

UNDERSTANDING THE FORMATION
AND EVOLUTION OF NUCLEI IN
GALAXIES USING N-BODY
SIMULATIONS

Markus Hartmann

A THESIS SUBMITTED IN PARTIAL FULFILMENT
OF THE REQUIREMENTS FOR THE DEGREE OF
DOCTOR OF PHILOSOPHY

Jeremiah Horrocks Institute for Astrophysics and Supercomputing
University of Central Lancashire

August 2011

Declaration

The work presented in this thesis was carried out in the Jeremiah Horrocks Institute for Astrophysics and Supercomputing, University of Central Lancashire.

I declare that while registered as a candidate for the research degree, I have not been a registered candidate or enrolled student for another award of the University or other academic or professional institution.

I declare that no material contained in the thesis has been used in any other submission for an academic award and is solely my own work.

Chapter 2 and 3 of this thesis have been submitted to the journal, Monthly Notices of the Royal Astronomical Society, and is public available on ArXiv e-prints, arXiv:1103.5464v1.

For Nina

Abstract

Galaxies across the Hubble sequence harbour central massive objects (CMOs) such as supermassive black holes (SMBHs) and massive stellar nuclear clusters (NCs) (Geha et al., 2002; Böker et al., 2004; Côté et al., 2006). Remarkably, both follow the same correlation between their mass, M_{CMO} , and that of their host galaxy (Ferrarese et al., 2006; Wehner & Harris, 2006; Rossa et al., 2006). These relations suggest that SMBHs and NCs share a similar growth history, and that these CMOs are connected with the evolution and formation of their host galaxy. Therefore, the centres of galaxies can provide vital constraints on galaxy formation processes, and, to date, no clear explanation exists for the variety of phenomena present therein.

Unlike SMBHs, the stellar populations and kinematics of NCs also provide information about their growth. NCs have complex star formation histories, and are often flattened compound objects with a nuclear cluster disc of young stars and spheroidal component (Seth et al., 2006). Analytical and numerical studies of the two suggested formation scenarios, the radial transport of gas with in-situ star formation (Milosavljević, 2004; Bekki, 2007), and the merger and accretion of star clusters due to dynamical friction (Tremaine et al., 1975; Bekki et al., 2004; Capuzzo-Dolcetta & Miocchi, 2008a). Both scenarios yield similar observed scaling relations between the size and mass of NCs. However, these studies have not taken into account the NC's structural properties. These studies were not able to consider the kinematical constraints provided by recent observations showing that NCs are rapidly rotating (Seth et al., 2008b).

Amongst the scaling relations between the SMBH and properties of the host galaxy, the correlation between the mass of the SMBH, M_{\bullet} , and the aperture velocity dispersion of stars in the bulge, σ_e , the $M_{\bullet} - \sigma_e$ relation, is the tightest (Gebhardt et al., 2000a; Ferrarese & Merritt, 2000; Tremaine et al., 2002; Ferrarese & Ford, 2005; Gültekin et al., 2009b). The problem of unraveling the formation and evolution of the scaling relations of SMBHs is, therefore, of great interest, and has been much debated over the last decade. While in elliptical galaxies, σ_e of the total galaxy correlates with the M_{\bullet} of the SMBH, in disc galaxies σ_e of the bulge scales with the M_{\bullet} . Some bulges in disc galaxies are found to be offset from the $M_{\bullet} - \sigma_e$ relation (Hu, 2008; Gadotti & Kauffmann, 2009). Graham et al. (2011) find that bulges in barred spiral galaxies tend to be below the $M_{\bullet} - \sigma_e$ relation of unbarred galaxies with an offset about 0.5 dex. The evolution of the $M_{\bullet} - \sigma_e$ relation has been studied in a number of galaxy merger simulations (Kazantzidis et al., 2005; Robertson et al., 2006; Younger et al., 2008; Johansson et al., 2009), but the evolution of the $M_{\bullet} - \sigma_e$ relation in bulges, along with the internal evolution of the disc, have not been investigated. The formation of spiral structure and bar formation can have drastic consequences on the kinematical properties of a galaxy’s bulge and disc. Similar to the SMBHs in barred spiral galaxies, NCs also show an offset from the $M_{\bullet} - \sigma_e$ relation of galaxies (Ferrarese et al., 2006). Unlike SMBHs in barred galaxies, NCs are ten times more massive, therefore, NCs appear above the $M_{\bullet} - \sigma_e$ relation.

I present observations and dynamical models of the NCs at the centres of the galaxies NGC 4244 and M33. I then compare these to an extensive set of simulations that test the importance of purely stellar dynamical mergers on the formation and growth of NCs. Mergers of star clusters can produce a wide variety of observational properties, including the densities, structural scaling relations, shapes (including the presence of young discs) and even rapid rotation of the NCs. Nonetheless, difficulties remain when comparing with kinematical properties. The profile of the line-of-sight

velocities, V , rise more slowly within the half mass radius, R_{eff} , than in NGC 4244. Most notably, the profile of the second order kinematic moment $V_{\text{rms}} = \sqrt{V^2 + \sigma^2}$, where σ is the line-of-sight velocity dispersion of stars, of the models are too centrally peaked to match observations. However, this can be partly remedied by the merger of star clusters onto a pre-existing nuclear cluster disc, but the profile of the line-of-sight velocity V is still more slowly rising than in NGC 4244. My results, therefore, suggest that purely stellar dynamical mergers cannot form NCs in late-type spiral galaxies, and that gas dissipation is a necessary ingredient for at least 50% of a NC's mass. Further studies of the anisotropy of the simulated NCs show that the negative vertical anisotropy found in NGC 4244 requires at least 10% of the mass to be accreted as stars, since gas dissipation and in situ star formation lead to positive vertical anisotropy. These predictions can be used to constrain the formation history of NCs and, so far, a hybrid model is favoured in late-type spiral galaxies. However, more observational data is essential to make further progress.

In another set of disc galaxy simulations I study the consequences of bar formation on the $M_{\bullet} - \sigma_e$ relation in bulges of galaxies. The redistribution of angular momentum within the disc leads to an increase in mass within the half mass radius of the bulge and raises the velocity dispersion σ_e of the stars within the galaxy. I find that the effect of orientation gives rise to a scatter $\lesssim 15\%$ in σ_e . However, the increase in σ_e is about a factor of $\sim 40\%$ and it shows a strong correlation with the relative changes in mass and with the anisotropy of the galaxy. If the initial M_{\bullet} follows the $M_{\bullet} - \sigma_e$ relation found in galaxies and does not grow as the bar forms, the increase in σ_e implies an offset from the $M_{\bullet} - \sigma_e$ relation. My simulations show that the offset from the $M_{\bullet} - \sigma_e$ relation is significant and larger than the 1σ uncertainty level. While σ_e is obtained within the radius containing half the mass of the bulge, R_{eff} , I also measured $\sigma_{e/8}$ in the aperture of $1/8R_{\text{eff}}$ to consider different influences of stars within the disc on the stars in the bulge. I perform a Kolmogorov-Smirnov

test which shows no evidence that σ_e and $\sigma_{e/8}$ follow different distributions, but the scatter in σ_e seems to be smaller than in $\sigma_{e/8}$. For a comparison, I also fit the $M_\bullet - \sigma_e$ relation to classical bulges and pseudo bulges in disc galaxies using the most recent sample of M_\bullet and σ_e measurements in disc galaxies. The offset in both types of bulges is significant and larger than the 1σ uncertainty level. Thus the increase in mass in the central region due to bar formation could explain the offset between barred and unbarred galaxies in the $M_\bullet - \sigma_e$ plane of galaxies.

Contents

Declaration	2
Abstract	4
Acknowledgements	15
1 Introduction	17
1.1 Motivation	17
1.2 Central Massive Objects	19
1.2.1 Supermassive Black Holes	19
1.2.2 Nuclear Clusters	24
1.3 Scaling Relations	27
1.3.1 M_{\bullet} - σ Relation	28
1.3.2 M_{CMO} - σ Relation	32
1.4 Formation and Evolution of Disc Galaxies	32
1.4.1 Bar Formation in Galaxies	35
1.5 Formation Scenarios of Nuclear Clusters	39
1.5.1 Radial Transport of Gas into the Centre	39
1.5.2 Merger Scenario	40
1.6 Nuclear Cluster Formation in Spiral Galaxies	43
1.7 Outline for the thesis	46

2	Integral Field observations of NGC 4244 and M33	50
2.1	Spectroscopy and isophotal shape of NGC 4244 and M33	50
2.2	Axisymmetry of the M33 nucleus	53
2.3	Modelling the Observations	54
2.3.1	The Jeans Anisotropic MGE dynamical models	54
2.3.2	JAM models of observed NCs	56
2.3.3	Rotation from the $(V/\sigma, \varepsilon)$ diagram	60
2.4	Conclusion	61
3	Constraining the role of star cluster mergers in nuclear cluster formation	63
3.1	Numerical Methods	63
3.1.1	Galactic disc model	64
3.1.2	Bulge model	67
3.1.3	Star cluster models	67
3.1.4	Bare NCD model	69
3.1.5	Numerical parameters	71
3.2	Results of the Merger Simulations	71
3.2.1	Structural properties	73
3.2.2	Remnant kinematics	75
3.2.3	Accretion onto Super Star Clusters	78
3.3	Accretion onto bare NCDs	87
3.3.1	Vertical anisotropy	93
3.4	JAM models of simulated NCs	93
3.5	Discussion	99
3.5.1	In situ formation versus accretion	99
3.5.2	Nuclear Cluster Formation in Dwarf Elliptical Galaxies	101
3.5.3	The $M_{\text{CMO}}-\sigma_e$ relation	102

3.6	Summary	103
4	Consequences of bar formation on the $M_{\bullet} - \sigma_e$ relation	105
4.1	Numerical methods	105
4.1.1	Galaxy models	105
4.1.2	Model parameters	107
4.1.3	Numerical parameters	108
4.2	Evolution of structural properties	112
4.3	Evolution of Dispersion	114
4.3.1	Contamination from the disc	116
4.3.2	The Effect of Orientation	121
4.4	Evolution of the $M_{\bullet} - \sigma_e$ relation	124
4.4.1	Zero-Point	124
4.5	Comparison with observations	129
4.6	Discussion	131
4.6.1	Offset in the $M_{\bullet} - \sigma_e$ relation	131
4.7	Summary	132
5	Summary of Conclusions and Future Prospects	134

List of Tables

3.1	Properties of star cluster models	70
3.2	Properties of nuclear cluster simulations	72
3.3	Global parameters from the JAM models for observed and simulated nuclear clusters	97
4.1	Disc galaxy simulations to study the evolution of the $M_{\bullet} - \sigma_e$ relation in barred galaxies	109
4.2	Results from χ^2 fit of $M_{\bullet} - \sigma_e$ relation	128

List of Figures

1.1	Mean projected mass density within the half mass radius, R_{eff} , as a function of the total mass for different stellar systems	26
1.2	$M_{\bullet} - \sigma$ relation for 64 galaxies	31
1.3	$M_{\bullet} - \sigma_e$ relation for supermassive black holes and nuclear clusters in the Virgo Cluster Survey	33
1.4	Radial distribution of globular clusters in dwarf elliptical galaxies	42
1.5	<i>Hubble Space Telescope</i> F814W images of edge-on nuclear clusters	45
1.6	Colour maps of three edge-on nuclear clusters	47
1.7	Velocity and velocity dispersion fields of nuclear clusters in NGC 4244 and M33	48
2.1	Velocity profiles of nuclear clusters in NGC 4244 and M33	52
2.2	Deviation of perfect ellipse of nuclear cluster in NGC 4244	53
2.3	Contour plot of MGE model of nuclear cluster NGC 4244	58
2.4	Observed and modelled kinematics of nuclear cluster in NGC 4244	59
2.5	$(V/\sigma, \varepsilon)$ diagram of observed nuclear clusters	62
3.1	Initial condition of the main disc	65
3.2	Distribution of particles in the main disc	66
3.3	Distribution of particles within the bulge	68
3.4	Volume density of star cluster models	70

3.5	Comparison of scaling relation of simulated and observed nuclear clusters	74
3.6	Shape of nuclear clusters in merger simulations	76
3.7	Edge-on shape properties of nuclear clusters in merger simulations	77
3.8	Kinematic fields of nuclear clusters in merger simulations	79
3.9	Anisotropy of nuclear clusters in merger simulations	80
3.10	Edge-on shape properties of nuclear clusters in accretion simulations	82
3.11	Evolution of $(V/\sigma)_e$ in simulation A1	84
3.12	Kinematic fields of nuclear clusters in accretion simulations	85
3.13	Kinematic profiles of nuclear clusters in accretion simulations	86
3.14	Anisotropy of nuclear clusters in accretion simulations	86
3.15	Surface density fields, mass and luminosity weighted profiles of nuclear clusters in the accretion simulations	88
3.16	Vertical density profile of the nuclear cluster in simulation A2	90
3.17	Evolution of $(V/\sigma)_e$ in simulation A2	91
3.18	Profile of the second order velocities V_{rms} for simulation A2	92
3.19	The effect of different projections on β_z in the NC in NGC4244	94
3.20	Changes in anisotropy during accretion of different massive star cluster	95
3.21	$(V/\sigma, \varepsilon)$ diagram of observed and simulated nuclear clusters	98
4.1	Fractional changes in mass of disc and bulge and the average changes in σ_e as a function of bar strength	113
4.2	Correlation of σ_e and the fractional changes in mass in the disc and bulge component	115
4.3	Anisotropy as function of bar strength	117
4.4	The changes in σ_e as function of anisotropy	118
4.5	Contours of bulge-to-disc mass ratio in the B/D and R_{eff}/R_d plane	119
4.6	Correlation of σ_e and $\sigma_{e/8}$ in the disc and bulge + disc	120

4.7	Cumulative distribution of $\sigma_{e/8}$ and σ_e	122
4.8	The evolution of the scatter $\Delta\sigma_e$ as a function of anisotropy	123
4.9	Scatter $\Delta\sigma_e$ at fixed inclination	125
4.10	Scatter $\Delta\sigma_e$ at fixed position angles	126
4.11	Scatter $\Delta\sigma_e$ averaged over all orientations	127
4.12	Offset in the $M_\bullet - \sigma_e$ relation in simulations	128
4.13	The $M_\bullet - \sigma_e$ relation for classical bulges in disc galaxies, classical and pseudo bulges in barred spiral galaxies	130

Acknowledgements

The work presented in my thesis could not have been done without the support of many people, my colleagues, my friends in Germany and in England and my beloved family. I would like to say thank you to all of them.

I would like to express my gratitude and appreciation to my supervisor Victor Debattista for the opportunity to work on these fascinating projects. Thank you very much for all your support and patience during the time I was working on these projects. You have taught me a lot of interesting things, mostly how to work as a scientist. It was not always easy, but you never give up until I got the knack on it. There is still so much to learn and I hope that I can continue to work on these fascinating subject. I also would like to express my gratitude to Tim Cawthorne who become my secondary supervisor in 2010 and provided guidance for the thesis.

I would like to thank my collaborators Anil Seth, Michele Cappellari, Tom Quinn and Monica Valluri. Especially Anil and Michele, who supported me throughout my PhD.

I would like to thank my external examiner John Magorrian and my internal examiner Cristina Propescu for willing to read my thesis and to take the time to organise the viva of my PhD.

I would like to thank the former Starlink manager Steven Chapman, the acting Starlink manager David Capstick and the former HPCF manager Xiaohu Guo for their support and helping hands whenever the computer was not doing what I asked it to do.

I would like to thank all my colleagues from the Jeremiah Horrocks Institute. It was a great and exciting time. We had a lot of joy, not even at work. Especially, I would like to thank Katie, Aveek, Sortiris, Srinivasan and Owain.

I would like to thank Esko Gardner, Chris Brook and Rok Roskar who were always helping me and very supportive in several occasions.

A very special thank goes to my two flatmates, Elisa and Gemma. You both always cheered me up and helped me whenever I was in distress. I would also like to thank Christine Brown, who gave me a place to stay during the first time of my PhD and become a very good friend of mine.

In particular I would like to thank my parents. Without their support, I would never have come so far in my life. They have always encouraged me and supported me through my life.

Finally I would like express my gratitude to Nina. I know it was a tough time for you and me, but you have been always encouraging and supporting me from near and far. You always believed in me and you fill my heart with love. Therefore, I dedicate my work to you as a sign of my deepest gratitude.

Thanks a million to all of you and those who I missed to call!

Markus Hartmann
Preston, August 2011

Chapter 1

Introduction

1.1 Motivation

Galaxies are the stellar islands in our Universe. These extraordinary and beautiful agglomerations of stars are not only the places of stellar birth and death, but also the source of light, which allows us to explore our Universe through cosmological scales. In the present model of cosmology, the Universe is believed to consist of 70% dark energy (Riess et al., 1998; Perlmutter et al., 1999), which is believed to cause an accelerated expansion of the Universe, and 25% dark matter (Hinshaw et al., 2009), which only interacts through gravitational forces. Dark matter is believed to be the main part of galaxies and structures in the Universe. The content of ordinary, baryonic matter is only about 4% of the Universe. For the understanding of the whole picture of the Universe, it is therefore essential to understand how the variety of galaxies have formed and evolved in our Universe. It was Edwin Hubble (1936) who brought the diversity of galaxies into a unifying schema. Across this sequence of galaxies, at their centres, the densest and most massive objects known in the Universe, supermassive black holes, are found. These fabulous objects, and dark matter, both have in common the fact that there was scepticism regarding their dynamical mass measurements, and that their acceptance was preceded by decades

of debate. Dark matter has become an essential feature for our understanding of many phenomena in galaxy formation, and in the formation of large scale structure in the Universe. A similar situation exists with regard to the prevailing view of the centres of galaxies.

Supermassive black holes seem to be a relic of the formation process of the host galaxy and they have been recognised as the source of energy driving the Universe's powerful objects, quasars (quasi-stellar radio sources) (Lynden-Bell, 1978). These objects are observed in the distant universe (Willott et al., 2007) and they evolve during a specific era of the evolution of galaxies. However, the growth of a supermassive black hole during this evolutionary process is remarkably slow, so that they have to grow to a mass of $10^8 M_{\odot}$ before they reach the quasar phase of galaxy evolution. Since that era, the growth of supermassive black holes does not seem to be accompanied by any emission of electromagnetic radiation. Nonetheless, the merger of two binary black holes at the very centre is likely to be the most powerful extragalactic sources of gravitational waves, and perhaps the only ones powerful enough to be detected by the *Laser Interferometer Space Antenna* a planned ESA/NASA mission. Understanding the evolution and formation processes within the central region of galaxies will shed light on the formation history of central massive objects and on the galaxy itself.

In the last decade observations of the centre of galaxies at high spatial resolution have revealed a large fraction of dense stellar systems, the so called **Nuclear Clusters**. Like supermassive black holes, they have been found in all types of galaxies. These environments are fossil records of the formation and evolution of the central region of their host galaxy. Their structural and kinematic properties are important constraints on their formation. I use N -body simulations to understand the evolution and formation of these fascinating phenomena which are among the most dense stellar systems known in our Universe.

1.2 Central Massive Objects

The centre of a galaxy is a special place due to its deep gravitational potential well and unique dynamics and, therefore, provides an environment for exotic objects such as Active Galactic Nuclei (AGN), quasars, supermassive black holes (SMBH) and nuclear clusters (NC). These objects are collectively referred to central massive objects (CMO). In this chapter I will describe the properties of these objects and show what they have in common.

1.2.1 Supermassive Black Holes

Black holes are thought to exist in at least three different mass ranges. The evolutionary end point of some massive stars are black holes with masses of $\sim 10 M_{\odot}$, which are referred to as stellar black holes. Intermediate mass black holes (IMBH) $\sim 10^4 M_{\odot}$ are suggested to lurk at the centres of globular clusters (GC) (Gebhardt et al. 2000b, 2005; Gerssen et al. 2002, 2003; Noyola et al. 2008, 2010, but see also van der Marel & Anderson 2010). Finally SMBHs are predicted in the centre of galaxies (Richstone et al., 1998; Magorrian et al., 1998). The relation of these three classes of black holes is unknown.

One of the favoured scenario is that SMBH seeds are the remnants of the first population of stars, called Population III stars, which form out of primordial gas. These stars are believed to form in dark matter halos of $10^6 - 10^8 M_{\odot}$ at redshifts $z \sim 20 - 50$ (Tegmark et al., 1997). The fragmentation of primordial gas is physically simpler than star formation in the local universe because, in the absence of metals and dust, the only cooling mechanisms are through molecular and neutral hydrogen (F. Palla, H. Zinnecker, A. Maeder, & G. Meynet, 2002). These first generation of stars tend to be very massive, which has been shown in simulations of the collapse of primordial gas clouds (Abel et al., 2000; Bromm et al., 2002; Yoshida et al., 2006; Gao et al., 2007). The most massive Population III stars ($> 260 M_{\odot}$) are suggested

to form black holes with masses of $\sim 100 M_{\odot}$ (Bond et al., 1984; Woosley & Weaver, 1986; Fryer et al., 2001). Therefore, it has been suggested (Madau & Rees, 2001) that in the high density environments of the early universe, relic black holes of $> 150 M_{\odot}$ form in the cores of more massive dark matter halos.

Another avenue for SMBH formation is the collapse of massive objects directly out of dense gas (Haehnelt & Rees, 1993; Loeb & Rasio, 1994; Eisenstein & Loeb, 1995; Bromm & Loeb, 2003; Koushiappas et al., 2004; Begelman et al., 2006; Lodato & Natarajan, 2006). The very first proto-galaxies consisting of primordial gas are suggested to lead to SMBH formation, because the cooling of gas is less efficient and therefore, fragmentation and star formation are inhibited (Bromm & Loeb, 2003; Santoro & Shull, 2006). In addition, a highly turbulent system could also inhibit fragmentation, so that proto-galaxies with metal-enriched gas could form SMBHs due to efficient gas collapse (Begelman, 2010; Mayer et al., 2010). In these proto-galaxies, gas contracts until rotational support halts the collapse. Wise et al. (2008) and Regan & Haehnelt (2009) have studied numerical simulations of gaseous discs and found that these discs can lose 90% of their angular momentum due to supersonic turbulence. These central massive gas clouds can result in the formation of a supermassive star. Nuclear fusion processes may be present, but subsequent infall leads to further contraction of the core within the supermassive star and to the collapse into a black hole, which then grows via the accretion of the envelope up to a mass of $10^4 - 10^5 M_{\odot}$ (Begelman et al., 2006, 2008).

When gas collapse is less efficient and star formation proceeds in small dark matter halos, more massive halos are built-up and they become enriched with metals. Therefore, fragmentation and star formation of low mass stars is even more efficient (Omukai et al., 2008). The first episode of Population II star formation is believed to result in massive star clusters (Schneider et al., 2006; Clark et al., 2008), in which SMBH seeds can form in the range of $10^2 - 10^4 M_{\odot}$ due to stellar collisions (Devecchi

& Volonteri, 2009). The formation of SMBH seeds in dense stellar systems is a long standing idea (Begelman & Rees, 1978; Ebisuzaki et al., 2001; Miller & Hamilton, 2002; Portegies Zwart & McMillan, 2002; Portegies Zwart et al., 2004; Freitag et al., 2006; Gürkan et al., 2004, 2006). The main mechanism for the dynamical evolution of a star cluster is dynamical friction (Chandrasekhar, 1943), which lets the massive stars segregate toward the centre due to the loss of orbital energy. If this dynamical process is faster than the stellar evolution of the most massive stars (< 5 Myrs), the core of the star cluster collapses, because the star cluster attempts to reach a state of equilibrium. Energy conservation and the evaporation of less bound stars lead to a decrease in the size of the core (Spitzer, 1987). In these cores, stellar collisions can take place in a runaway fashion which could lead to stellar black holes (Miller & Hamilton, 2002; Portegies Zwart & McMillan, 2002). In a study of proto-galaxies Devecchi & Volonteri (2009) find that a fraction of ~ 0.05 proto-galaxies at $z \sim 10 - 20$ form black hole seeds with masses $\sim 10^3 M_{\odot}$.

Most evidence of the existence of SMBHs in our Universe is because SMBHs are thought to be the power source of quasars and AGN. Lynden-Bell (1978) shows that accretion discs around SMBH can convert $\sim 10\%$ of the rest mass of an object into energy, a higher efficiency than in thermonuclear reactions, which have typical energy production rates of 1%. As most quasars died out by redshift of $z < 2$, the nearby universe is populated with relic SMBHs. It was Chokshi & Turner (1992) who argue that the average mass density ρ_u of SMBHs in the local universe matches or exceeds the mass-equivalent of the energy density u emitted by quasars:

$$u = \int_0^{\infty} \int_0^{\infty} L \Phi(L, z) dL \frac{dt}{dz} dz = 1.3 \times 10^{-16} J m^{-3}, \quad (1.1)$$

where $\Phi(L, z)$ is the comoving density of quasars with luminosity L at redshift z and t is the time. The corresponding present-day mass density for a radiative efficiency ϵ is $\rho_u = u/(\epsilon c^2) = 2.2 \times 10^4 \epsilon^{-1} M_{\odot} \text{ Mpc}^{-3}$. Compared to the luminous density in galaxies $j = 1.1 \times 10^8 L_{\odot} \text{ Mpc}^{-3}$ (Loveday et al., 1992), we obtain the ratio of the

SMBH mass to the galaxy bolometric luminosity, as

$$\Upsilon = \frac{\rho_u}{j} = 1.8 \times 10^{-3} \left(\frac{-0.1}{\epsilon} \right) \left(\frac{M_\odot}{L_\odot} \right). \quad (1.2)$$

A geometrically-thin and optically-thick accretion disc has an efficiency of $\epsilon \sim 0.1$ (Frank et al., 1992). Then Eqn. 1.2 predicts SMBHs with a mass $M_\bullet \sim 10^7 M_\odot$, in a typical galaxy with luminosity $L_* \simeq 10^{10} L_\odot$ and $M_\bullet \sim 10^6 M_\odot$ for a dwarf spheroidal galaxy with $L_* \simeq 10^9 L_\odot$.

Quasars have been detected at very high redshift ($z > 6$), where the Universe had an age of less than 1 Gyr (*e.g.* Haiman, 2004; Shapiro, 2005; Volonteri & Rees, 2006; Tanaka & Haiman, 2009). The question of how SMBH seeds could grow during this time remain open. Cosmological hydrodynamical simulations suggest the formation of a dense central gas concentration (Pelupessy et al., 2007; Wise et al., 2008; Greif et al., 2008), but these simulations have insufficient resolution to study the accretion and radiative feedback processes of a seed black hole, nor do these simulations resolve the fine structures of these dense gas clouds, where the seed black holes are embedded (Pelupessy et al., 2007; Johnson & Bromm, 2007).

The influence radius of a SMBH, R_{infl} , can be determined from the velocity of stars at which the potential of the SMBH is equal their velocity dispersion σ (Binney & Tremaine, 2008):

$$R_{infl} = \frac{GM_\bullet}{\sigma^2 (R_{infl})} = 11 \text{ pc} \frac{M_\bullet}{10^8 M_\odot} \left(\frac{\sigma}{200 \text{ km s}^{-1}} \right)^{-2}, \quad (1.3)$$

where G is the gravitational constant. For a reasonable SMBH in an elliptical galaxy, $R_{infl} \sim 20$ pc, so that at a distance of $d \sim 20$ Mpc (the distance to the Virgo cluster is 16.5 ± 0.1 Mpc) the angular size is about 0.2 arcsec. This is only greater by factor of 2 than the best angular resolution of the *Hubble Space Telescope* (HST). If SMBH are not accreting, and therefore an AGN is not detectable, the only possible way to measure the mass of a quiescent SMBH is from its gravitational potential. Solving the collisionless Boltzmann equation, one obtains the Jeans equation for spherical

galaxies:

$$\frac{d(\rho\sigma_r^2)}{dr} + 2\frac{\beta\rho\sigma_r^2}{r} = -\rho\frac{d\Phi}{dr}, \quad (1.4)$$

where Φ is the potential, σ_r the radial velocity dispersion, ρ the mass density, which can be obtained by measuring the mass to light, M/L , the luminosity density $j(r)$ and the anisotropy

$$\beta \equiv 1 - \frac{\sigma_\theta^2 + \sigma_\phi^2}{2\sigma_r^2}. \quad (1.5)$$

If we assume that the system is isotropic ($\beta = 0$), the M_\bullet and the mass of stars is determined by

$$M(r) = -\frac{r}{G} \left(\sigma^2 \frac{d \ln j}{d \ln r} + \frac{d\sigma^2}{d \ln r} \right). \quad (1.6)$$

It was shown by Binney & Mamon (1982) that if the assumption $\beta = 0$ is not valid, there is more than one solution for a given σ and $l(r)$. Furthermore if a SMBH is present, stars are scattered and the stellar system become tangential biased ($\beta < 0$). Thus assuming $\beta = 0$ would overestimate M_\bullet . Nonetheless, several groups have successfully hunted for galactic quiescent SMBHs using high resolution spectroscopic studies performed with the HST and the largest ground-based telescopes (*e.g.* the *Very Large Telescope* (VLT)) by fitting dynamical models to both the photometry and the line-of-sight velocity dispersion, measured at different radii, particularly on parsec scales (Richstone & Tremaine, 1985; van der Marel et al., 1998; Gebhardt et al., 2003).

Aside from the dynamical modelling, SMBHs can be detected as AGN, if the SMBH is accreting matter. The reverberation mapping of the broad emission lines in the AGN is used to determine the size of the emission region (*e.g.* Blandford & McKee, 1982; Peterson et al., 2004). They use emission lines such as *e.g.* $H\beta$ which traces the motion of the gas within the potential of the SMBH. The M_\bullet can be determined by measuring the velocity dispersion and the size of the emission line region (Shen et al., 2008; Greene et al., 2010).

Have we found SMBHs at the centre of galaxies? Dynamical proof of SMBHs requires measurement of relativistic velocities near the Schwarzschild radius, $r_S \simeq 10^{-5}$ pc for a SMBH with $10^8 M_\odot$. Even for M31, this is 3×10^{-6} arcsec. HST angular resolutions is only $0''.1$. However, what dynamical searches have contributed is the first solid evidence for massive dark objects in a galaxy nucleus. The most promising evidence has been made in our own Galaxy. The study of the orbits of stars around the radio source SgrA*, so called S stars, are well described by Keplerian orbits and have been studied since 1992. The orbit of the star S2 has a orbital period of ~ 16 yrs and pericentre of 100 AU. To explain the orbits of these stars, a central dark object with a mass of $\sim 4.3 \pm 0.5 \times 10^6 M_\odot$ is needed coincident with the radio source of SgrA* (Ghez et al., 2005; Gillessen et al., 2009). Thus the most plausible explanation for this object is a SMBH (Maoz, 1998).

1.2.2 Nuclear Clusters

In the last decade, observations from the HST have revealed that the centres of galaxies are occupied by compact, barely resolved sources. Based on their structural properties, which are similar to those to stellar clusters, and their spectra, these sources clearly have a stellar origin. For this reason, they are called nuclear cluster or stellar nuclei. As is the case of SMBHs, NCs are found in all type of galaxies: in elliptical galaxies (Côté et al., 2006), in dwarf elliptical galaxies (Wehner & Harris, 2006) and in spiral galaxies (Rossa et al., 2006). The formation of NCs is therefore linked with the evolution of galaxies.

The fraction of NCs in late-type (Scd-Sm) spiral galaxies is $\sim 75\%$, in earlier-type (Sa-Sc) spiral galaxies is $\sim 50\%$ and in spheroidal (E and S0) galaxies the fraction is $\sim 70\%$. Therefore, NC are very common across the Hubble sequence. With typical absolute *I*-band magnitudes between -14 to -10 , NCs are 40 times more luminous than the average Milky Way globular cluster (GC) (Harris, 1996).

However NCs are as compact as Milky Way GCs. Their half-light radii, which is the radius containing half the luminosity of the object, are typically 2–5 pc, independent of galaxy type (Geha et al., 2002; Böker et al., 2004; Côté et al., 2006). Despite their compactness they are more massive than GCs. Spectra of NCs in a sample of late-type spiral galaxies from the *Ultraviolet and Visual Echelle Spectrograph* (UVES) on the VLT reveal velocity dispersions in a range of $\sigma = 13 - 34 \text{ km s}^{-1}$, indicating a dynamical mass of $10^6 - 10^7 M_{\odot}$ (Walcher et al., 2005). As shown in Figure 1.1, NCs in spiral galaxies and in dwarf elliptical galaxies (dEs) lie in the upper mass range of the same sequence of GCs, in the plane given by the effective surface density versus the total mass of the objects. On the other hand, there is a gap between dwarf spheroidal galaxies and NCs, which makes a direct evolutionary connection between these two types of stellar systems unlikely (Walcher et al., 2005).

Data from a survey of 40 spiral galaxies of various Hubble types (Rossa et al., 2006) observed by the *Space Telescope Imaging Spectrograph* (STIS) on the HST were used to fit single stellar populations models with different ages. This yields values for parameters of NCs like: extinction, metallicity and star formation history, luminosity-weighted mean age and the mass to light ratio M/L . For the NC in NGC 300, Rossa et al. (2006) find a metallicity $Z = 0.004$, an extinction of $A_V = 0.4$, a luminosity-weighted mean $\langle \log(\text{age}/\text{Gyr}) \rangle = 8.63$ and $M/L_B = 0.51 M_{\odot}/L_{\odot}$. The implied NC mass is $M_{NC} = 10^{5.7} M_{\odot}$. The estimated masses from the VLT and HST from the spectral population fitting are in good agreement with the dynamical models (van der Marel et al., 2007).

The star formation history of NCs is complex, due to the fact that most NCs have stellar populations comprised of multiple generations of stars (Rossa et al., 2006; Walcher et al., 2006). The youngest population of stars is nearly always younger than 100 Myrs, which indicates that NCs experience frequent and repetitive star formation episodes. The NCs in early-type spiral galaxies tend to have younger

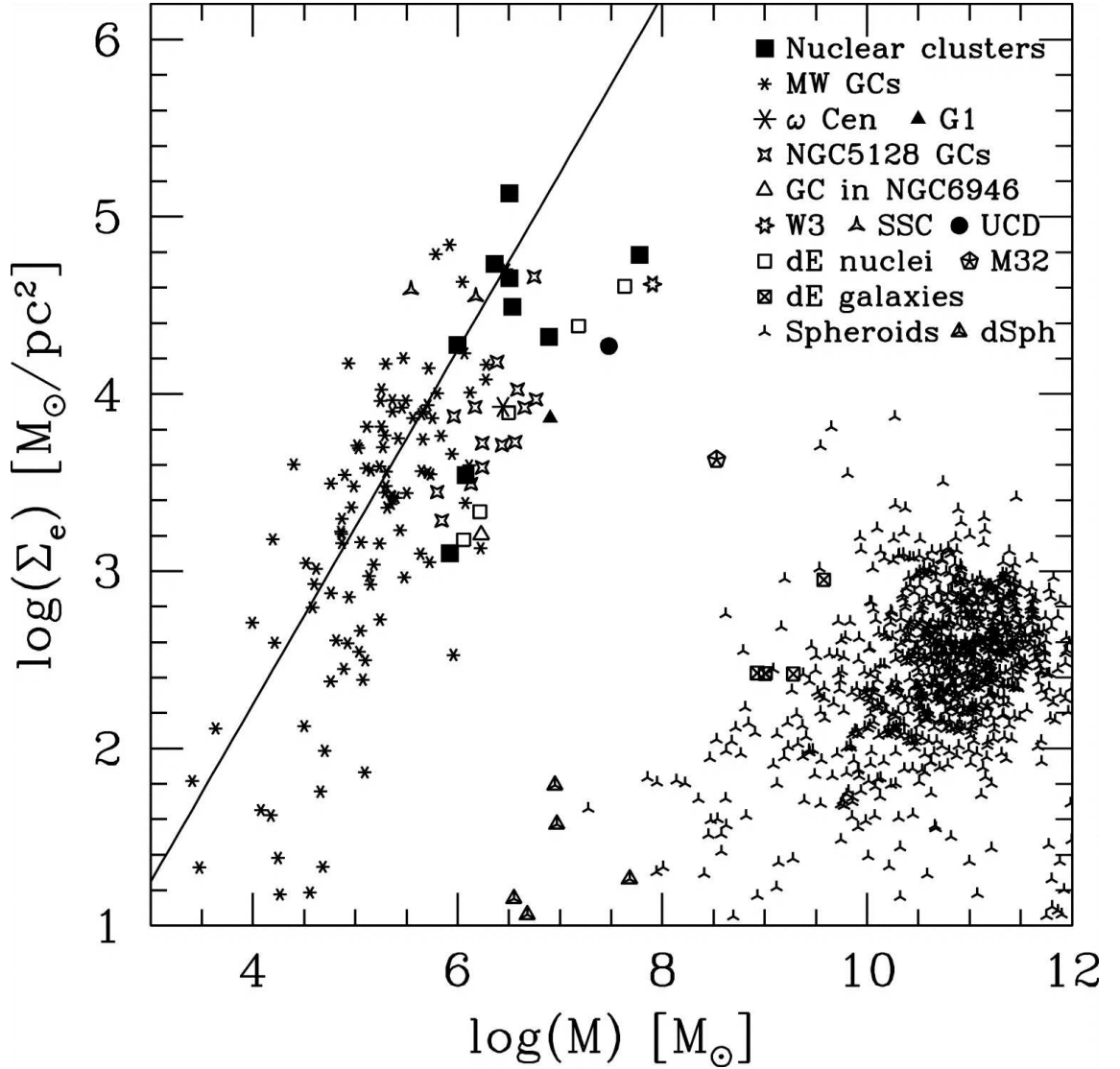


Figure 1.1: Mean projected mass density within the half mass radius, R_{eff} , versus the total mass for different types of stellar systems as labeled in the plot. Dwarf elliptical galaxies are found on the right side of the plot, whereas GCs are found on the left side, where $R_{\text{eff}} = 3$ pc is shown by the solid black line. NCs in spiral galaxies and in dwarf elliptical galaxies lie on the high-mass end of GC sequence. Figure taken from Walcher et al. (2005).

luminosity-weighted mean ages than those in late-type spiral galaxies (van der Marel et al., 2007). Even if the light of a NC is dominated by the young population, there is an underlying older population which contains most of the mass (van der Marel et al., 2007). Carollo et al. (2002) find that NC luminosities in early-type spiral galaxies are, on average, brighter than those in late-type spiral galaxies. Rossa et al. (2006) find that this relation is true for NC masses as well, and that the total mass loosely correlates with the total luminosity of the host galaxy bulge. The studies of NCs in different Hubble types (Côté et al., 2006; Rossa et al., 2006; Wehner & Harris, 2006) have made it clear that NC obey scaling relations similar to those of the host galaxy and SMBHs.

1.3 Scaling Relations

Scaling relations between intrinsic properties of galaxies provide clues to the physical mechanisms in these systems. The tighter a relation is, the more fundamental the relation is expected to be. Therefore, it is not surprising that there is a huge interest in scaling relations between the CMO and its host galaxy. In the study for the demographics of SMBHs, Kormendy & Richstone (1995) and Marconi & Hunt (2003) found that the SMBH mass, M_{\bullet} , is proportional to the galaxy bulge mass, M_{bul} . Magorrian et al. (1998) and Häring & Rix (2004) discovered that M_{\bullet} scales with the bulge luminosity L_{bul} . SMBHs exhibit a number of other scaling relations such as those with the bulge velocity dispersion, the $M_{\bullet} - \sigma_e$ relation (Gebhardt et al., 2000a; Ferrarese & Merritt, 2000; Tremaine et al., 2002; Ferrarese & Ford, 2005), with the mass of the galaxy, the $M_{\bullet} - M_{\text{gal}}$ relation (Ferrarese, 2002; Baes et al., 2003), the Sérsic index of the surface brightness profile, the $M_{\bullet} - n$ relation (Graham & Driver, 2007), where n has been measured for the bulge only by using a decomposition of the disc and bulge in the case of spiral galaxies, and with the inner core radius, the $M_{\bullet} - r_{\gamma}$ relation (Lauer et al., 2007). Amongst these, the tightest

is the relation between M_\bullet and the velocity dispersion, σ_e , of the stars in elliptical galaxies and of the stars within the spheroid in disc galaxies. Thus I refer to these as the bulges of the host galaxy.

1.3.1 M_\bullet - σ Relation

Ferrarese & Merritt (2000) and Gebhardt et al. (2000a) found a scaling relation with the form of

$$\log\left(\frac{M_\bullet}{M_\odot}\right) = \alpha + \beta \log\left(\frac{\sigma}{200 \text{ km s}^{-1}}\right). \quad (1.7)$$

Measurements of the slope β have varied amongst different studies ranging from $\beta = 3.75 \pm 0.3$ (Gebhardt et al., 2000a) to $\beta = 4.8 \pm 0.5$ (Ferrarese & Merritt, 2000). Tremaine et al. (2002) interpreted this discrepancy to be mostly due to systematic differences in velocity dispersion. While Ferrarese & Merritt (2000) and Merritt et al. (2001) estimate the central stellar velocity dispersion, σ_c , as a luminosity weighted root-mean-square velocity dispersion extrapolated to an aperture of radius, $R_{\text{eff}}/8$, where R_{eff} is the effective or half-light radius of the host galaxy bulge, Gebhardt et al. (2000a) and Tremaine et al. (2002) used the stellar velocity dispersion σ_e measured within a slit aperture of length $2R_{\text{eff}}$. The most recent study by Gültekin et al. (2009b) finds a slope of $\beta = 4.24 \pm 0.41$, with the zero-point $\alpha = 8.12 \pm 0.08$ and with an intrinsic scatter of $\epsilon = 0.44 \pm 0.06$ for all galaxies.

How do SMBHs evolve onto the $M_\bullet - \sigma_e$ relation? In the present picture of hierarchical galaxy formation, structure formation proceeds such that smaller structures form prior to larger ones (*e.g.* Blumenthal et al., 1984; Frenk et al., 1985, 1988; Efsthathiou et al., 1988). Therefore, the evolution towards the $M_\bullet - \sigma_e$ relation depends on the seeding prescription (see Section 1.2.1). While low mass black hole seeds would lie below a $M_\bullet - \sigma_e$ relation, more massive black hole seeds would initially lie above the $M_\bullet - \sigma_e$ relation (Volonteri & Natarajan, 2009). The $M_\bullet - \sigma_e$ relation could be established if self-regulated accretion is associated with the hierarchical

formation of galaxies. A number of possible mechanisms have been suggested. In a merger of galaxies, the accretion of gas onto a SMBH can be regulated by star formation (Burkert & Silk, 2001; Kazantzidis et al., 2005; Zheng et al., 2009) or the accretion of matter from a nuclear disc that has been enhanced by accretion of stars (Miralda-Escudé & Kollmeier, 2005). In addition, the vast energy available from an accreting SMBH can connect the growth of the SMBH and the properties of the hosting bulge. Only a small part of the energy from an accreting SMBH is needed to influence the temperature and structure of the interstellar medium of the host galaxy (Silk & Rees, 1998; King, 2003; Wyithe & Loeb, 2003; Di Matteo et al., 2005; Murray et al., 2005; Sazonov et al., 2005; Younger et al., 2008). However, as an alternative, the $M_{\bullet} - \sigma_e$ relation could be a consequence of unrelated processes (Adams et al., 2001, 2003; Jahnke & Maccio, 2010). Since the merger rate and number of major mergers are greater in the early times of galaxy formation, the $M_{\bullet} - \sigma_e$ relation should be established earlier in massive elliptical galaxies than in lower mass galaxies, like bulges in early and late type spiral galaxies (Volonteri & Natarajan, 2009). Thus, studying the demographics of SMBHs of the lower mass end at scaling relations, could shed light on the evolution of SMBHs and hint to the formation of the SMBH seeds in the early universe.

Elliptical galaxies and bulges in disc galaxies share structural and kinematical properties (*e.g.* Wyse et al., 1997; Kormendy & Kennicutt, 2004), and, therefore, they have similar positions in the fundamental plane which combines the parameter of the central velocity dispersions σ_c , the central surface brightness μ_e and effective radius R_{eff} (Bender et al., 1992). In the present picture of galaxy formation, ellipticals and bulges are forming via the mergers of galaxies and the accretion of smaller satellite galaxies (Eggen & Sandage, 1962; Tremaine et al., 1975; Searle & Zinn, 1978; Kauffmann et al., 1993; Baugh et al., 1996; van den Bosch, 1998). On the other hand, the properties of bulges are also found to be intimately related to

the disc of their host galaxy. For example, the effective radius, R_{eff} , of the bulge has been found to scale with the scale-length of the disc and the colour of the bulge is similar to that of the inner part of the disc (see Kormendy & Kennicutt, 2004, for a review). Bulges are divided into two different types, those having similar properties to elliptical galaxies and believed to form via mergers are called *classical bulges* and those having properties that are related to the properties of discs are called *pseudo bulges*. As opposed to classical bulges, pseudo bulges are thought to form via secular processes in the disc such as due to the presence of a bar or from spirals (Combes & Sanders, 1981; Combes et al., 1990; Raha et al., 1991; Norman et al., 1996; Courteau et al., 1996; Bureau & Athanassoula, 1999; Debattista et al., 2004; Athanassoula, 2005; Drory & Fisher, 2007). Do SMBHs found in classical bulges and pseudo bulges follow the same scaling relations as the ones in elliptical galaxies? Hu (2008) found that SMBHs in elliptical galaxies and those found in classical bulges follow similar scaling relations, and that pseudo bulges differ from these relations. He finds that SMBHs in pseudo bulges have a significant offset from the $M_{\bullet} - \sigma_e$ relation of elliptical and classical bulges. In contrast, Gadotti & Kauffmann (2009), using stellar mass measurements of the Sloan Digital Sky Survey, to showing that there are different $M_{\bullet} - \sigma_e$ relations for pseudo-bulges, classical bulges and elliptical galaxies. Hu (2008) and Gadotti & Kauffmann (2009) both point out that the presence of bars in those galaxies could also be responsible for the offset from $M_{\bullet} - \sigma_e$. Moreover, Graham (2008a) and Graham & Li (2009) discovered that by excluding barred galaxies, the intrinsic scatter in the $M_{\bullet} - \sigma_e$ relation is reduced. In a sample of 64 galaxies, Graham et al. (2011) define a barless $M_{\bullet} - \sigma_e$ relation. They found that barred galaxies have an offset about ~ 0.5 dex from the barless $M_{\bullet} - \sigma_e$ relation. In Figure 1.2, the $M_{\bullet} - \sigma_e$ relation is presented for 64 galaxies (Graham, 2008b; Graham et al., 2011). The barred galaxies are denoted with a cross and lie mostly below the $M_{\bullet} - \sigma_e$ relation.

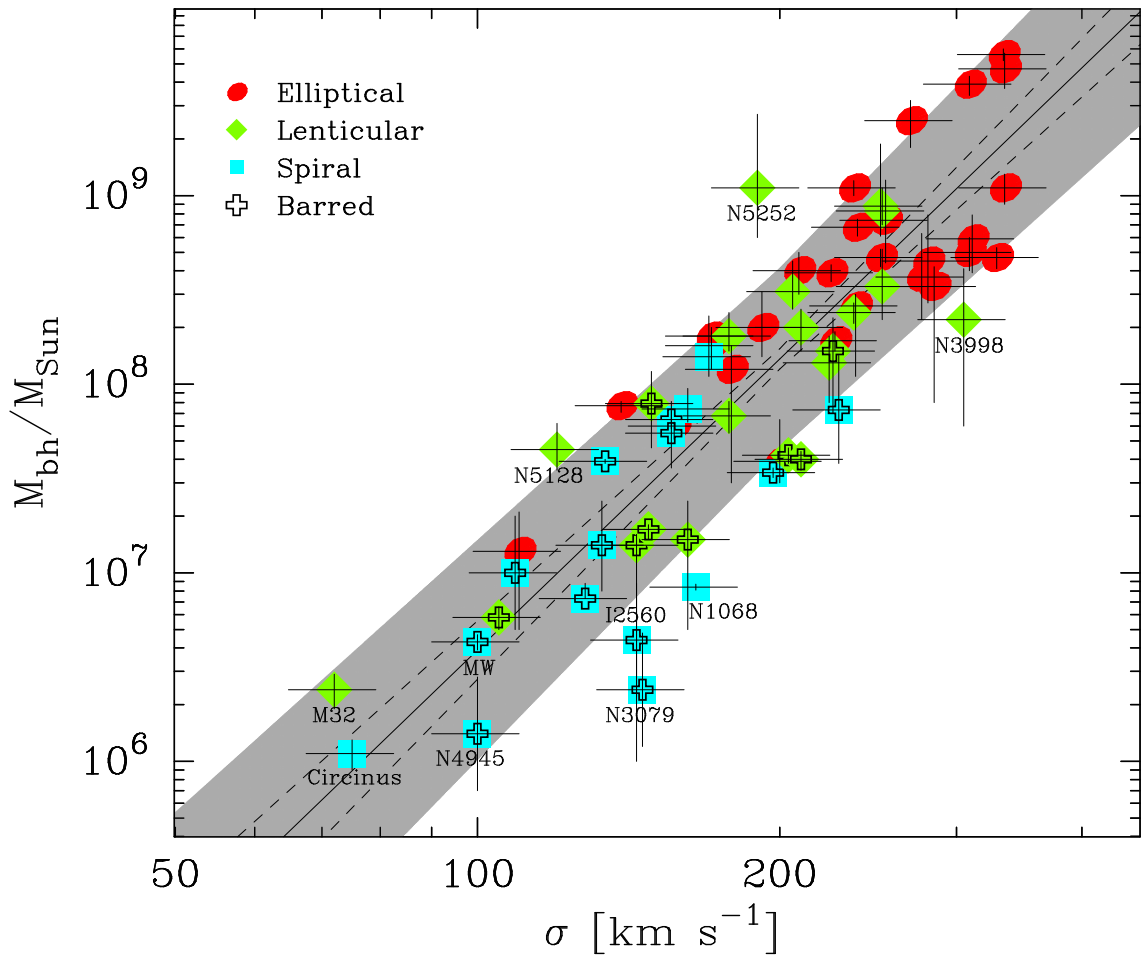


Figure 1.2: $M_{\bullet} - \sigma$ diagram for 64 galaxies. The barred galaxies are marked with a cross. Excluding these galaxies reduces the scatter. Figure taken from Graham et al. (2011).

1.3.2 $M_{\text{CMO}}-\sigma$ Relation

After finding the tight $M_{\bullet} - \sigma_e$ relation, the question is as to whether NCs obey a similar relation with the bulge component of the host galaxy. Wehner & Harris (2006) and Ferrarese et al. (2006) find similar correlations for NCs in early-type elliptical and late-type spiral galaxies. Feedback of stellar winds from O and B stars, and supernovae in NCs, could be responsible for the similar correlations of NCs with their host galaxy spheroid (McLaughlin et al., 2006). This leaves the questions of why only intermediate bright galaxies tend to form NCs and why do bright galaxies contain SMBHs instead of NCs. Figure 1.3 shows the CMOs of the Virgo Cluster Survey, with masses of SMBHs from the sample presented in Ferrarese & Ford (2005) and masses of NCs measured photometrically by using an appropriate M/L (Ferrarese et al., 2006). The masses of SMBHs and NCs, both correlate with the total mass of the host galaxy and build the relation $M_{\text{CMO}} - M_{\text{bul}}$. Even more remarkably, for a given velocity dispersions σ_e , NCs tend to have 10 times more mass than a SMBH.

These findings suggest that the formation of a CMO is a part of galaxy evolution. NCs and SMBHs can coexist. Our Milky Way galaxy is the most prominent example, but study of NCs and AGNs provide more evidence of the co-existence of NC and SMBH (Seth et al., 2008a; Graham et al., 2011). Therefore, the study of NCs provide us with the possibility for understanding the common growth history of CMOs in galaxies.

1.4 Formation and Evolution of Disc Galaxies

Presently, in the most favoured theory of structure formation in the Universe, Λ CDM, galaxies form in a hierarchy of merging haloes (Steinmetz & Navarro, 2002). In this standard model, massive elliptical galaxies most likely form in dissipationless

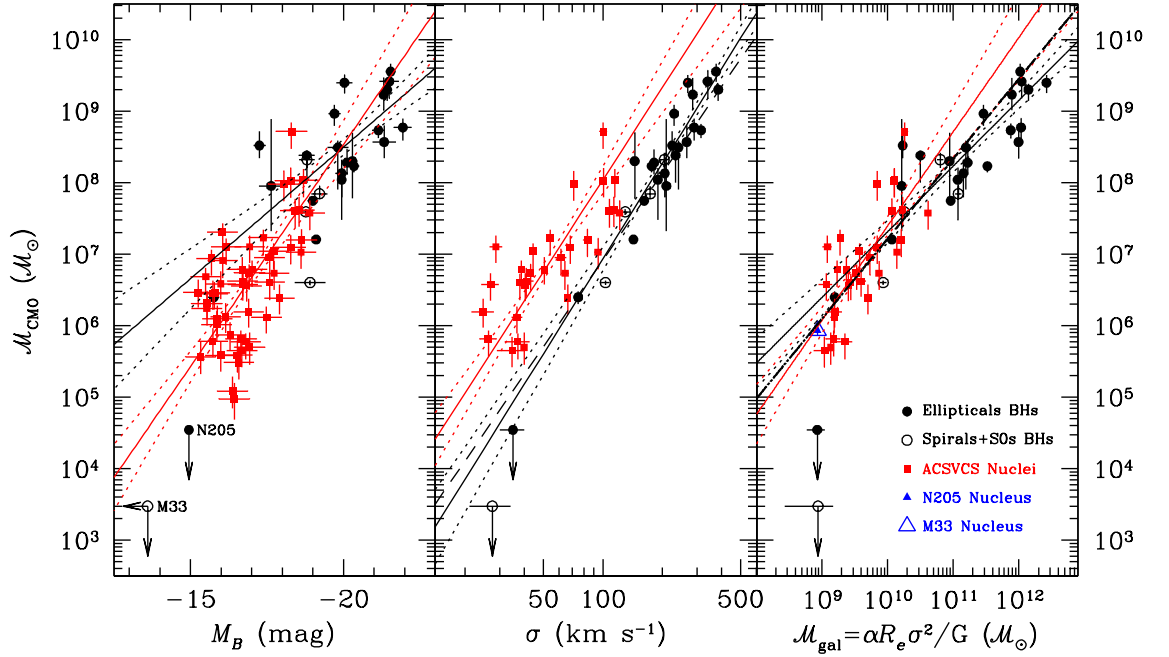


Figure 1.3: Left panel - Mass of the CMO plotted against absolute blue magnitude of the host galaxy (or bulge for spiral galaxies). NCs from the ACS Virgo Cluster Survey are shown as red squares. The SMBHs in early-type and spiral galaxies are shown as filled and open circles, respectively. Middle panel - CMO mass as a function of the velocity dispersion of the host galaxy, measured within R_{eff} . Right panel - CMO mass plotted against galaxy mass. In all panels, the solid red and black lines show the best fits to the NCs and early-type SMBH samples, respectively, with 1σ confidence levels shown by the dotted lines. In the middle panel, the dashed line is the best-fit SMBH relation of Tremaine et al. (2002). In the right panel, the dashed line is the fit obtained for the combined NC+SMBH sample. Figure taken from Ferrarese et al. (2006).

or also called *dry mergers* of elliptical progenitors (Khochfar & Burkert, 2005; Naab et al., 2006; Cox et al., 2006; Naab & Ostriker, 2009), while lower mass ellipticals are forming in dissipational or *wet mergers* of disc galaxies (Naab et al., 1999; Naab & Burkert, 2003). On the other hand, disc galaxies form out of cooling gas within the halo and build a rotationally supported disc of stars (White & Rees, 1978; Fall & Efstathiou, 1980). The first simulations were carried out by Katz (1991) and Katz et al. (1992). They investigated the collapse of a uniformly rotating, initially expanding spherical state with imposed small-scale irregularities predicted in a CDM universe. They found rotationally supported discs in simulations with a moderate amount of initial irregularity, but for initial conditions with a higher degree of irregularity, stars formed earlier in subclumps prior the main collapse, thus the stellar systems were more spheroidal. Higher resolution smoothed particle hydrodynamics Λ CDM cosmological simulations confirmed that during the merger of dark matter halos, which forms larger objects, the gaseous cores transfer most of their angular momentum to the dark matter halo and form a compact and bulge dominated disc galaxy (Navarro & Benz, 1991; Navarro & White, 1994). In full Λ CDM cosmological simulations, the formation of such discs is still a challenge (Steinmetz & Navarro, 1999; Navarro & Steinmetz, 2000; Abadi et al., 2003; Governato et al., 2004). In recent simulations, the formation of bulgeless disc galaxies with observed properties are produced by Governato et al. (2009); Brook et al. (2010) and Brooks et al. (2011). These simulations include feedback from supernovae and stellar winds to prevent the collapse of gas with low angular momentum in to the centre of dark matter haloes and therefore prevent the formation of a classical bulge component.

Recent surveys (*e.g.* COSMOS (Scoville et al., 2007)) found that disc galaxies are already present at $z \sim 1$ and beyond (Jones et al., 2010). Therefore, in the present theory of galaxy formation, disc galaxies assemble from the smooth accretion of gas cooling inside a halo, while gas with low angular momentum driven to the centre by

hierarchical mergers forms stars within a bulge component. These assembled discs do not have to be in a stable state, thus dynamical processes are able to redistribute energy and angular momentum within the disc. These internal secular processes are forming the variety of spiral structures in disc galaxies. These dynamical processes are slower compared to merger processes and, therefore only play a significant role at lower redshifts, when the merger rate is lower. Secular evolution must have played a significant role in the evolution of structural properties of disc galaxies since we observe them at $z < 2$ (MacArthur et al., 2003; Debattista et al., 2004; Avila-Reese et al., 2005; Combes, 2005; Debattista et al., 2006a). Presently, it is not clear what role these processes have played in the evolution of the scaling relation between CMOs and their host galaxies. In the second part of this thesis, I study the consequences of bar formation in the evolution of the $M_{\bullet} - \sigma_e$ relation.

1.4.1 Bar Formation in Galaxies

The most prominent features in disc galaxies are spiral arms. Disc galaxies are divided into two different types. Galaxies in the first class are known as '*grand design spirals*', which have two long and prominent spiral arms and make up 10% of all disc galaxies. The second class of galaxies have shorter and more fragmented spiral arms. Those disc galaxies are called '*flocculent spirals*' and they make up 90% of all disc galaxies.

The second prominent feature of disc galaxies is a bar in the central region of the galaxy. Bars lead to a redistribution of angular momentum, and an increase in the central mass density. Hohl (1971) found that a single disc results in a double exponential profile due to the formation of a bar. Therefore bars are suggested as one possible mechanism to fuel central starbursts and AGN. However, bars are more likely to be detected in old stellar components and in near infrared surveys (Combes, 2003). The high ratio of barred-galaxies to AGN in the nearby universe seems to

argue against this as a common phenomenon (McLeod & Rieke, 1995; Mulchaey & Regan, 1997).

Stars in disc galaxies are rotating around the centre on nearly circular orbits, which means that the circular velocity v_c is greater than the velocity dispersion of the stars σ . The circular velocity profiles $v_c(R)$ of disc galaxies often rise very quickly from the centre, depending on whether a bulge component is present. At greater radii $v_c(R)$ flattens and stays constant. This was first noticed by Rubin & Ford (1970) and is evidence for dark matter in disc galaxies, because v_c remains constant even when the luminosity profile of the disc declines. When the disc is in differential rotation the variation of angular frequency $\Omega(R)$ is such that the inner part rotate many times faster than stars in the outer parts. Thus if the stars in the spiral arm remain in the arm, differential rotation will wind up the arm very quickly. This winding problem was recognised very early by Wilczynski (1896) and by Lindblad (1925).

A disc galaxy can be ideally described with an axisymmetric potential and the orbits can be represented in cylindrical coordinates (R, ϕ, z) . Stars orbiting in the equatorial plane do not recognise whether the potential is spherically symmetric or not. Thus the stars orbit around the centre in a non-closed orbit with a radial period T_r and an azimuthal period T_ϕ . The radius of a given star oscillates about a radius R , which is also called the guiding centre radius R_g . Thus, if one watches the orbit from a frame which rotates at azimuthal frequency $\Omega_p = \Omega_\phi = 2\pi/T_\phi$, the orbit of the star would describe a circle around R_g with the angular frequency $\Omega_r = 2\pi/T_r$. This frequency $\kappa = 2\pi/T_r$ is called the epicyclic frequency. If one watches the orbit in a frame with angular frequency Ω , the azimuthal angle changes by $\Delta\phi_p = \Delta\phi - \Omega_p T_r$, where $\Delta\phi$ is the change of angle ϕ in the non-rotating frame, so that the orbit in this rotating frame can be seen as closed, if $\Delta\phi = 2\pi\frac{n}{m}$, where

m, n are positive integers. The orbit of the star is closed at m radial oscillations:

$$\Omega_p = \Omega_\phi - \frac{n\Omega_r}{m} \simeq \Omega - \frac{n\kappa}{m} . \quad (1.8)$$

The frequencies $\Omega(R)$ and $\kappa(R)$ both of which depend on the radius within the galaxy. However it was Lindblad (1925) who found that while most of the $\Omega - \frac{n\kappa}{m}$ curves vary rapidly over the radius of the galaxy, the frequencies for $n = 1$ and $m = 2$ or $n = 2$ and $m = 4$ are constant across the galaxy. That means, for a given galaxy with pattern speed Ω , there exists closed orbits covering a wide range of radii with epicyclic frequency κ , and one can build bar like structures with those arranged orbits of stars. This bar is stationary in the rotating frame and oscillating with pattern speed Ω in the inertial frame. If the orbits of stars are shifted relative to each other, spiral structures with different configurations can be created (see Figure 6.12 in Binney & Tremaine, 2008). Thus, the spiral arms are described as density waves and these type of density waves are called kinematic density waves (Lindblad, 1925; Kalnajs, 1973).

In disc galaxies, the potential due to spiral patterns cannot be described by an axisymmetric potential, because the spiral arms are a non-axisymmetric component of the gravitational potential. Spiral arms perturb the gravitational field and they produce a drift of the orbits of stars as a long-lived density wave within the disc. The response to a perturbation of the gravitational field can be achieved by finding the resonant orbits. In a rotating frame a stationary gravitational field is given by $\Phi_s(R, \phi, t) = \Phi(R, \phi - \Omega_p t)$. For example, a bar like structure has a well defined pattern speed Ω_p . The perturbation can be expanded to

$$\Phi_s(R, \phi - \Omega_p t) = \sum A_m \cos m(\phi - \Omega_p t) . \quad (1.9)$$

The resonances occur when the frequency of the perturbed field equals the epicyclic frequency of the stars, hence $\frac{d}{dt}m(\phi - \Omega_p t) = m(\Omega - \Omega_p) = 0, \pm\kappa$. For a bar $m = 2$ the resonances are:

- $\Omega - \Omega_p = 0$, the star co-rotates (CR) with the perturbation and experiences persistent perturbation
- $\Omega - \Omega_p = \kappa/2$, inner Lindblad resonance (ILR), the star experiences a periodic perturbation at its radial frequency
- $\Omega - \Omega_p = -\kappa/2$, outer Lindblad resonance (OLR)

The resonances occurs at specific radii for a given differentially rotating disc. A static density wave with pattern speed Ω_p can persist when the Lindblad resonances are satisfied. The orbital structure of stars within the bar can be described by periodic orbits, so called x_1 orbits. As seen before, stars on those orbits are like ellipses which are aligned with the major axis and centred of the bar (Contopoulos & Papayannopoulos, 1980; Athanassoula, 1992). The axis ratio of the orbits increases with increasing pericentre and is maximal near co-rotation. Depending on the strength and the mass of the bar, a family of orbits called x_2 can be present. These orbits are perpendicular to the bar, and their maximum extent is less than or of similar order as the bar minor axis (Athanassoula, 1992).

Bars evolve within the disc and thus they must be born as a thin component. Similar to the resonances within the equatorial plane of the disc as described before, resonances also occur in vertical direction. These vertical resonances thicken the bar, because stars are scattered within a vertical ILR, $\Omega_b = \Omega - \nu/2$, where ν is the vertical frequency. It has been suggested that bars are efficient at forming stellar bulgelike structures (Combes et al., 1990). Another process forming bulgelike structures can occur through collisionless buckling instabilities (Raha et al., 1991). These lead to the bending of the bar perpendicular to the plane of the disc. The buckling is a result of vertical anisotropy (Merritt & Hernquist, 1991; Merritt & Sellwood, 1994), which leads to a vertical heating of disc stars (Saha et al., 2010). At the same time buckling weakens a bar. The key signature of this process is the boxy/peanut-shaped density distributions of gas and stars when a galaxy is

seen edge-on (Kuijken & Merrifield, 1995; Merrifield & Kuijken, 1999; Bureau & Athanassoula, 1999).

1.5 Formation Scenarios of Nuclear Clusters

Two main scenarios have been proposed to explain the formation of NCs. One scenario relies on NCs forming in situ out of gas falling into the centre (Shlosman & Begelman, 1989; Maciejewski et al., 2002; Maciejewski, 2004a,b). Alternatively, NCs may form from the merging of star clusters after sinking to the centre under the action of dynamical friction (Tremaine et al., 1975; Miocchi et al., 2006).

1.5.1 Radial Transport of Gas into the Centre

A number of mechanisms have been proposed for driving gas to the centre. The problem of fuelling the inner central region is that there is a need for different pathways from the outer to the inner region. Shlosman et al. (1989) suggests that the main components are bar-driven inflow at large radii ~ 1 kpc, and self-gravitating disc of clouds at radii ~ 100 pc bringing the gas closer due to cloud-cloud mergers. Numerical studies of gas dynamics, star formation and chemical evolution within 1 kpc of dwarf elliptical galaxies produce dense stellar systems, however it cannot provide a clear explanation of the correlations between the dynamical properties of NCs and their host galaxy (Bekki et al., 2006). Besides, NCs are also found in unbarred galaxies and in these galaxies there is no evidence of departure from axisymmetry. Milosavljević (2004) finds that radial transport of interstellar gas due to the magneto-rotational instability within the galactic disc is sufficient to drag the gas towards the inner 100 pc. After the formation of a NC, stellar winds and supernova blast waves prevent further star formation during 50 Myrs, the lifetime of O and B stars. After the stars with masses of $8 M_{\odot}$ have been expended, fresh

gas returns to the NC and accumulates toward a subsequent starburst. The star formation history of an NC is therefore punctuated by periodic starbursts separated by ~ 100 Myrs (Milosavljević, 2004). High resolution interferometric observations of the line-emission of CO and HCN molecules of the nuclear region in the nearby late-type spiral galaxy IC 342 show that mechanical feedback from recent star formation activity affects the gas inflow caused by a large stellar bar (Schinnerer et al., 2003, 2008). The balance between feedback from star formation and fuelling efficiency appears to regulate the rate of nuclear star formation and could explain the repetitive star formation episodes seen in NCs (Walcher et al., 2006; Rossa et al., 2006). However, high-accuracy hydrodynamical simulations of the gas flow in barred galaxies with an imposed potential of a single or double bar have shown that the second bar does not enhance the gas inflow into the central region, rather the secondary bar can prevent the gas inflow (Maciejewski et al., 2002).

1.5.2 Merger Scenario

Stellar systems like GCs in the halo of galaxies and star clusters (SCs) in the main disc and bulge component will lose the kinetic energy of their orbital motion due to dynamical friction. The latter is given by

$$\frac{d\vec{v}_M}{dt} = -16\pi^2 G^2 M m_a \ln \Lambda \left[\int_0^{v_M} dv_a v_a^2 f(v_a) \right] \frac{\vec{v}_M}{v_M^3} \quad (1.10)$$

(Chandrasekhar, 1943) where G is the gravitational constant, the subject body mass is M and its velocity is v_M , the mass of the field stars is m_a , the distribution of velocities is given by the integral over the distribution function $v_a^2 f(v_a)$ and $\ln \Lambda$ is the Coulomb logarithm. The acceleration is proportional to the mass of the GC or SC and the dynamical friction force is proportional to the square of its mass. In a study of dwarf elliptical galaxies in the Virgo and Fornax Cluster, Lotz et al. (2001) find a depletion of the most massive GCs radial distribution compared to the total GC distribution, which is shown in Figure 1.4. The colours of the GC

populations and NC are similar and seem to be bluer than those of the underlying field star population. The coalescence of GCs within the centre is consistent with the correlations between nuclear colour and luminosity, and the host galaxy (Lotz et al., 2004). Thus one plausible explanation for the depletion of the radial distribution of the most massive GCs is that they have merged within the centre of the galaxy, because of their smaller infall timescales.

However, Milosavljević (2004) also finds that in late-type spiral galaxies the timescale for the inspiral of GCs due to dynamical friction is long. He calculates the timescale for the decay of GCs assuming an exponential disc embedded within a spherical dark matter halo. Then, the dynamical friction can be calculated from $t \sim v_c^3 / 4\pi G^2 M \rho \ln \Lambda$ (Chandrasekhar 1943a), where v_c is the circular velocity of the GC, ρ the density of the dark matter halo and $\ln \Lambda$ the Coulomb logarithm. For the density, Milosavljević (2004) uses $\rho = (3 - \gamma) v_c^2 / 4\pi G r^2$ with $\gamma = 1$. Thus the timescale for the infall of a GC can be estimated from

$$t \geq 3 \times 10^9 \text{yr} \frac{v_{\text{circ}}}{50 \text{ km s}^{-1}} \left(\frac{r}{1 \text{kpc}} \right)^2 \left(\frac{M_{\text{GC}}}{10^6 M_{\odot}} \right)^{-1}. \quad (1.11)$$

In fact, GCs have to be more massive than $10^6 M_{\odot}$ and have to be within the region of < 1 kpc, otherwise the timescale for spiralling into the inner region of the galaxy will be > 3 Gyrs. Even so, five GCs in the Fornax dwarf spheroidal galaxy seem to be orbiting at a projected distance of 1 kpc. N -body simulations and analytical calculations have revealed that a constant density core within 1 kpc would inhibit an infall altogether (Read et al., 2006; Goerdt et al., 2008, 2010). Nonetheless, self-consistent simulations have found that mergers do occur within a bulge component (Capuzzo-Dolcetta & Miocchi, 2008b) and the resulting NC has structural parameters that are consistent with those observed (Bekki et al., 2004; Miocchi et al., 2006; Capuzzo-Dolcetta & Miocchi, 2008a,b).

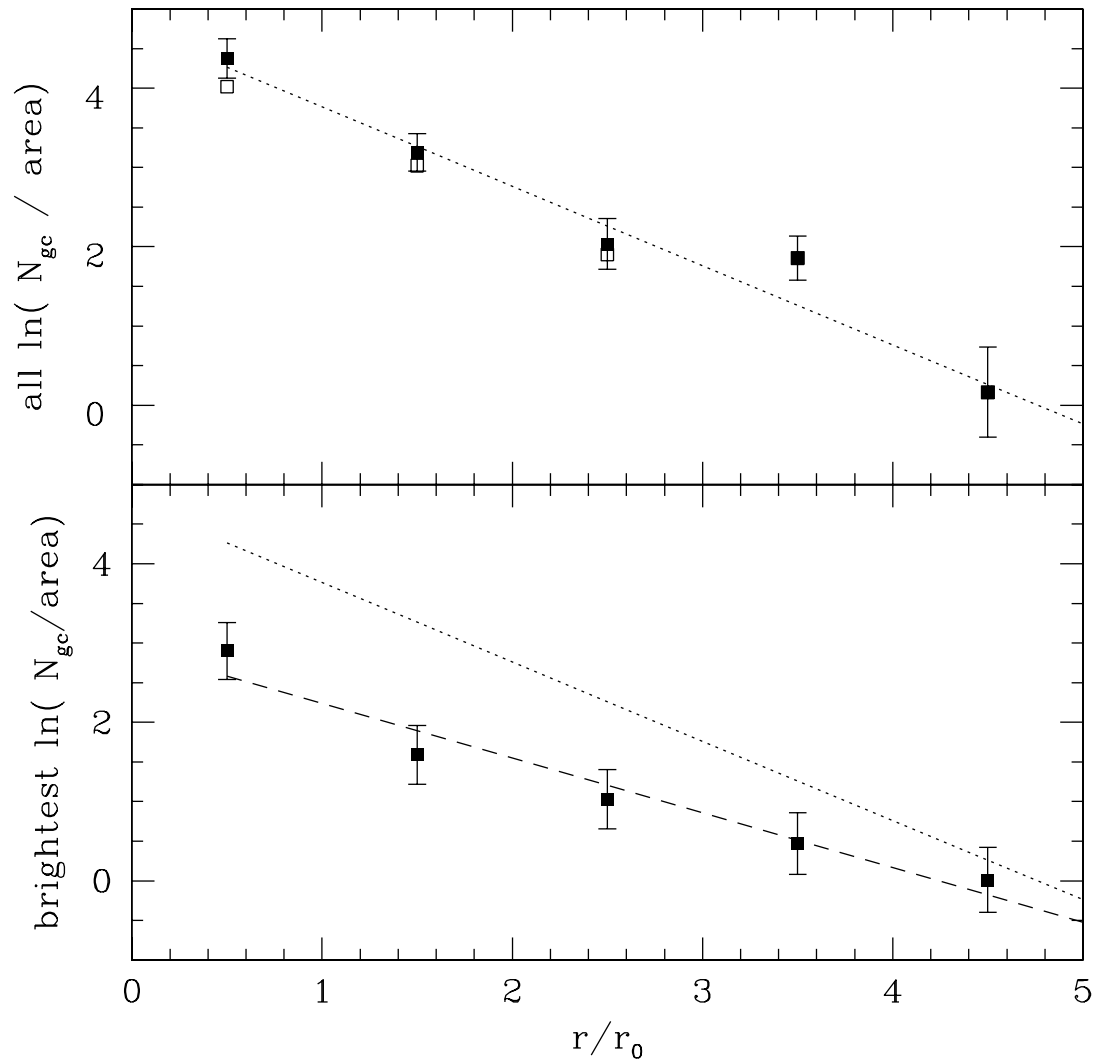


Figure 1.4: Top - Radial distribution of globular clusters scaled to the scale length of the galaxy. Possible NCs have been excluded. The total GC surface density follows the exponential light profile of the dwarf elliptical's, but the bright clusters $M_V < -8.0$ appear to be depleted (Lotz et al., 2001). The open squares show the summed profile without incompleteness correction in the inner region. Figure taken from Lotz et al. (2001).

1.6 Nuclear Cluster Formation in Spiral Galaxies

NC formation in late-type spiral galaxies is an ongoing process, because stars younger than 100 Myrs are present and the star formation histories of NCs are extended and possibly constant (Rossa et al., 2006; Walcher et al., 2006). Mergers and accretion of *old* SCs is thus not a viable formation scenario, regardless of whether enough such SCs are available.

However, mergers and accretion of *young* SCs formed near the centres of galaxies, such as those observed in the Milky Way (Figer et al., 1999, 2002), could still provide a viable formation mechanism. Recent HST observations have found a candidate SC in the inner few hundred parsecs of the galaxy NGC 2139 (Andersen et al., 2008), while Kornei & McCrady (2009) have observed a super star cluster in the nuclear region of NGC 253. Therefore SCs exist in the inner region of galaxies and the supply of young SCs to the inner regions may be enhanced because tidal forces are compressive within 10% of the effective radius when the density profile has a Sérsic index $n < 2$ (Emsellem & van de Ven, 2008). It is plausible that even if the infall of gas due to non-axisymmetric or magneto-rotational instabilities is efficient, tidal torques are sufficient to compress molecular clouds and induce star formation. Thus NC formation could occur mainly by the accretion of young SCs.

Agarwal & Milosavljević (2011) used analytic modelling to show that infalling SCs from an empirical SC population produce NCs of the right mass in isolated spheroidal and late-type galaxies. Such SCs must form quite close to the galaxy centres ($\lesssim 1$ kpc), otherwise the timescales for infall due to dynamical friction are prohibitively long (Milosavljević, 2004). In a study of gas-kinematics in bulgeless spiral galaxies, Neumayer et al. (2011) find that for SCs with masses $> 2 \times 10^5 M_{\odot}$ the dynamical friction timescales are < 2 Gyrs within 500 pc.

More recent observations have to be taken into account to shed light on the evolution and formation of NCs. In a study of 14 nearby edge-on late-type galaxies

with the HST, Seth et al. (2006) find nine NCs. Moreover, this study reveals that not all NCs have single component structures. In Figure 1.5, HST F814W images of the nine NCs show in the three cases, IC 5052, NGC 4206 and NGC 4244, an elongated disc or ring component and a spheroidal component. These components are compact and they physically overlap. In two other galaxies NGC 4517 and NGC 5023, the NCs tend to show evidence for similar structures. Thus NCs seem to be multi-component stellar clusters with flattened, compound structures.

The dimensions and scales of the NCs are determined by two dimensional fitting with analytical functions, e.g. elliptical King and Sérsic profiles. The median axis ratio $q = b/a$ is 0.81, where a and b are the semi major and semi minor axis. The NCs in NGC 4206 and NGC 4244 have $q \sim 0.5$ and they have the most prominent nuclear cluster discs (NCDs). The major axis of the three discs in IC 5052, NGC 4206 and NGC 4244 are aligned within 10° of the major axis of the main galaxy discs. The NCs have R_{eff} of ~ 3 pc, which are in agreement with other observed NCs (Böker et al., 2004; Walcher et al., 2006).

More fascinating is the fact that the compound structures are related with the different stellar populations in these NCs. The colour maps revealed from the HST F814W and F606W observations are presented in Figure 1.6. The NCDs are 0.3–0.6 magnitudes bluer than the reddest parts in the spheroidal component. The colour of F606W- F814W $\simeq 0.65$ indicates that the NCD component consists of a younger (< 1 Gyr) single stellar population. Further evidence of a young single stellar population comes from the analysis of the spectra of NGC 4244, which confirms a stellar population younger than 100 Myrs. This analysis is in agreement with the spectral analysis of NCs in late-spiral galaxies (Walcher et al., 2006). The analysis with model spectra obtained with stellar population models (*e.g.* Maraston, 2005; Kotulla et al., 2009) shows that at least three different stellar populations are present. The best fitting results are obtained by using a constant star formation

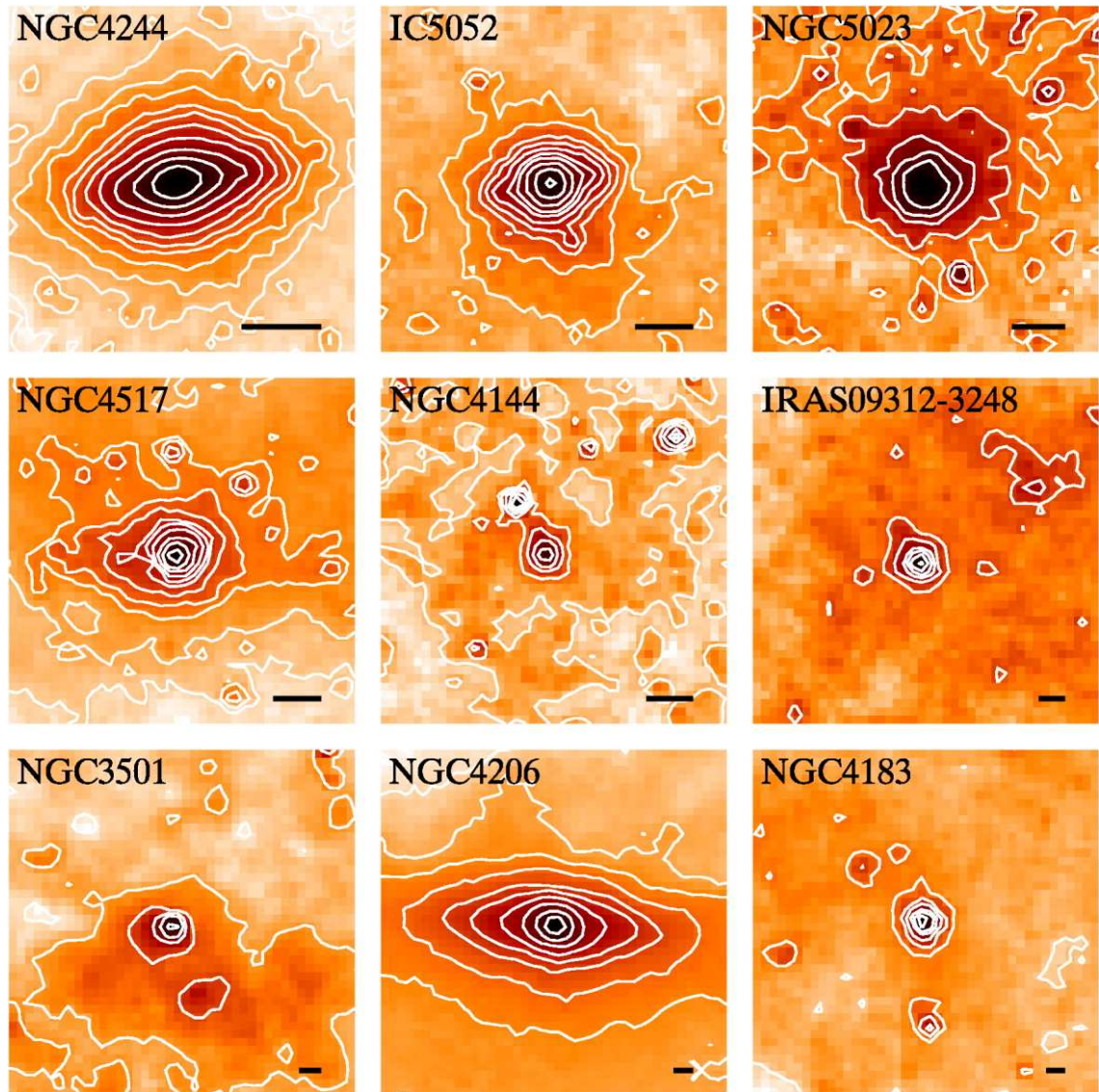


Figure 1.5: HST F814W images of the nine NC candidates. The images are rotated so that the x axis is aligned with the position angle of the major axis of the galaxy main disc. The black solid line indicates a length of 10 pc. Image taken from Seth et al. (2006).

rate, which shows that even more than three stellar populations must be present. Thus NCs have a complex star formation history as found by Rossa et al. (2006). The total dynamical mass of the NC in NGC 4244 is $2.5_{-1.2}^{+1.7} \times 10^6 M_{\odot}$, where the young stellar population within the NCD component is about $\sim 5\%$ of the total NC's mass (Seth et al., 2006).

New two dimensional integral field data from Gemini Near-Infrared Integral Spectrograph (NIFS) provide an analysis of the kinematics in NCs and will give further constraints on their formation. Figure 1.7 shows the line-of-sight velocity, where spectra are binned together to provide a signal to noise level (S/N) of around 25. The *K*-band images for morphological analysis are reconstructed from the spectra. The velocity and velocity dispersions of the NCs in NGC 4244 and M33 show that they are rotating fast.

1.7 Outline for the thesis

Observations of NCs give further insights on the formation of CMOs in galaxies. The role of SC mergers has been studied by Capuzzo-Dolcetta & Miocchi (2008b) and Bekki et al. (2004), but new observations of NCs in edge-on late-type spiral galaxies as presented in Section 1.6 give further constraints on their formation. Do those findings rule out the merger or accretion of SCs as one of the possible scenarios for NC formation? Bekki et al. (2004) found that a NC formed by a merger of GCs shows some rotation. The accretion without gas dissipation need not result in slowly rotating systems: Read et al. (2008) showed that satellite galaxies that accrete onto disc galaxies can get dragged down on to the plane of the disc and settle directly into a rapidly rotating thick disc. Likewise, Eliche-Moral et al. (2006) find that low density satellites can accrete onto bulges and end up in a rapidly rotating disc component. Can NCDs form through an analogous process? Since SCs falling into the nucleus are likely to have formed in the mid-plane of the galaxy,

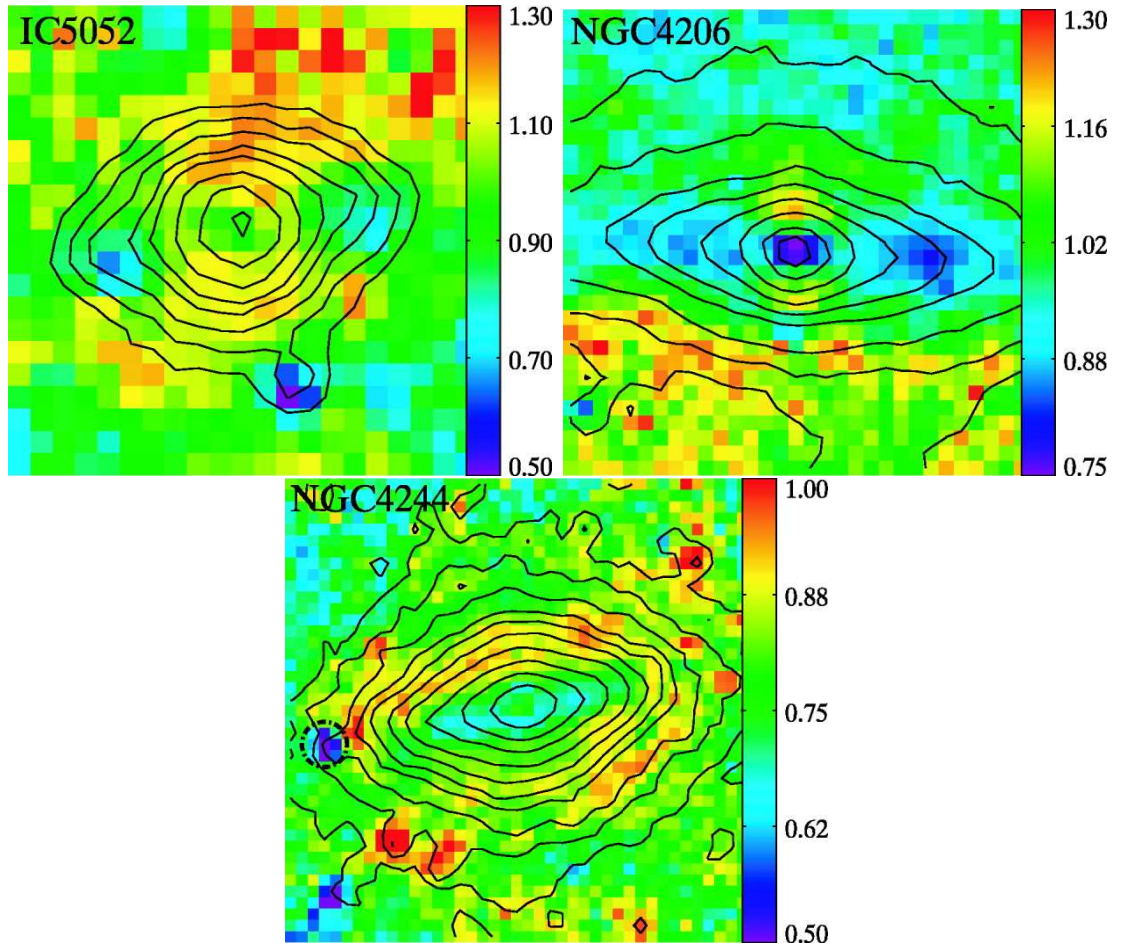


Figure 1.6: Colour maps of the HST F606W and F814W observations. The contours are showing the F606W brightness over plotted with black lines. The colour bars are indicating the colour values. The NCD components show bluer colours than the spheroidal component, indicating a younger stellar population. The circled region in NGC 4244 is a HII low mass star forming region. Images taken from Seth et al. (2006).

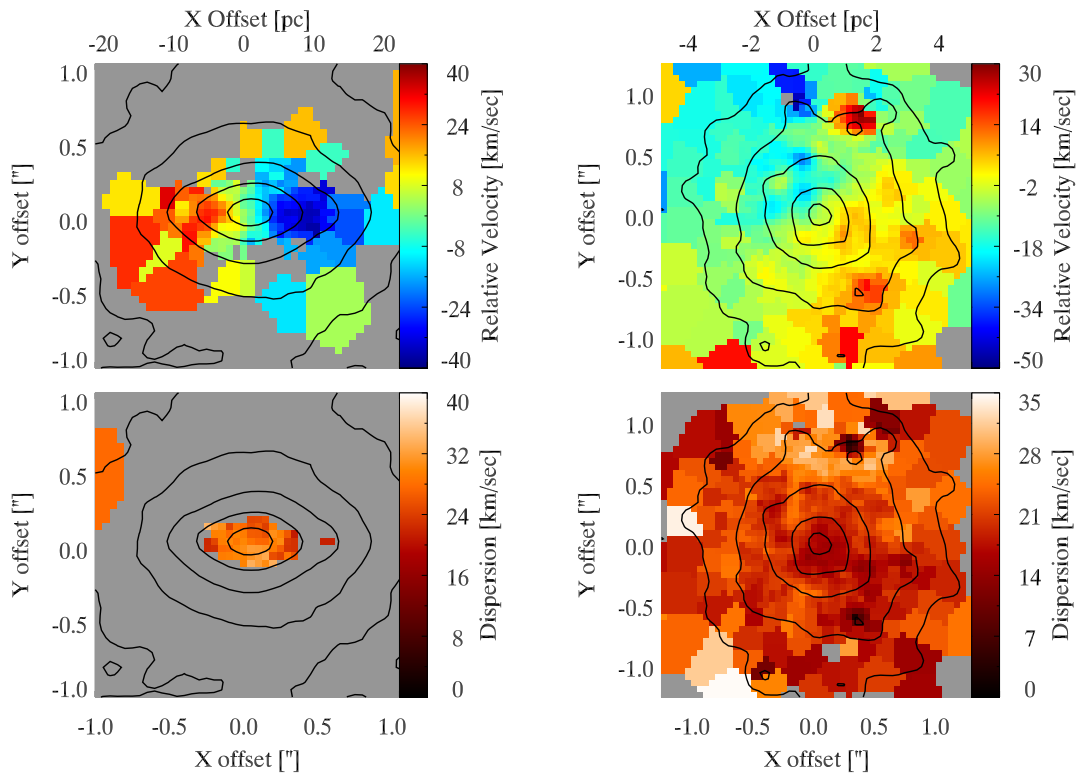


Figure 1.7: Top - Colour indicates the measured radial velocity observed with NIFS. Grey areas show spectra with $S/N < 10$ and/or errors $> 10 \text{ km s}^{-1}$. Contours are from the K -band images. There is rotation of $\sim 30 \text{ km s}^{-1}$ along the major axis and above in the spheroidal component. Bottom - Velocity dispersion measurements with $S/N > 10 \text{ km s}^{-1}$ and errors $< 5 \text{ km s}^{-1}$. On the left the NC in NGC 4244. The dispersion decreases with distance from the centre as for a cold disc population, whereas on the right the NC in M33 shows no disc component due to its inclination of 49° . However the NC also shows high rotation and a decline in its velocity dispersion with increasing distance from the centre.

they will generally share in its rotation. In Chapter 2, I will use the most recent observations to identify further observables and to model the kinematics of the NCs in NGC 4244 and M33. In Chapter 3, I will compare a suite of N -body simulations with the observations to distinguish between the proposed formation scenarios for NCs in galaxies.

Disc galaxies are present at redshifts $z < 2$. While elliptical galaxies and classical bulges in disc galaxies are believed to form by the merger of galaxies and the accretion of satellites (Eggen & Sandage, 1962; Tremaine et al., 1975; Searle & Zinn, 1978; Kauffmann et al., 1993; Baugh et al., 1996; van den Bosch, 1998), the evolution of the of the $M_{\bullet} - \sigma_e$ relation has been studied in numerous simulations of galaxy mergers (Kazantzidis et al., 2005; Robertson et al., 2006; Younger et al., 2008; Johansson et al., 2009). Unlike elliptical galaxies, classical bulges evolve along with the disc they are surrounded by. Non-axisymmetric features such as bars and spirals redistribute angular momentum and are driving the secular evolution in disc galaxies (*e.g.* Friedli & Benz, 1995; Athanassoula, 1992; Kormendy & Kennicutt, 2004; Debattista et al., 2006a). Bars are very common in local galaxies and their fraction remain similar until redshift $z \sim 1$ (Jogee et al., 2004; Elmegreen et al., 2004), which indicates that they are long-lived features with lifetimes > 2 Gyrs (Jogee et al., 2005). Thus their influence on the shape and structure of the galaxy is significant. As shown in Section 1.3 the $M_{\bullet} - \sigma_e$ relation seems to be different in ellipticals, classical bulges and pseudo bulges (Hu, 2008; Gadotti & Kauffmann, 2009). The offset of bulges in barred galaxies from the $M_{\bullet} - \sigma_e$ relation of unbarred galaxies (Graham et al., 2011) indicate that bar formation influences the kinematics of the disc and bulge. In a suite of disc galaxy simulations I will explore the effect of bar formation on the $M_{\bullet} - \sigma_e$ relation of classical bulges, under the assumption that classical bulges form with a SMBH satisfying the $M_{\bullet} - \sigma_e$ relation and later a bar forms within the disc.

Chapter 2

Integral Field observations of NGC 4244 and M33

I compare my simulations with observations of the NCs in two nearby galaxies, M33 and NGC 4244. These two galaxies provide me with well-resolved nuclei for which integral field kinematic data are available. While M33 is inclined by $i = 49^\circ$ (Corbelli & Schneider, 1997), NGC 4244 is an edge-on galaxy. These two objects thus give me two different perspectives for studying the morphology and kinematics of NCs in disc galaxies. For the distances I assume 4.4 Mpc for NGC 4244 (Seth et al., 2005) and 0.8 Mpc for M33 (Lauer et al., 1998).

2.1 Spectroscopy and isophotal shape of NGC 4244 and M33

Seth et al. (2006) presented HST F814W photometry of the NC in NGC 4244, which is resolved into a nuclear cluster spheroid (NCS) and a bluer nuclear cluster disc (NCD). The half mass radius, R_{eff} , of the NC obtained by fitting a King profile to the ACS/F814W images (Seth et al., 2006) is about 5 pc.

Here I use K -band spectra of NGC 4244 (Seth et al., 2008b) and M33 (Seth et al, in prep) obtained at Gemini North with the Near-Infrared Integral Field spectrograph (NIFS), an image slicing field unit spectrograph. The PSF core in both observations is $\sim 0''.1$ FWHM, with final data cubes sampled with $0''.05$ pixels. In NGC 4244, this corresponds to $1.06 \text{ pc pixel}^{-1}$, while in M33 the pixel scale is $0.19 \text{ pc pixel}^{-1}$. The line-of-sight velocities are determined by the fitting method pPXF of Cappellari & Emsellem (2004). The code uses a Gauss-Hermite series including the non-Gaussian terms h3 and h4 (van der Marel & Franx, 1993) to fit the line-of-sight velocities. The imperfect adaptive optics corrections result in nearly half of the light being a scattered PSF halo ($\sim 0''.7$ FWHM). This leads to problems separating the rotation in the NCS and NCD in NGC 4244 (see Section 2.3.2). In both clusters, the rotation amplitude increases with radius out to the effective radius, and decreases at larger radii. However, whether or not a NCD is present in the NC of M33 cannot be determined because of the galaxy's inclination. In Figure 2.1, I show the line-of-sight velocity profiles of M33 and NGC 4244.

The shape of an isophote can be quantified by the Fourier coefficients of the expansion

$$I(\phi) = I_0 + \sum_{n=1}^{\infty} A_n \sin(n\phi) + B_n \cos(n\phi) \quad (2.1)$$

where I_0 is the mean intensity along the ellipse, ϕ is the azimuthal angle and A_n , B_n ($n = 1, 2, \dots$) are harmonic amplitudes. The ellipse which best fits the isophote has the coefficients A_n , B_n ($n = 1, 2$) equal to zero. The deviations from the best-fit isophote are then given by the higher order coefficients A_n , B_n ($n = 3, 4, \dots$). The leading residual term generally will be the $n = 4$ term, which determines whether the isophote is discy ($B_4 > 0$) or boxy ($B_4 < 0$). I use the task ELLIPSE in IRAF¹ to measure B_4 . The task ELLIPSE reads a two dimensional image and uses an iterative method described by (Jedrzejewski, 1987) to fit the isophote. The parameter B_4 has

¹<http://iraf.noao.edu/iraf/web/>

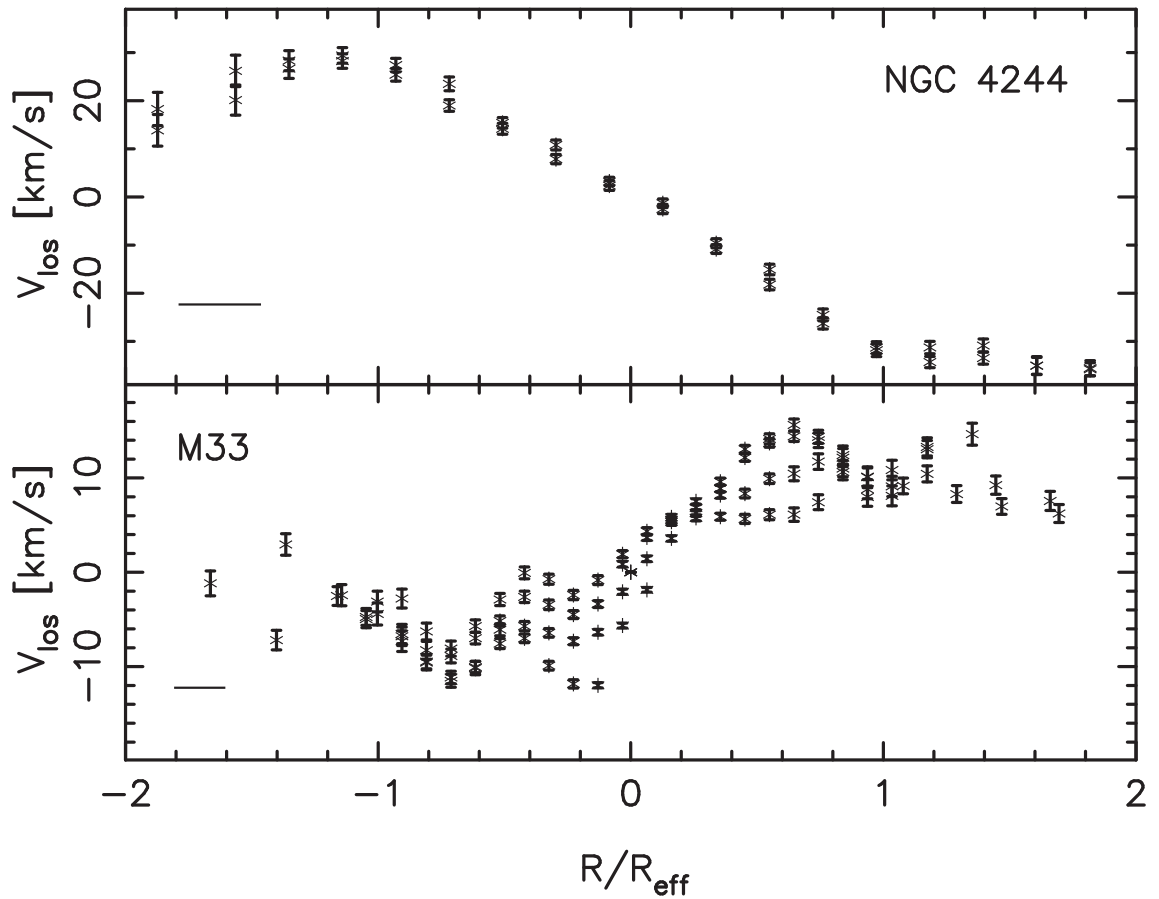


Figure 2.1: Profiles from the NIFS data (Seth et al., 2008b) of line-of-sight velocities along the major axis in NGC 4244 (top) and M33 (bottom). The kinematics were extracted from the integral-field data within a slit of $|z| < 0.4$ pc. This corresponds to $0.08 R_{\text{eff}}$ for NGC 4244 and $0.2 R_{\text{eff}}$ for M33. The line indicate the FWHM of the PSF.

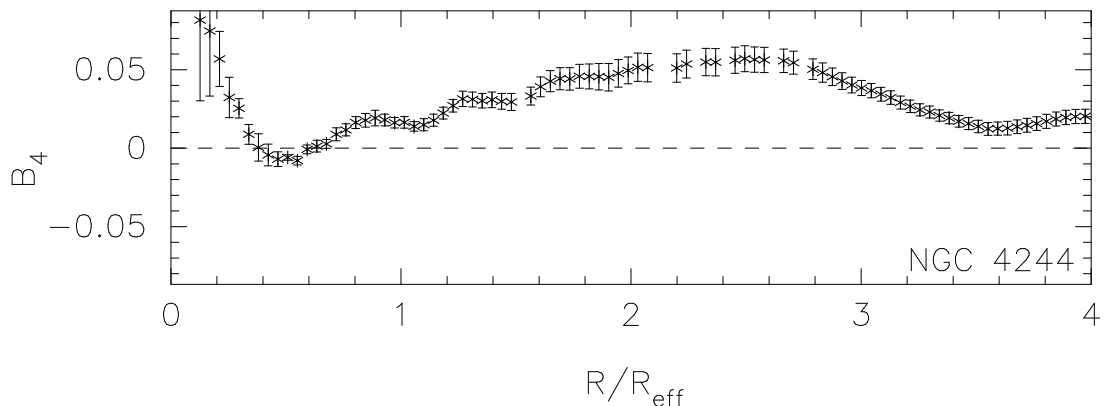


Figure 2.2: B_4 for the NC in NGC 4244 derived from the integrated K -band flux data (Seth et al., 2008b).

been shown to correlate with kinematic properties of the host galaxy in observations (Bender, 1988; Kormendy & Djorgovski, 1989; Kormendy & Bender, 1996) and in simulations of galaxy mergers (Naab et al., 1999; Naab & Burkert, 2003; Naab et al., 2006). This result was strongly confirmed with the large ATLAS^{3D} sample of early-type galaxies (Cappellari et al., 2011) which demonstrated that a significant disciness is an unambiguous indication of a fast rotating galaxy (Emsellem et al., 2011). Figure 2.2 shows B_4 for the NC in NGC 4244, which is clearly discy.

2.2 Axisymmetry of the M33 nucleus

The face-on axial symmetry is an important constraint on the formation of any stellar system. In general, the merger of stellar systems leads to triaxial systems, *e.g.* elliptical galaxies are found to be triaxial (Wagner et al., 1988; Naab et al., 1999; Naab & Burkert, 2003; Naab et al., 2006). Very little data are available for the face-on axial symmetry of NCs. For the NC in M33 I find evidence for axisymmetry. The inner $0''.5$ ($= 1.8$ pc) of the NC in M33 has an apparent $b/a = 0.84$, with an average position angle $PA = 19.3^\circ$ (Lauer et al., 1998), which is close to the PA of the inner disc $PA = 23^\circ \pm 1^\circ$ within $R < 4.0$ kpc (Zaritsky et al., 1989). Thus I

can assume that the NC is in the same plane as the inner disk and therefore it is possible to determine the NC's apparent axis ratio b/a . The galaxy is inclined by $i = 49^\circ$ (Corbelli & Schneider, 1997), so that an oblate spheroid of apparent axis ratio b/a at an inclination i would have an intrinsic vertical-to-horizontal axis-ratio q_0 given by

$$q_0 = \sqrt{\frac{(b/a)^2 - \cos^2 i}{\sin^2 i}} \quad (2.2)$$

(Hubble, 1926). The $q_0 \simeq 0.7$ that Eqn. 2.2 implies for M33's NC is fully consistent with the range of values of q_0 found in edge-on galaxies by Seth et al. (2006) (NGC 4244 having $q_0 \sim 0.5$). Moreover, I measured the kinematical $\text{PA}_{\text{kin}} = 36^\circ \pm 18^\circ$ (1σ error) from the NIFS integral-field kinematics, with the routine `FIT_KINEMATIC_PA` described in Appendix C of Krajnović et al. (2006). Thus, the kinematical misalignment is consistent with zero, consistent with the NC of M33 being axisymmetric.

2.3 Modelling the Observations

It is important to compare the kinematics of the observed NCs to those of the simulations. Given that integral-field kinematics are available for the observed NCs, I use two methods which make full use of the two-dimensional data. One method is based on the Jeans equations and the other is based on the $(V/\sigma, \varepsilon)$ diagram. In the following I show that consistent results are obtained with both approaches.

2.3.1 The Jeans Anisotropic MGE dynamical models

The integral-field stellar kinematics for the NCs in NGC 404 (Seth et al., 2010), NGC 4244 (Seth et al., 2006) and M33 (Seth et al, in prep), the few NCs for which this type of data are available, suggest that NCs are likely not far from oblate axisymmetric systems (as I also argued in Section 2.2). A classic reference model

to quantify the rotation of axisymmetric galaxies is the *isotropic rotator* (Binney, 1978), to which real galaxies have often been compared (e.g. Satoh, 1980; Binney et al., 1990; van der Marel, 1991; van der Marel & van Dokkum, 2007; van der Wel & van der Marel, 2008).

Recent dynamical modelling studies have found that real axisymmetric galaxies are generally best matched by models which have a nearly oblate velocity ellipsoid, flattened along the direction of the symmetry axis $\sigma_z \lesssim \sigma_R \approx \sigma_\phi$ (Cappellari et al., 2007; Cappellari, 2008; Thomas et al., 2009). A useful generalisation of the isotropic rotator to quantify the rotation of these anisotropic systems is a *rotator with an oblate velocity ellipsoid* ($\sigma_z \leq \sigma_R = \sigma_\phi$), which provides a good approximation for the observed integral-field kinematics of real galaxies (Cappellari, 2008; Scott et al., 2009).

To perform the measurement of the degree of rotation I used the Jeans Anisotropic MGE (JAM) software¹ which implements an efficient solution of the Jeans equations with an oblate velocity ellipsoid (Cappellari, 2008). Under that assumption the model gives a unique prediction for the observed first two velocity moments V and $V_{\text{rms}} = \sqrt{V^2 + \sigma^2}$, where V is the observed mean stellar velocity and σ is the mean stellar velocity dispersion.

The luminous matter likely dominates in the high-density nuclei of the studied galaxies. The same is true, by construction, for the simulations. For this reason, the dynamical models assume that light traces mass. To parametrise the surface brightness distribution of either the galaxies or the N -body simulations, I adopted a Multi-Gaussian Expansion (MGE; Emsellem et al., 1994), which I fit to the images with the method and software¹ of Cappellari (2002). For a given inclination, the models have one free nonlinear parameter, anisotropy $\beta_z = 1 - \sigma_z^2/\sigma_R^2$, and two linear scaling factors: (i) the dynamical M/L and (ii) the amount of rotation $\kappa \equiv L_{\text{obs}}/L_{\text{obl}}$, which is the ratio between the observed projected angular momentum L_{obs} and the

¹Available from <http://purl.org/cappellari/idl/>

one for a model with oblate velocity ellipsoid L_{obl} (see Cappellari, 2008, for details). To find the best fitting model parameters I constructed a grid in the non-linear parameter β_z and for each value I linearly scaled the M/L to match the V_{rms} data in a χ^2 sense. At the best-fitting $(\beta_z, M/L)$ I then computed the model velocity V , further assuming $\sigma_R = \sigma_\phi$, and measure the amount of rotation κ from the observed velocity.

2.3.2 JAM models of observed NCs

I applied the procedure to model the Gemini NIFS stellar kinematics of the NC in NGC 4244 (Seth et al., 2008b). The MGE fit to the nuclear part of the ACS/F814W image is shown in Figure 2.3. I used the ACS/F814W image for the MGE fit, because of the better known point spread function compared to the K -band NIFS data. The NC was assumed to be a dynamically distinct component, in equilibrium in the combined potential due to the galaxy and the NC itself. I used all of the MGE Gaussians, of both the NC and the main galaxy disc, in the calculation of the gravitational potential, but only the nuclear Gaussians were used to parametrise the surface brightness of the NC. Therefore, the JAM models of NCs are not self-consistent. Although this assumption is physically motivated and can sometimes produce significant differences in the kinematics of the model, in this case the results are indistinguishable from a self-consistent model. The best-fitting JAM model for NGC 4244, which has an edge-on inclination ($i = 90^\circ$), is shown in Figure 2.4. It has a best-fitting anisotropy parameter $\beta_z = -0.2 \pm 0.1$ and a rotation parameter $\kappa = 0.99 \pm 0.05$. This implies that the NC rotates almost perfectly as the reference rotator with oblate velocity ellipsoid (for which $\kappa = 1$). The best-fitting JAM model has no central IMBH. However from the NIFS data the upper limit of a possibly IMBH is $M_\bullet \lesssim 1 \times 10^5 M_\odot$ inside the NC. This is $\lesssim 1\%$ of the mass of the cluster, $M_{\text{NC}} = (1.1 \pm 0.2) \times 10^7 M_\odot$. For larger M_\bullet the model shows a clear central peak in

V_{rms} which is strongly excluded by the data.

The NC of NGC 4244 is composed of a NCD and a NCS (Seth et al., 2006), which have distinct stellar populations (Seth et al., 2008b). While Seth et al. (2008b) argued that both the disc and spheroid are rotating due to the change of line strengths and optical colour, the models suggest that the rotation signal may come only from the disc. For this I fitted two MGE models separately for the spheroidal and disc component defined by Seth et al. (2006). I computed the best-fitting JAM model for the V_{rms} like before, but then I fit V by setting the rotation to zero ($\kappa = 0$) for the MGE Gaussians describing the NCS. This model with an unrotating NCS reproduces the NIFS data as well as the model with constant anisotropy and rotation for both the NCS and the NCD. This is because the flat disc component of the NC dominates the light and the rotation of the model in the region where NIFS data are available. More spatially resolved/extended kinematics would be required to measure the rotation of the spheroidal component of the NC.

I constructed a similar MGE model for the NC of M33 using the WFPC2/F814W photometry. For the JAM model I adopted the inclination of the main galaxy disc ($i \approx 49^\circ$; Corbelli & Schneider 1997). In this case, the observed distribution of stellar σ from the NIFS data is quite irregular and presents significant asymmetries, which cannot be reproduced by an axisymmetric model. The irregularity in the velocity field is possibly due to granularity in the velocity field, with individual bright AGB stars having significant influence on the velocity and dispersion measurements. The velocity field of M33 and other nearby NCs will be discussed in more detail in an upcoming paper (Seth et al. *in prep*). As the anisotropy cannot be reliably inferred from the data, I assumed isotropy and derived the dynamical M/L from a fit to the observed V_{rms} . The rotation parameter derived from the observed V is then $\kappa = 1.02 \pm 0.10$, which, as for NGC 4244, is consistent with the rotation of the reference rotator with oblate velocity ellipsoid. The total mass of the NC is

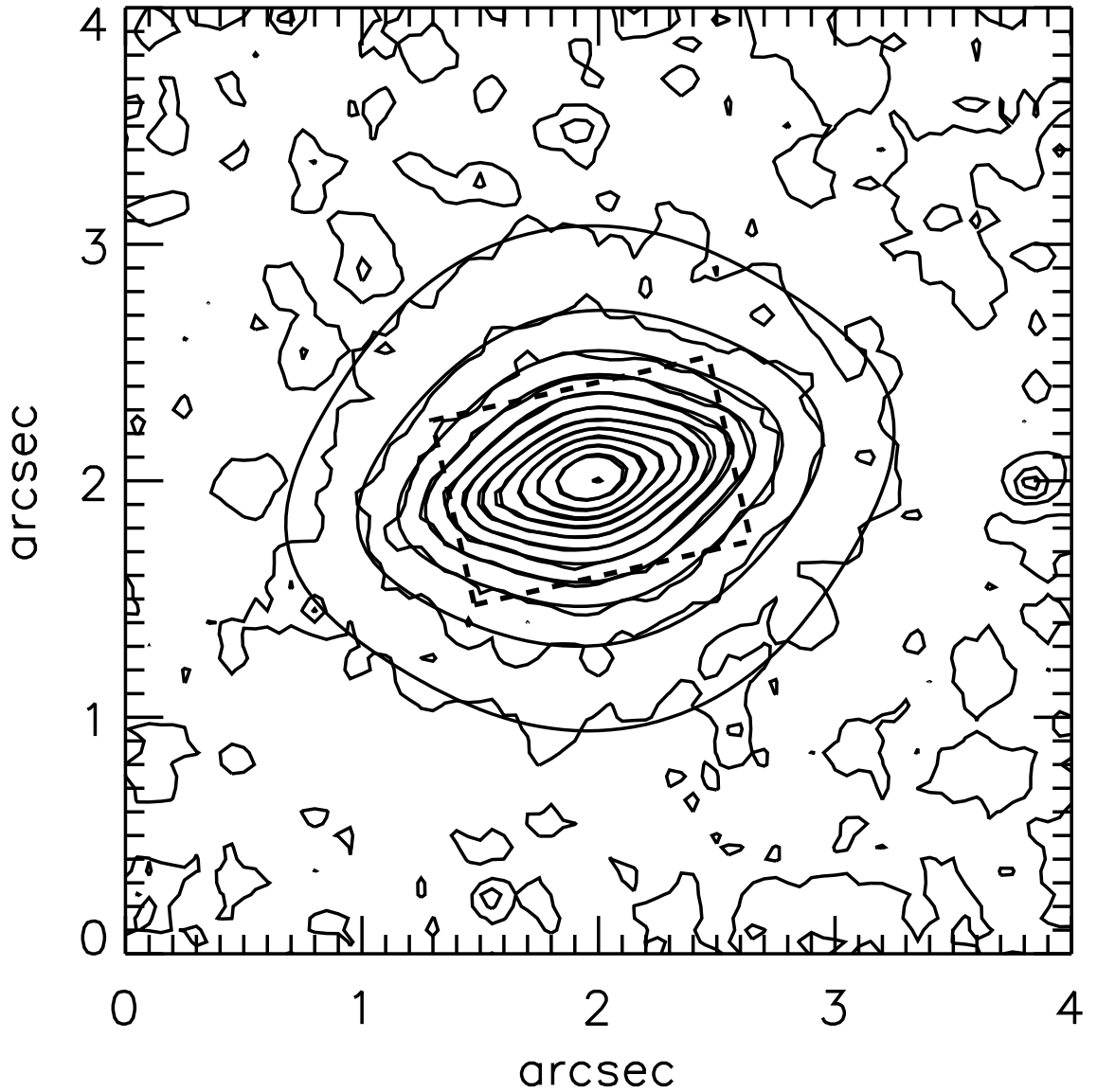


Figure 2.3: The contours of the surface brightness of the ACS/F814W image of the NC in NGC 4244, in steps of 0.5 mag, are overlaid on the PSF-convolved MGE model. Both the NCD and the NCS are well described by the model. The scale is ~ 21.1 pc/arcsec with a half-mass radius $\simeq 0.27''$ (Seth et al., 2008b). The dashed box shows the region within which kinematic data are observed.

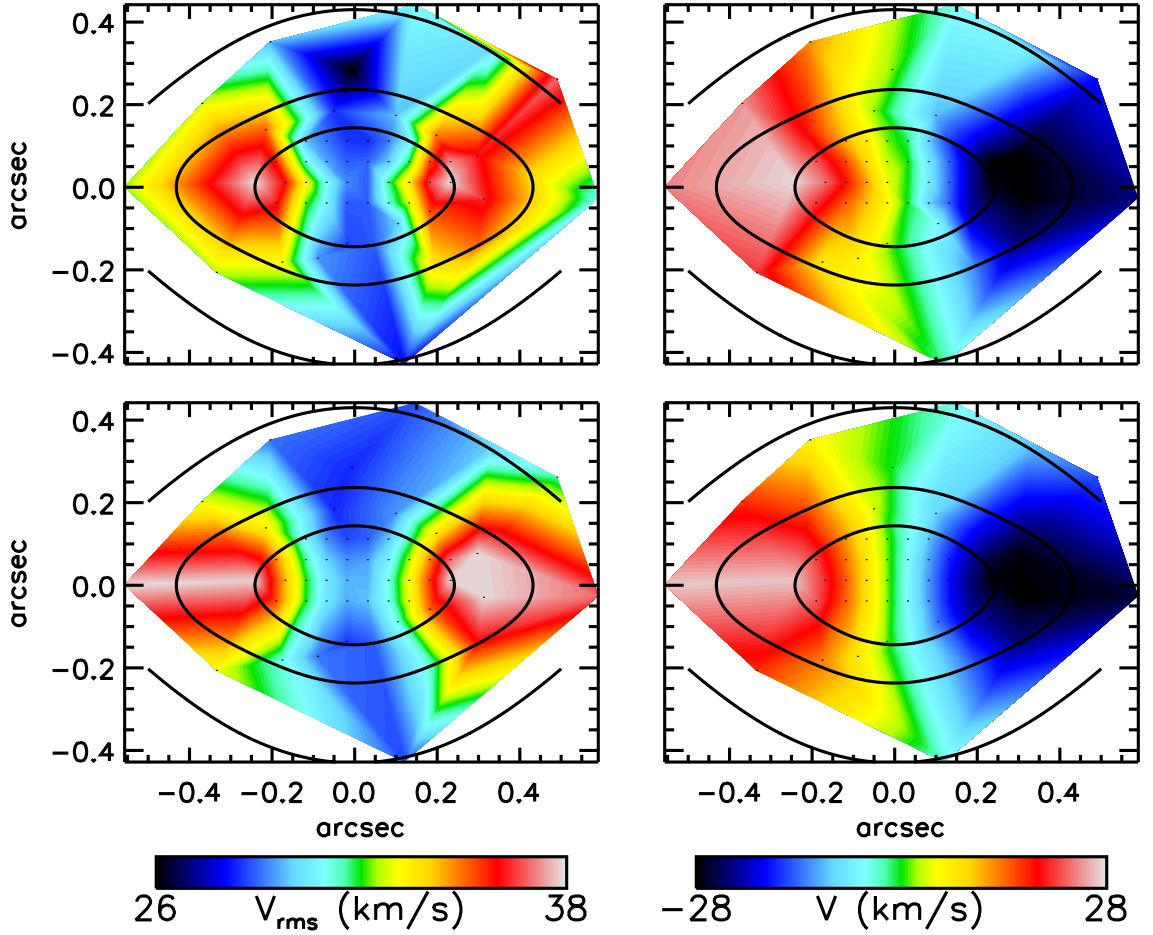


Figure 2.4: JAM model for the stellar kinematics of NGC 4244. The top two panels show the bi-symmetrized NIFS V_{rms} (left) and V (right). The two bottom panels show the corresponding kinematics of the best fitting JAM model. The contours of the surface brightness are overlaid in steps of 0.5 mag. The dots indicate the position of the centroids of the Voronoi bins for which the kinematics were extracted. The best fitting model has $\beta_z = -0.2 \pm 0.1$ and $\kappa = 0.99 \pm 0.05$. The NC of NGC 4244 has an almost perfect oblate velocity ellipsoid.

$$M_{\text{NC}} = (1.4 \pm 0.2) \times 10^6 M_{\odot}.$$

2.3.3 Rotation from the $(V/\sigma, \varepsilon)$ diagram

An alternative classic way of quantifying rotation is given by the $(V/\sigma, \varepsilon)$ diagram (Illingworth, 1977; Binney, 1978). Traditionally, the observed V/σ quantity was computed from the central velocity dispersion and the maximum rotational velocity. Binney (2005) updated and improved the formalism to compute the quantity in a more robust way when integral-field data are available. Here, the availability of integral-field kinematics for both the observations and the simulations allow us to apply this improved method. I use the updated formulae and define

$$\left(\frac{V}{\sigma}\right)_e^2 \equiv \frac{\langle V^2 \rangle}{\langle \sigma^2 \rangle} = \frac{\sum_{n=1}^N F_n V_n^2}{\sum_{n=1}^N F_n \sigma_n^2} \quad (2.3)$$

and I applied it within $3 R_{\text{eff}}$ as a luminosity-weighted quantity, which I estimate from the integral-field kinematics. Here F_n is the flux contained inside the n -th Voronoi bin and V_n and σ_n the corresponding measured mean line-of-sight velocity and velocity dispersion. The ellipticity is defined following Cappellari et al. (2007) by a similar expression as

$$(1 - \varepsilon)^2 = q^2 = \frac{\langle y^2 \rangle}{\langle x^2 \rangle} = \frac{\sum_{n=1}^N F_n y_n^2}{\sum_{n=1}^N F_n x_n^2}, \quad (2.4)$$

where the (x, y) coordinates are centred on the galaxy nucleus and the x axis is aligned with the NC photometric major axis. I estimate ε from the individual pixels, inside a given galaxy isophote, within the same region used for the computation of $(V/\sigma)_e$. The main disadvantage of the $(V/\sigma, \varepsilon)$ diagram, with respect to the JAM models, is that it does not rigorously take into account of multiple photometric systems, like a disc and a spheroid. Moreover, while the diagram can quantify the anisotropy, it does not provide any information on whether it is mostly radial or tangential. Still the diagram provides an important independent test of more detailed models and provides an easy way of comparing simulations and observations.

I used Eqns. 2.3 and 2.4 to place the NC of M33 and NGC 4244 on the $(V/\sigma, \varepsilon)$ diagram, using the NIFS data in Figure 2.5, where the line-of-sight velocities are obtained from a fit of a Gauss-Hermite series. Given that the diagram is defined for edge-on orientations, while M33 has an inclination of $i \approx 49^\circ$, I projected the $(V/\sigma, \varepsilon)$ values for the NC to an edge-on view following Binney & Tremaine (2008). The NC in NGC 4244 is seen at a nearly edge-on orientation and is weakly anisotropic. The location of M33 is slightly more uncertain, given the non edge-on view, but the NC is consistent with isotropy.

2.4 Conclusion

I have used HST data and NIFS integral field data about the NCs in NGC 4244 (Seth et al., 2006, 2008b) and M33 (Seth et al. in prep.). I find no evidence of non-axisymmetry in the NC of M33. Its PA is consistent with that of its main disc and its apparent ellipticity is consistent with a vertical flattening of $q = 0.7$, which is the average observed in the NCs of edge-on late-type galaxies (Seth et al., 2006). There is also only a small misalignment between the photometric and kinematic PAs. While this is the only galaxy where this measurement can be done at present, it suggests that NCs are generally axisymmetric.

I used the Jeans Anisotropic MGE (JAM) software, which implements an efficient solution of the Jeans equations with an oblate velocity ellipsoid (Cappellari, 2008), to obtain a model of the NCs in M33 and in NGC 4244. The isotropic model velocity ellipsoid of M33 has a mass of $(1.4 \pm 0.2) \times 10^6 M_\odot$ and is rapidly rotating. In the case of NGC 4244 I find that the NC is nearly isotropic, with a vertical anisotropy $\beta_z = -0.2 \pm 0.1$, and that the NC is rapidly rotating. It has a mass of $(1.1 \pm 0.2) \times 10^7 M_\odot$; if an IMBH is present its mass is less than 1% that of the NC. It is not possible from these models to distinguish whether the rotation is present throughout the NC or is restricted to the NCD.

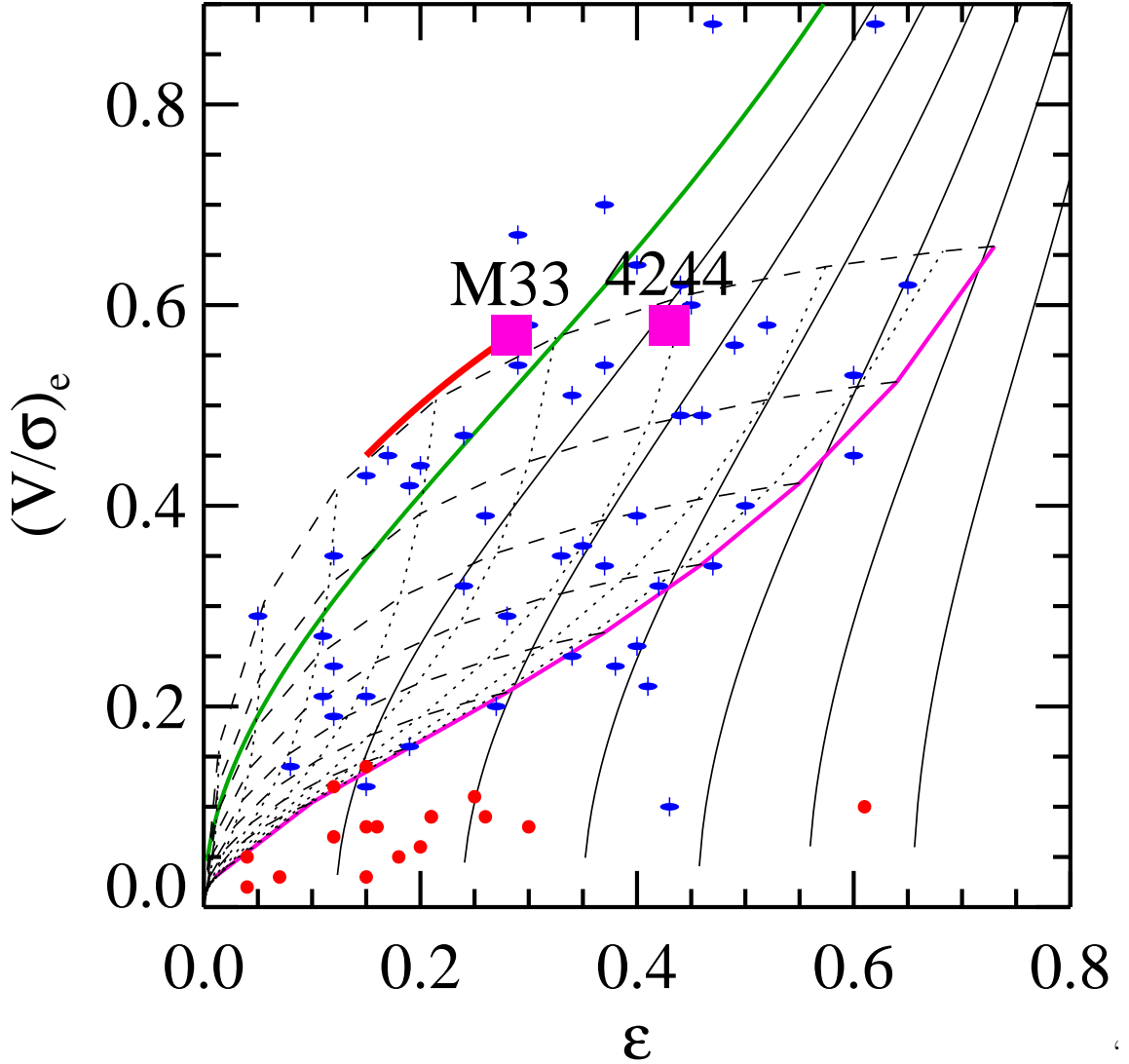


Figure 2.5: Observed NCs on the $(V/\sigma, \varepsilon)$ diagram of Binney (2005). The thick green line indicates the location of edge-on isotropic models, while the other solid lines are anisotropic models with global anisotropy $\delta \equiv 1 - 2\sigma_z^2 / (\sigma_\phi^2 + \sigma_R^2)$, spaced at 0.1 intervals. The magenta line is the lower envelope for fast-rotating galaxies defined in Cappellari et al. (2007). The dashed lines indicate how the magenta line transforms at lower inclinations in 10° steps, indicated by the dotted lines. The magenta squares are the observed NCs in NGC 4244 and M33. The observed location for M33 has been projected (red line) assuming an inclination of $i = 49^\circ$. For comparison I also plot the fast-rotator (blue dots) and slow-rotator (red circles) early-type galaxies from Cappellari et al. (2007). The observed NCs are fast rotating and relatively close to the line of isotropy.

Chapter 3

Constraining the role of star cluster mergers in nuclear cluster formation

The half mass relaxation time for the NC in NGC 4244, with $R_{\text{eff}} \simeq 5$ pc and total mass $1.1 \times 10^7 M_{\odot}$ is ~ 10 Gyrs. NCs in the Virgo Cluster Survey have relaxation times ranging from 1 – 10 Gyrs (Merritt, 2009). Therefore it is reasonable to approximate NCs as collisionless systems on timescales of $\lesssim 1$ Gyr, allowing me to use standard collisionless codes to simulate their evolution.

3.1 Numerical Methods

In this Section I describe the N -body initial conditions for the simulations. I am interested in the evolution at the inner ~ 100 pc region of such galaxies. Assuming an NFW halo (Navarro et al., 1996) with a concentration parameter $c \sim 10$ and total mass of the halo $M_h \sim 10^{12} M_{\odot}$, the dark matter mass fraction within this radius is only 20% if the main disc is exponential with a scale-length $R_d \sim 2$ kpc and a mass $M_d \sim 4 \times 10^{10} M_{\odot}$. If instead a bulge of mass $M_b \sim 1 \times 10^{10} M_{\odot}$, Sersic

Index $n \sim 2$ and half mass radius $R_{\text{eff}} \sim 0.6$ pc is present, then the dark matter mass fraction is even lower, 1%. Therefore, the contribution to the mass within the central region from the halo is negligible and I ignore it throughout the simulations, I used in this chapter.

3.1.1 Galactic disc model

NGC 4244 and M33 are late-type, bulgeless galaxies, therefore I consider only the main galactic disc and adopt an exponential profile:

$$\rho(R, z) = \frac{M_d}{2\pi R_d^2} e^{-R/R_d} \frac{1}{\sqrt{2\pi} z_d} e^{-z^2/2z_d^2} \quad (3.1)$$

where M_d is the disc mass, R_d is the scale-length of the disc and z_d the scale-height. I use $M_d = 10^{10} M_\odot$, $R_d = 2.0$ kpc, $z_d = 200$ pc and truncate the disc at $5 R_d$. The disc is represented by 4×10^6 particles. If I had used equal mass particles for the galactic disc, this would correspond to particle masses of $2500 M_\odot$. Such high masses would inhibit dynamical friction on objects of mass $\sim 10^4 M_\odot$, and lead to excessive heating of any in-falling clusters. In order to reduce such effects, I use multi-mass disc particles, with masses ranging from $7 M_\odot$ within the inner 20 pc increasing to $1.2 \times 10^7 M_\odot$ in the disc's outskirts. Figure 3.1 shows the distributions of masses and softenings of disc particles; the latter is related to particle mass via $\epsilon_p \propto m_p^{1/3}$. I use the epicyclic approximation to set Toomre- $Q = 1.2$. This setup is imperfect and needs to be relaxed. Simulations using such initial conditions can only be run for a few crossing times of the main disc, since the radial migration of stars induced by disc instabilities, including bars and spirals, would introduce massive particles to the central regions (Sellwood & Binney, 2002; Debattista et al., 2006b; Roškar et al., 2008). In order to check that the system does not rapidly homogenise, I relaxed the system for 10 Myrs, after which main disc particles in the central 100 pc have masses ranging from $7 M_\odot$ to $2.8 \times 10^3 M_\odot$. In Figure 3.2, I plot the mass distribution for the disc particles within the inner 100 pc at three different times for

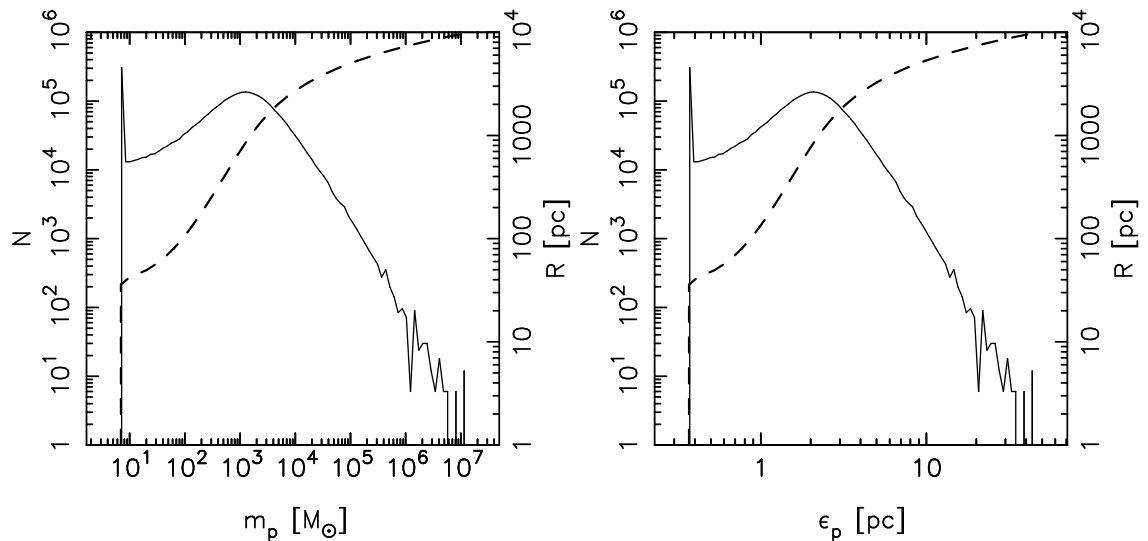


Figure 3.1: The unrelaxed initial conditions of the main galactic disc. Left: The solid line shows the number of particles (left axis) and the dashed line the radius R (right axis) versus the particle mass. Right: The solid line represents the number of particles with a certain softening ϵ and the dashed line the softening of the particles versus the radius.

the longest merger simulation (M2, described below). The cumulative distribution (bottom panel) shows that the mass at the centre is dominated by particles with masses smaller than $2500 M_\odot$, with more than half the mass in this region coming from particles with masses less than $1000 M_\odot$. Thus, these simulations using the main disc as initial conditions are only suitable for simulations about ~ 1 Gyr. After ~ 1 Gyr it becomes more likely that more massive particles are getting close to the centre due to disc instabilities. This would lead to scattering of particles and excessive heating of less massive particles and finally destroy the equilibrium. For longer times (> 1 Gyr) only initial conditions with isotropic velocity distribution are possible such as a bulge.

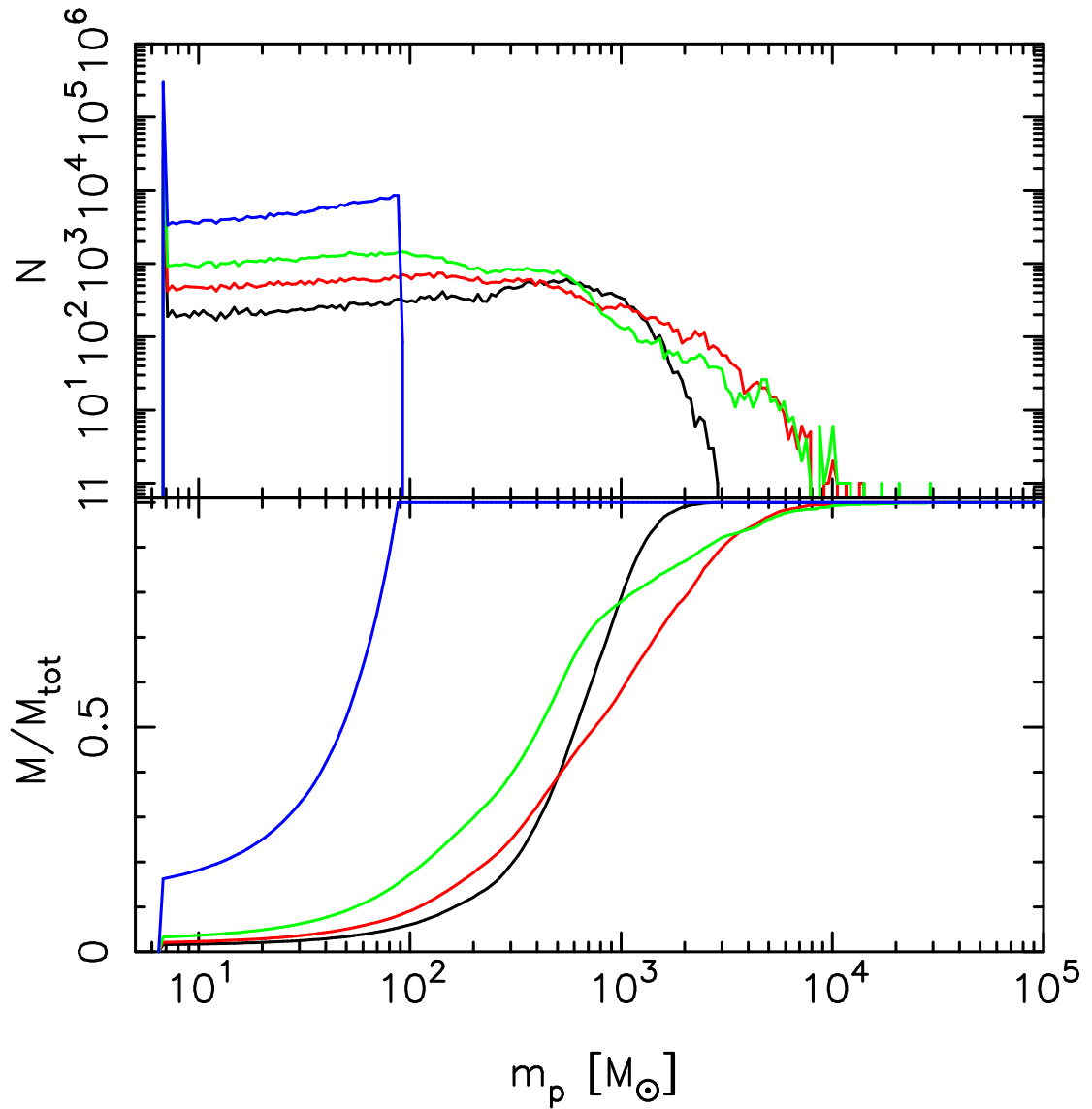


Figure 3.2: The masses of particles in the inner 100 pc of the main disc in run M2. Blue: initial setup; black: initial conditions after relaxing the disc for 10 Myr; red: after 17.5 Myr; green: after 35 Myr. The top panel shows the number of particles of a given mass while the bottom panel shows the cumulative mass distribution.

3.1.2 Bulge model

On timescales comparable to the crossing time of the galaxy, dynamical instabilities, such as bars and spirals, move particles to the central regions. Multi-mass particle simulations within discs are no longer possible in these cases. I set up a bulge, again neglecting the dark matter halo, and evolve the systems in this environment. The bulge model has a Hernquist (1990) profile:

$$\rho(r) = \frac{aM_b}{2\pi r(r+a)^3}, \quad (3.2)$$

where M_b is the bulge mass and a is the scale radius. I use $M_b = 5 \times 10^9 M_\odot$ and $a = 1.7$ kpc. The bulge is truncated by eliminating all particles with enough energy to reach $r > 15a$, therefore the density drops gently to zero at this radius (Sellwood & Debattista, 2009). The bulge is populated by 3.5×10^6 particles with masses ranging from $40 M_\odot$ to $3.9 \times 10^5 M_\odot$. Particle masses are selected by the weighting function $w(L) \propto 3 + 5000L^2$, with L the specific angular momentum, ensuring a high resolution within the inner 160 pc (Sellwood, 2008). The softening is related to the particle mass via $\epsilon_p \propto m_p^{1/3}$. Unlike the disc, the bulge has no strong instabilities, therefore the distribution of particles remains unchanged even on timescales of a few Gyrs. These timescales are needed to model multiple accretions of SCs. Figure 3.3 shows the particles distribution for simulation A1, described below, within 32 pc for three different times. This simulation shows the largest changes in the mass distribution. Although accretion delivers higher mass particles into the central region, the distribution of particles does not substantially change.

3.1.3 Star cluster models

I set up model SCs, ranging in mass from $2 \times 10^5 M_\odot$ to $2 \times 10^6 M_\odot$, using an isotropic distribution function (DF): $f(x, v) = \mathcal{F}(E)$. The specific form I choose is

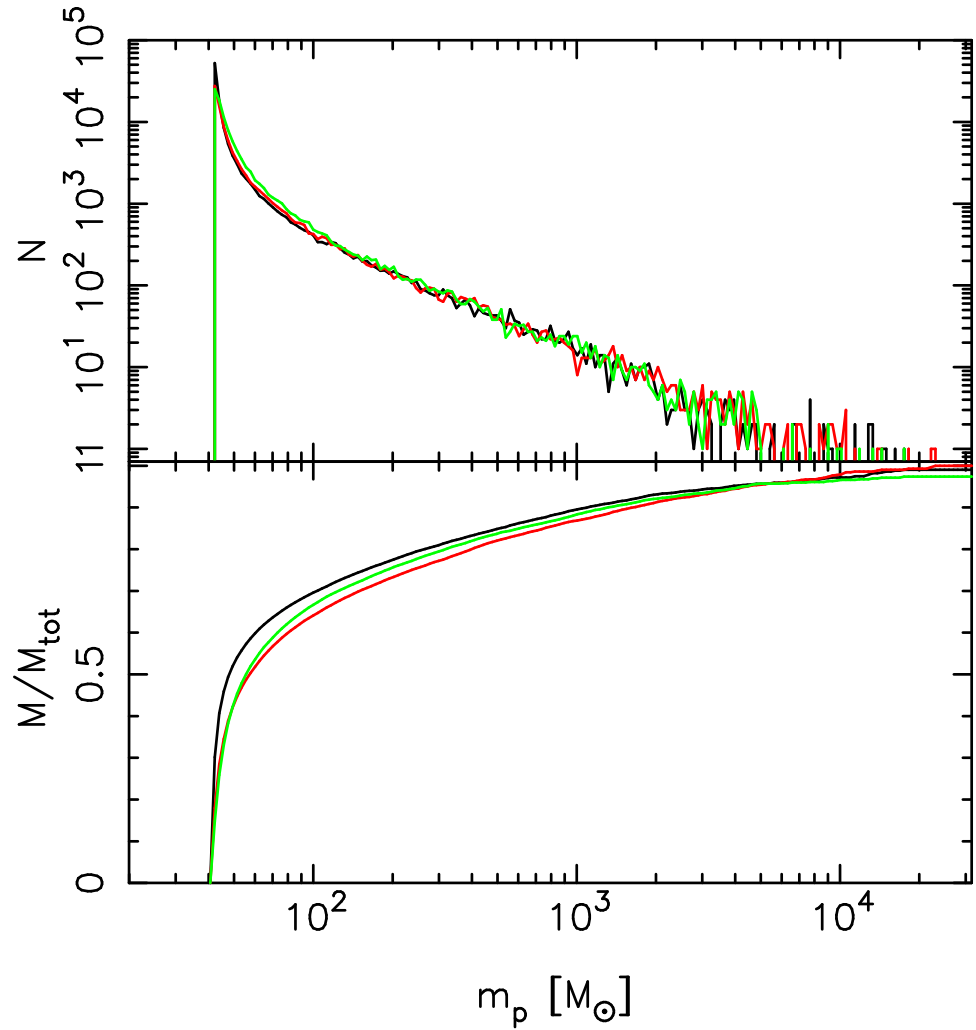


Figure 3.3: The masses of particles in the inner 30 pc of the bulge in simulation A1. Black: initial setup; red: initial conditions after the 65 Myr needed for the infall of the NCS seed; green: after 0.275 Gyrs. The top panel shows the number of particles of a given mass while the bottom panel shows the cumulative mass distribution.

a lowered polytrope DF

$$f(x, v) \propto [-2E(x, v)]^{n-3/2} - [-2E_{max}]^{n-3/2}, \quad (3.3)$$

with polytrope index $n = 2$ in all cases. I produce equilibrium models through the iterative procedure described in Debattista & Sellwood (2000). I set up five such models, C1-C5. All SC models have particles of equal mass ($1.1 M_{\odot}$ for C1-C2, $5.0 M_{\odot}$ for C3-C4 and $15 M_{\odot}$ for C5) and equal softening ($\varepsilon = 0.104$ pc for C1 and C2 and $\varepsilon = 0.13$ pc for C3-C5). IMBHs may be present in some SCs (Gebhardt et al. 2000b, 2005; Gerssen et al. 2002, 2003; Noyola et al. 2008, 2010, but see also van der Marel & Anderson 2010). In model C2 I include an IMBH at the centre of the cluster C1 by adiabatically growing the mass of a single particle with softening $\varepsilon_p = 0.042$ pc over 100 Myrs. Table 3.1 lists the properties of the SC models. The concentration c is defined as $c \equiv \log(R_{\text{eff}}/R_c)$ where R_{eff} is the half mass radius (effective radius) and R_c is the core radius, where the surface density drops to half of the central. Figure 3.4 plots the volume density profiles of the SCs. The central density ρ_0 ranges from 3×10^3 to $1 \times 10^5 M_{\odot} \text{ pc}^{-3}$; the masses and R_{eff} (see Tab. 3.1) are comparable to young massive star clusters in the Milky Way (Figer et al., 1999, 2002), in the LMC (Mackey & Gilmore, 2003), in the Fornax Cluster (McLaughlin & van der Marel, 2005), in irregular galaxies (Larsen et al., 2004) and in interacting galaxies (Bastian et al., 2006).

3.1.4 Bare NCD model

If direct formation of a NCD via gas inflows precedes the full formation of a NC, how does the accretion of SCs alter the properties of such NCD? The simulations do not include smooth particle hydrodynamics (SPH) only pure N -body systems. For this reason I cannot introduce any gas particles in my simulations to study the dynamics of such particles and the dissipative formation of a NCD. In order to mimic the dissipative formation of such a NCD, I introduce a stellar NCD component at the

Table 3.1: The SCs used in the simulations. M_* is the stellar mass of the SC, R_{eff} is the effective (half-mass) radius, c is the concentration (see text for definition) and M_\bullet is the mass of the black hole if one is present.

Model	M_*	R_{eff}	c	M_\bullet
	$[M_\odot]$	$[\text{pc}]$		$[M_\odot]$
C1	2.2×10^6	1.72	0.07	-
C2	2.2×10^6	1.60	0.07	4.4×10^4
C3	2.0×10^6	2.18	0.12	-
C4	2.0×10^5	1.11	0.12	-
C5	6.0×10^5	1.11	0.16	-

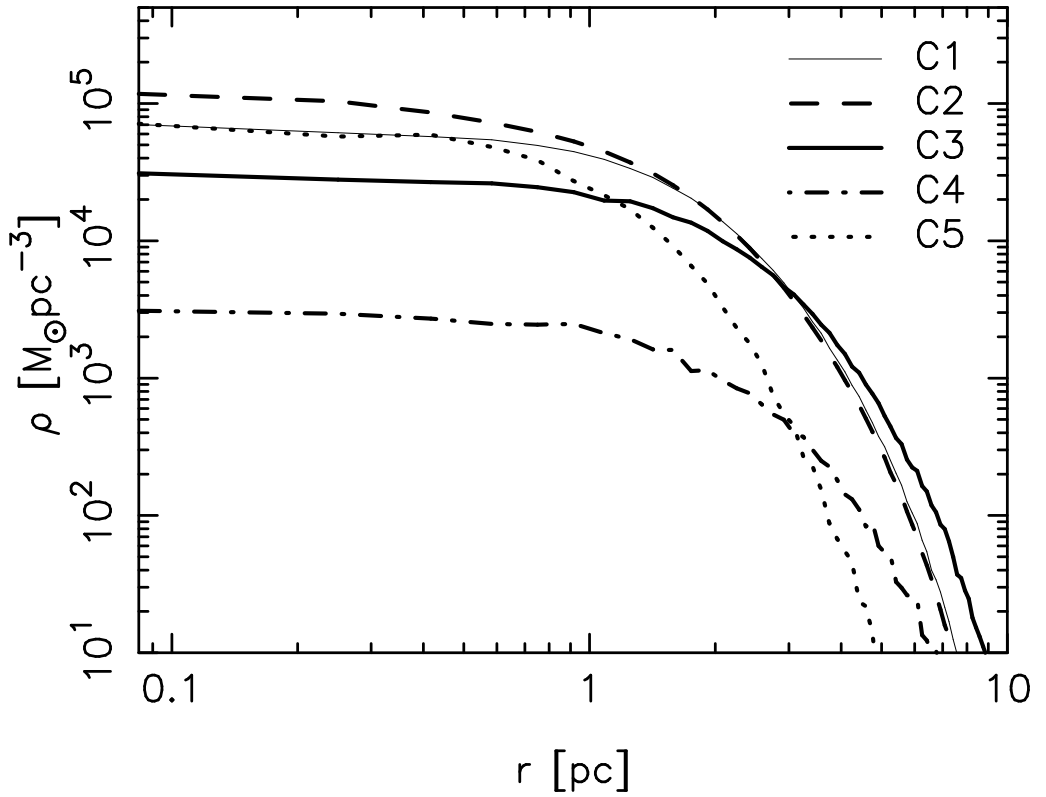


Figure 3.4: Volume density of the SC models C1 - C5 used in the merger and accretion simulations.

centre of the bulge. I generated this NCD model by adiabatically growing a stellar disc over a period of 0.5 Gyr. The NCD is exponential of the type in Eqn. 3.1, with a scale-length $R_d = 9.5$ pc and scale-height $z_d = 0.1R_d$. The disc, truncated at a radius of $5 R_d$, consists of 2×10^5 particles each with softening $\varepsilon = 0.13$ pc. The final total mass of the NCD is $1 \times 10^6 M_\odot$. I set the kinematics of the grown disc to give constant z_d and Toomre- $Q = 1.2$, as described in Debattista & Sellwood (2000). For this, I calculated the potential using a hybrid polar-grid code (Sellwood, 2003).

3.1.5 Numerical parameters

All the simulations in this chapter were evolved with PKDGRAV (Stadel, 2001), an efficient, parallel tree-code. I used an opening angle $\theta = 0.7$ in all of the simulations. PKDGRAV is a multi-stepping code, with timesteps refined such that $\delta t = \Delta t / 2^n < \eta(\varepsilon/a)^{1/2}$, where ε is the softening and a is the acceleration at a particle's current position. I set $\eta = 0.1$ in all cases. Simulations A1-A3 used base timestep $\Delta t = 10^5$ years, whereas all other simulations used half this value $\Delta t = 0.5 \times 10^5$ years.

3.2 Results of the Merger Simulations

I ran three simulations in which eight massive SCs were allowed to merge at the centre of the disc to form a NC. I use SC models C1 and C2 in these simulations, because these SCs are sufficiently massive and concentrated to not evaporate too rapidly (McLaughlin & Fall, 2008) and to have orbit decay times due to dynamical friction less than 3 Gyr from a radius of 1 kpc (Milosavljević, 2004). Lower mass SCs having longer infall times and thus are not able to merge within a Hubble time within the central region of galaxies. These simulations are used to test, whether the proposed formation scenario of the merger of SCs or globular clusters is able to reproduce the structural and kinematical properties of observed NCs, see Chapter 2.

Table 3.2: The merger simulations. N(SC) gives the number of star clusters used and column SC lists which star cluster from those in Table 3.1 are used in the simulation. Column host shows which host galaxy model is used as initial conditions.

Run	N(SC)	SC	host	Comments
M1	8	C1	disc	SCs at mid-plane of main disc
M2	8	C1	disc	6 SCs offset from main disc mid-plane
M3	8	C2	disc	SCs at mid-plane of main disc
A1	10	C5	bulge	multiple accretion of SCs onto NCS
A2	20	C4	bulge	accretion of SCs onto a NCD
A3	20	C4	bulge	like A2 with 50% retrograde orbits

The SCs were placed randomly at radii ranging from 14 to 92 pc with velocities between 8 and 13 km s^{-1} , which are $\sim 60\%$ of the local circular velocity. In run M1 the SCs are all initially in the mid-plane; in run M2 instead the SCs are vertically offset from the mid-plane by up to 67 pc, with tangential velocities similar to M1 and vertical velocities up to 1 km s^{-1} . Finally, run M3 is identical to run M1, but uses SC C2 instead of C1. Details of these simulations are listed in Table 3.2.

SCs merge after 13–36 Myr, with the longest time needed in M2. One SC failed to merge in run M1 and was excluded from all analysis. In M3 two of the eight IMBHs came very close with a distance similar to the softening length ϵ . Therefore I decided to merge both IMBHs by adding a particle containing a mass of both IMBHs at their centre of mass and with the velocity of their centre of velocity. This was necessary, because the runtime of the simulation was slow, because the simulation has to resolve the movements of these two close particles.

3.2.1 Structural properties

I measured mass surface density profiles of the remnant NCs viewed face-on and obtained R_{eff} by fitting Sérsic or King profiles. The King profile clearly fits the profiles better and I therefore present results only of this fit throughout. The King profile is given by (King, 1962)

$$\Sigma(R) = k [X^{-1/2} - C^{-1/2}]^2 \quad (3.4)$$

with normalisation constant $k = \Sigma_0 [1 - C^{-1/2}]^{-2}$, $X(R, R_c) = 1 + (R/R_c)^2$ and $C(R_t, R_c) = 1 + (R_t/R_c)^2$, where R_c is the core radius and R_t is the tidal radius at which the projected density drops to zero. Integration yields the cumulative form of the King profile for $R \leq R_t$:

$$M(R) = \pi R_c^2 k \left[\ln X - 4 \frac{X^{1/2} - 1}{C^{1/2}} + \frac{X - 1}{C} \right] \quad (3.5)$$

which is the mass in projection within a cylinder of radius R . R_{eff} can be approximated by

$$R_{\text{eff}} = R_c \left[e^{(M/2\pi R_c^2 k) - 1} \right]^{1/2}. \quad (3.6)$$

The merger remnants have R_{eff} in the range 4.3 – 4.7 pc with mass fractions from 87 – 97% of the total *merged* SC mass. These masses are consistent with those of observed NCs (Côté et al., 2006; Geha et al., 2002; Böker et al., 2004; Walcher et al., 2006; Seth et al., 2006). Figure 3.5 plots the mean surface density within R_{eff} versus the total mass of the merger remnants and compares them to NCs in early-type galaxies (Côté et al., 2006), late-type spiral galaxies (Carollo et al., 1997, 1998, 2002; Böker et al., 2002; Seth et al., 2006) and Milky Way GCs (Walcher et al., 2005). As shown by Capuzzo-Dolcetta & Miocchi (2008b), I find that SC mergers produce remnants which have structural properties in good agreement with observed NCs.

As was shown already by Bekki et al. (2004), the merger remnants can be triaxial. I measured the ellipticities viewed face-on and edge-on of the simulated NCs using

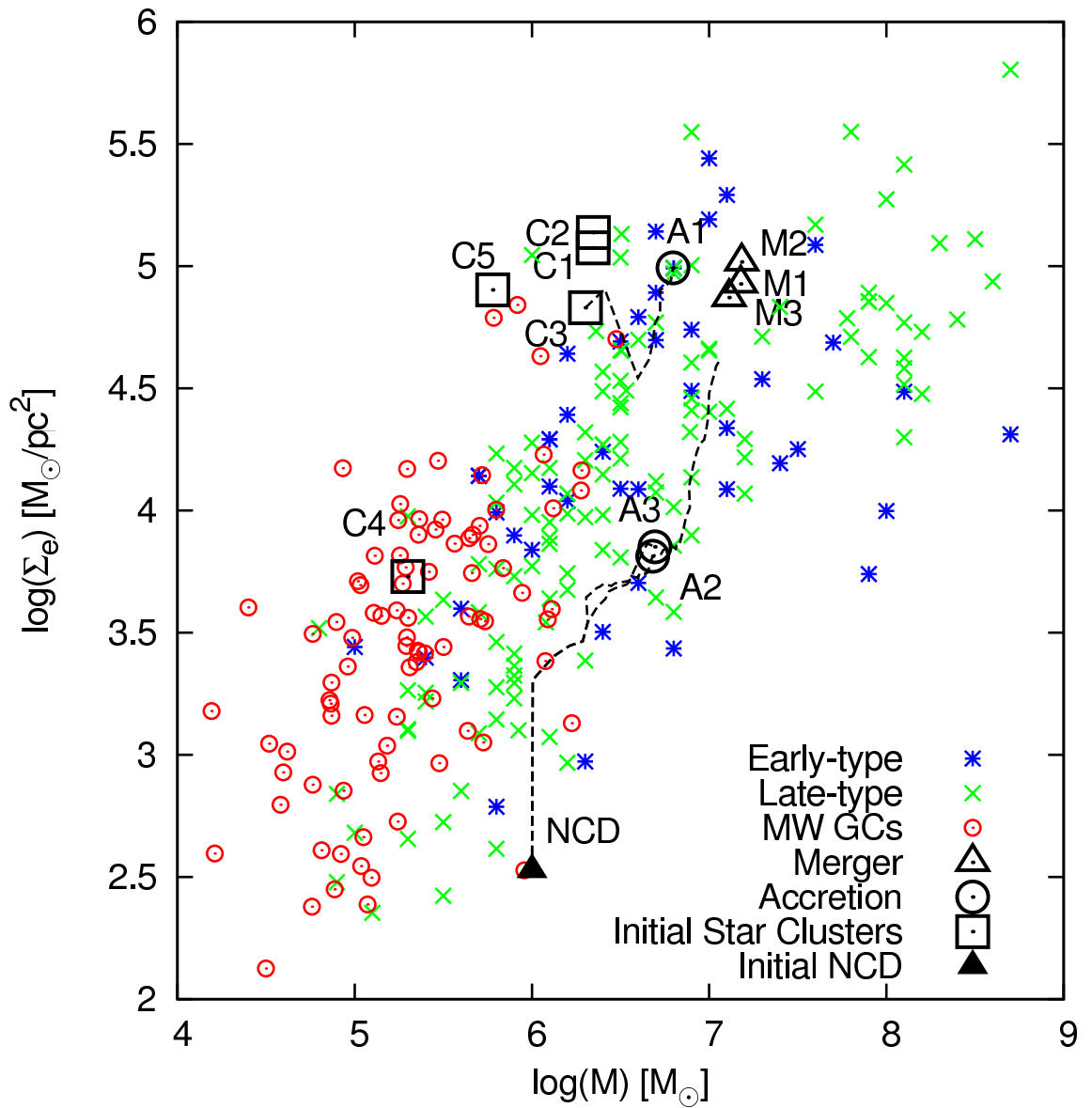


Figure 3.5: Comparison of the simulated and observed NCs in the mean surface density within R_{eff} versus total NC mass plane. I compare with the observed NCs of early-type and late-type spiral galaxies as well as Milky Way globular clusters. The initial SCs are shown by the open black squares while the remnant NCs are shown by black triangles for multiple mergers and black circles for multiple accretions. The tracks of the evolving NC in the multiple accretion simulations are indicated by dashed lines.

Eqn. 2.4, obtaining the isophote at R_{eff} using the task ELLIPSE in IRAF. The NC in M1 is significantly non-axisymmetric, with face-on mean ellipticity $\varepsilon_{FO} \simeq 0.37$. I also measured the 3-D shape using the moment-of-inertia tensor as described in Debattista et al. (2008). Figure 3.6 plots the density axis ratios and triaxiality, $T = (a^2 - b^2)/(a^2 - c^2)$ (Franx et al., 1991), of the remnant NCs. In run M1, the NC is triaxial within $2 R_{\text{eff}}$. Models M2 and M3 explore two ways of producing more axisymmetric NCs. In M2 I start the SCs off the mid-plane. This makes the NC oblate, with $\varepsilon_{FO} \simeq 0.05$. In run M3 instead I add 2% IMBHs to the SCs which again results in an oblate NC, also with $\varepsilon_{FO} \simeq 0.03$.

I find remnant edge-on ellipticities at $3 R_{\text{eff}}$ ε_{EO} in the range of $0.36 - 0.56$. These values are consistent with the range of observed ellipticities $0.39 - 0.89$ (Seth et al., 2006).

Figure 3.7 shows B_4 for the edge-on view. In the triaxial NC of M1, B_4 varies with viewing angle but is always negative, *i.e.* the NC is boxy. The NCs in M2 and M3 are also boxy. The merger of SCs cannot produce isophotes as discy as observed in the NC of NGC 4244.

3.2.2 Remnant kinematics

Bekki et al. (2004) found that his merger remnants were rotating, while Capuzzo-Dolcetta & Miocchi (2008a) found that merger remnants are kinematically distinct from the main disc/bulge.

Figure 3.8 shows the edge-on line-of-sight kinematics of the remnant NCs. They are all clearly strongly rotating. However, the second moment of the velocity, V_{rms} , shows that the merger remnants are so dominated by dispersion at the centre that V_{rms} is centrally peaked, contrary to what is seen in the NC of NGC 4244 (Figure 2.4). In the bottom row I show the rotation curve $V_c(R)$, the line-of-sight velocity $V(x)$, the line-of-sight velocity dispersion $\sigma(x)$ and the root-mean-square

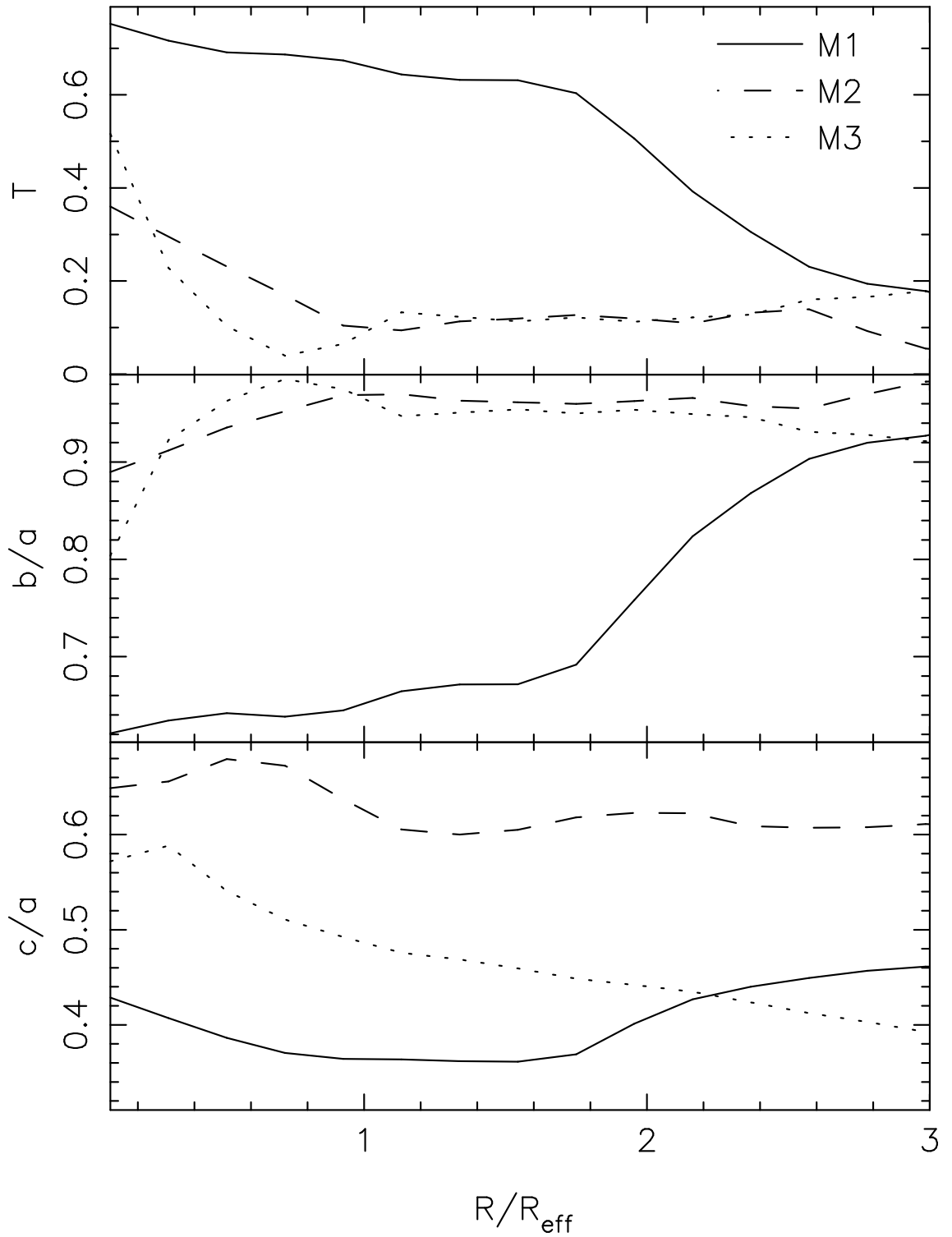


Figure 3.6: The 3-D shape of the NC in runs M1 (solid lines), M2 (dashed lines) and M3 (dotted lines). The top panel shows the triaxiality T , the second row b/a and the third c/a .

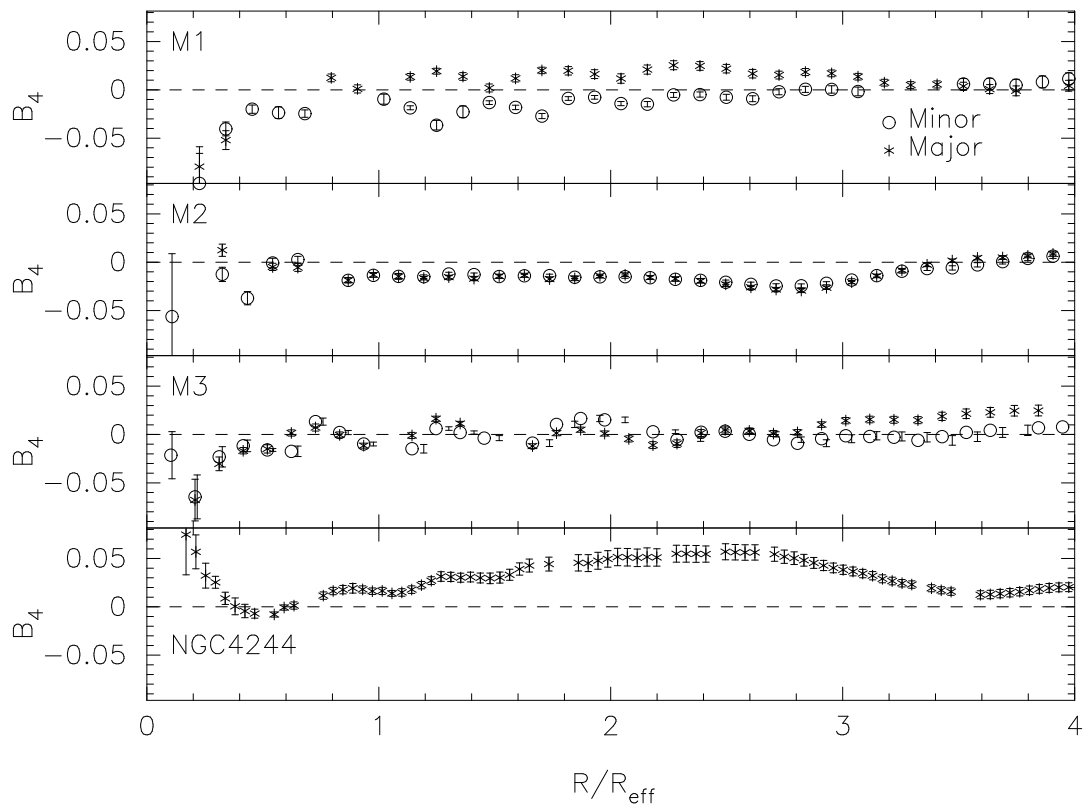


Figure 3.7: The B_4 parameter for the merger simulations. From top to bottom these are M1, M2, M3 and the NC of NGC 4244 for comparison. The remnant NCs have $B_4 \lesssim 0$, whereas the observed NC in NGC 4244 has clearly discy isophotes, i.e. positive B_4 .

velocity $V_{\text{rms}}(\mathbf{x})$ of the merger remnants. Velocities in M1-M3 peak at larger radii than those observed in NGC 4244 and M33 (see Figure 2.1).

In Figure 3.9 the anisotropies in cylindrical coordinates are shown,

$$\beta_\phi = 1 - \left(\frac{\sigma_\phi}{\sigma_R} \right)^2 \quad (3.7)$$

and

$$\beta_z = 1 - \left(\frac{\sigma_z}{\sigma_R} \right)^2, \quad (3.8)$$

where σ_R , σ_ϕ and σ_z are the radial, tangential and vertical velocity dispersions, respectively. This shows that the remnant NCs are all radially biased within $4 R_{\text{eff}}$. M2 is less radially biased than M3, which may seem surprising at first, but the radius of the sphere of influence of the IMBH in M3 is less than 1 pc, explaining the absence of a tangential bias at R_{eff} . The vertical pressure support is generally the smallest. The initial vertical energy of the SCs in run M2 imparts larger vertical random motions, leading to the smallest β_z and smallest edge-on ellipticity ε_{EO} . Radial anisotropy has been noted in the past as a signature of the merging process (e.g. Burkert & Naab, 2005; Bournaud et al., 2007; Debattista et al., 2008; Thomas et al., 2009). The presence of plausible IMBHs does not alter this result.

3.2.3 Accretion onto Super Star Clusters

The super star cluster found by Kornei & McCrady (2009) in the nuclear region of NGC 253 seems destined to fall into the centre of the galaxy and form the basis of a NC. How would the accretion of further SCs alter the structure and kinematics of such a seed NC? Observed Milky Way globular clusters are found to be nearly isotropic (Gebhardt, 1994; Gebhardt et al., 1995). How much mass needs to be accreted to appreciably alter the isotropic distribution? As we have seen before, the

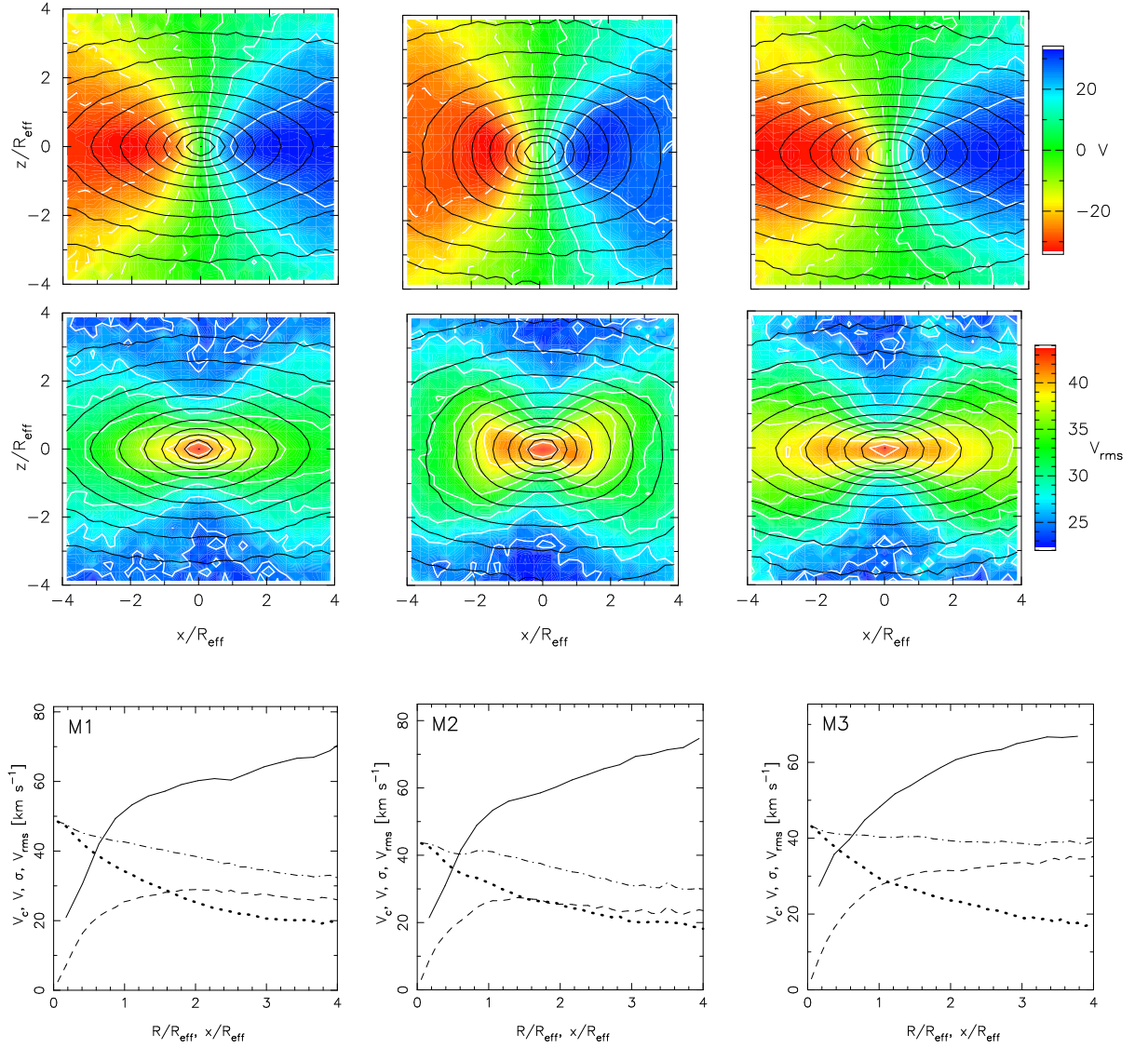


Figure 3.8: Velocity (top row) and V_{rms} (middle row) fields within $4 R_{\text{eff}}$ for M1 (left), M2 (middle), and M3 (right). The velocity fields show a large scale rotation. In all cases, V_{rms} is centrally peaked. In the top two rows black contours show log-spaced density while the white contours show the kinematic contours corresponding to each panel. The bottom row plots the rotation curve $V_c(R)$ (solid lines), the line-of-sight velocities $V(x)$ (dashed lines), the line-of-sight velocity dispersions $\sigma(x)$ (dotted lines) and the root-mean-square velocities $V_{\text{rms}}(x)$ (dashed-dotted lines) along the major axis.

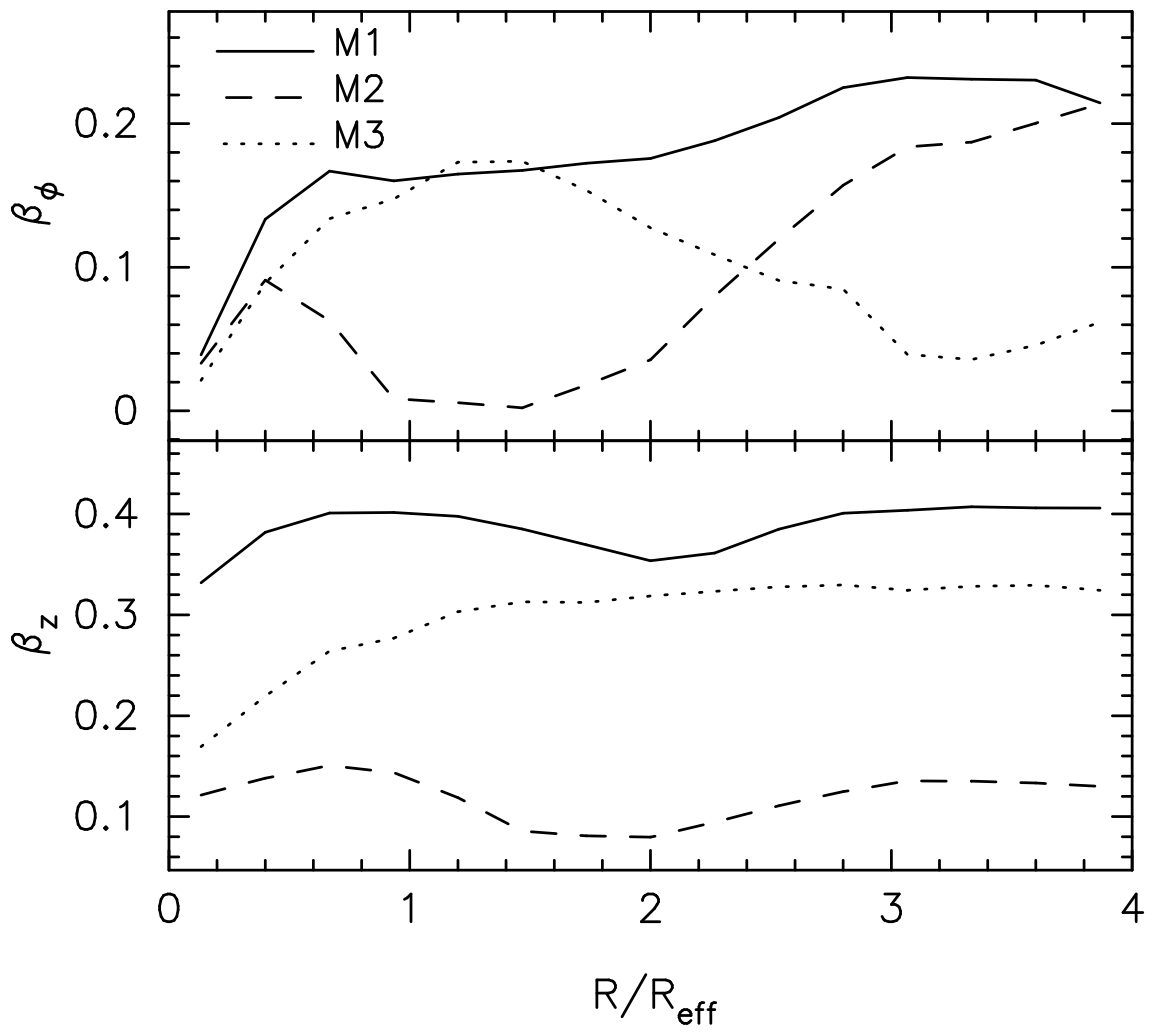


Figure 3.9: Final anisotropy β_ϕ (top) and β_z (bottom) in runs M1, M2 and M3.

merger of SCs produce fast rotating NCs, however the observed profiles of the line-of-sight velocities and the second moment of velocities cannot be reproduced by this formation process. Moreover the complex star formation history of observed NCs indicates that the formation is caused by periodic star formation episodes. Thus, in this section I study the multiple accretion of SCs onto a NC seed. The latter is a super star cluster formed in the central region as in NGC 253, which has fallen to the centre of the galaxy. The periodic star formation episodes are produced by the multiple accretion of young SCs formed in the vicinity of this NCS seed.

The initial conditions of a main disc are no longer possible for this simulation, because the time needed for the simulation of multiple accretion of SCs is about the crossing time of the main disc. Therefore, I evolve this simulation within the bulge model.

In run A1 I study the accretion of SCs onto a NCS by introducing a spherical isotropic SC inside the bulge model. I form the NCS by letting a massive star cluster fall to the centre. I used SC C3 and started it at 127 pc on a circular orbit allowing it to settle at the centre over 65 Myrs, before I start the accretion of 10 SCs. I use model C5 for the accreted SCs, starting them on circular orbits at a distance of 32 pc from the centre. All SCs are accreted within the same plane, even if this simulation evolves in a bulge, the SCs share the same rotation as it would be the case within the initial conditions of a main disc. In total, the mass accreted corresponds to ~ 3 times the NCS's initial mass. Each accretion is allowed to finish before a new SC is inserted. A single accretion on average requires ~ 20 Myrs. Table 3.2 gives further details of this simulation.

After each accreted SC, I measure R_{eff} by fitting a King profile (Eqn. 3.4) to the mass surface density profile of the NC. The final remnant has $R_{\text{eff}} \sim 3.2$ pc and structural properties consistent with observed NCs, as shown in Figure 3.5, which tracks the evolving NC. The NC becomes triaxial after it has doubled in mass. With

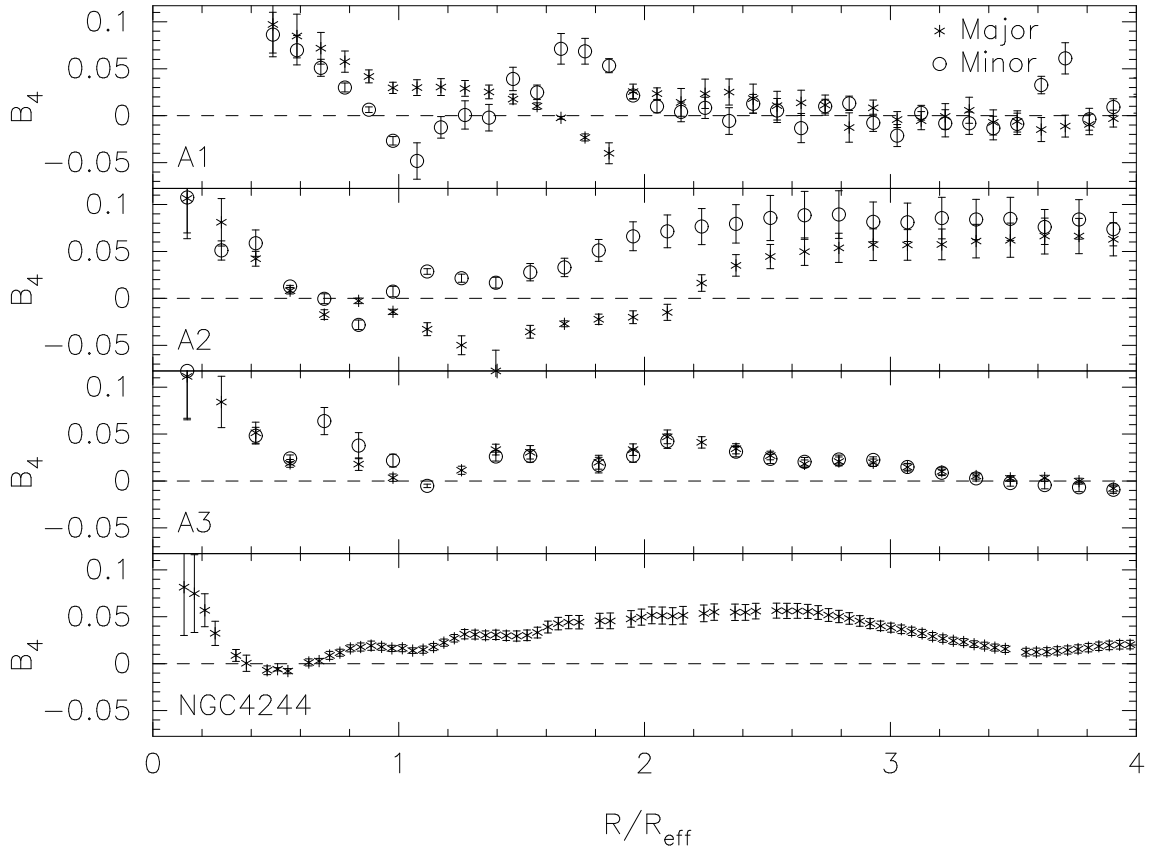


Figure 3.10: B_4 for edge-on projections of runs A1, A2 and A3 compared with the NC in NGC 4244 (bottom). For the simulations we measured the isophotes along the edge-on semi-principal axes.

the final $\varepsilon_{FO} \simeq 0.17$ and $\varepsilon_{EO} \simeq 0.51$, the latter is in the observed range (Seth et al., 2006). The final triaxiality is $T \simeq 0.4$. Figure 3.10 shows that the remnant NC in A1 is discy ($B_4 > 0$).

Multiple accretion of young SCs allows me to also explore the effect of a different M/L ratio for a *young* accreted SC. For the NC in NGC 4244 the structural properties are obtained from I -band observations (Seth et al., 2006) and the kinematics from K -band data (Seth et al., 2008b). I obtain both the M/L in the I -band and K -band for the NCD assuming a single stellar population with an age of about 70 Myrs and a metallicity of $[\text{Fe}/\text{H}] = -0.4$. For the NCS assuming two stellar populations, the first with an age of 1 Gyr with the same metallicity and the second of 10 Gyrs

and a metallicity of $[\text{Fe}/\text{H}] = -1.4$ in NGC 4244. Using the stellar evolution code of Maraston (1998, 2005) this gives $M/L \approx 0.2$ for the NCD and $M/L \approx 1.6$ for the NCS in the I -band and $M/L \approx 0.1$ for the NCD and $M/L \approx 0.8$ for the NCS in the K -band. Throughout the rest of this chapter, I adopt the M/L values in the I -band for the analysis of structural properties and M/L values in the K -band for the kinematics, assuming that stars from the last accreted SC are young while the rest of the stars are old, to obtain a luminosity-weighting. Adopting these M/L values, the final edge-on ellipticity becomes $\varepsilon_{EO} \simeq 0.56$.

I produce a luminosity-weighted density map of the final NC and fit two components, an elliptical King and an exponential disc profile, as in Seth et al. (2006), to measure the structural properties of the NCS and NCD component. While the NCS has $R_{\text{eff}} \sim 3.2$ pc and a flattening $\varepsilon \sim 0.59$, I did not fit a reasonable NCD.

The initial super star cluster is isotropic and has no rotation and remains unrotating after falling to the centre. Figure 3.11 shows the evolution of $(V/\sigma)_e$; after the first accretion the merger remnant's rotation has already increased to $(V/\sigma)_e \simeq 0.23$. By the end of the simulation, the mass-weighted $(V/\sigma)_e \simeq 0.34$ ($\simeq 0.41$ when luminosity-weighted). The velocity field of the remnant; seen in Figure 3.12, shows that the NC is rotating. However V_{rms} is still dominated by the velocity dispersion at the centre even when luminosity weighted. The line-of-sight velocity V peaks at larger radii than observed in NGC 4244 and M33, see Figure 3.13.

The settling of the SC to the centre does not change its dispersion within R_{eff} , since the bulge mass within R_{eff} changes only about 0.6%. The evolution of β_ϕ and β_z is shown in Figure 3.14. The first accretion drives β_ϕ to negative values which slowly increases as more mass is accreted. The final β_z peaks within R_{eff} and declines further out.

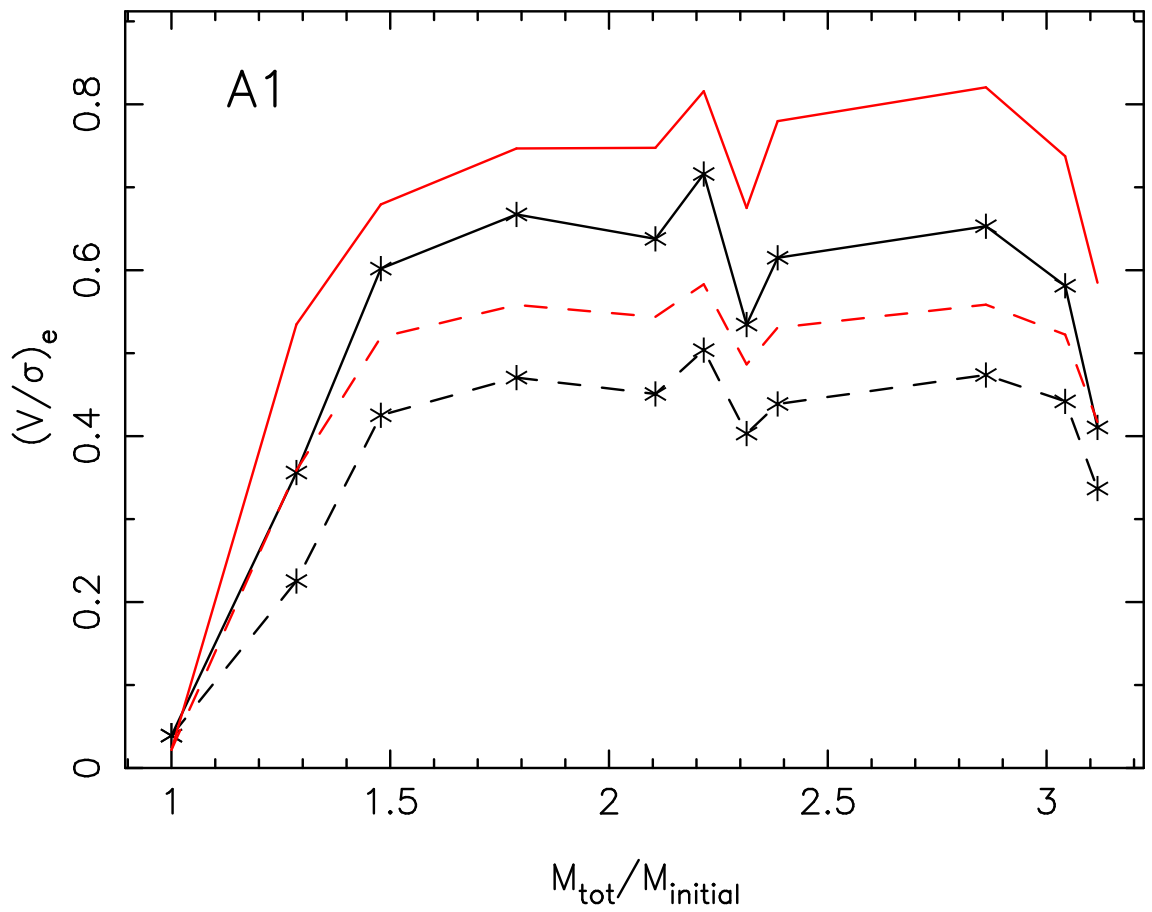


Figure 3.11: The evolution of $(V/\sigma)_e$ in run A1 within R_{eff} (black lines) and $3 R_{\text{eff}}$ (red lines). The dashed lines represent mass-weighted and the solid lines luminosity-weighted measurements as described in the text.

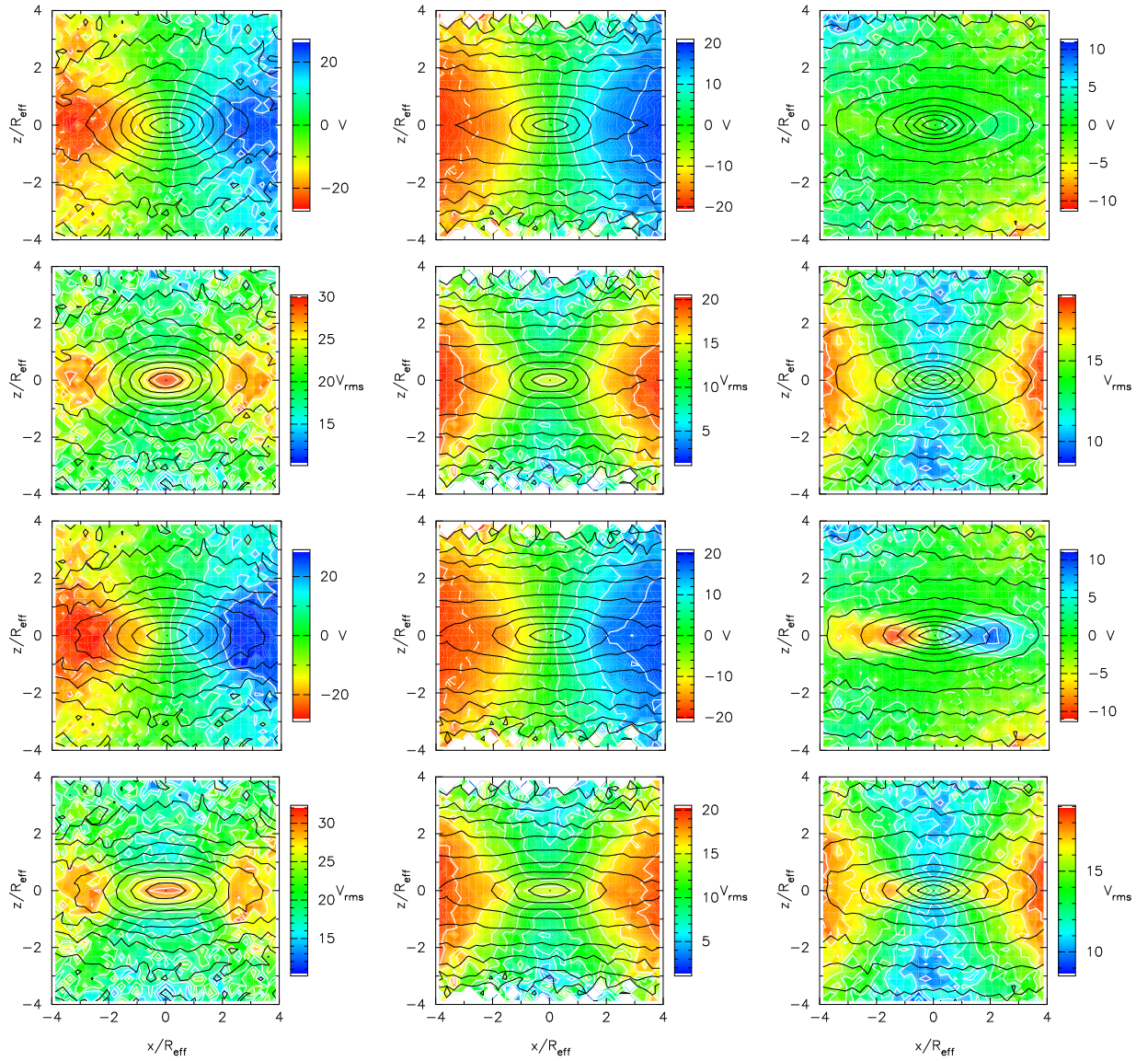


Figure 3.12: Kinematic fields for the accretion simulations A1 (left), A2 (middle) and A3 (right). The top two rows adopt a mass-weighting while the next two rows use luminosity-weighting, as described in the text. In the top four rows the black contours show log-spaced density while the white contours show the kinematic contours corresponding to each panel. Run A3 shows significant rotation only with luminosity-weighting.

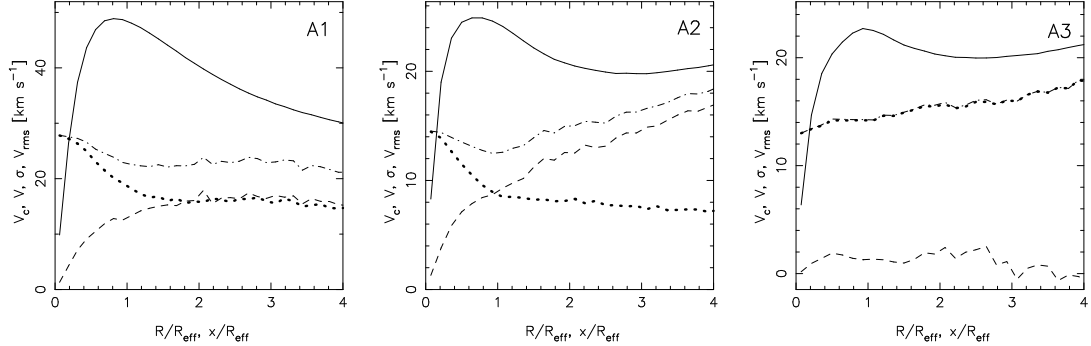


Figure 3.13: Kinematic profiles for the accretion simulations A1 (left), A2 (middle) and A3 (right). It shows the rotation curve $V_c(R)$ (solid lines), the line-of-sight velocities $V(x)$ (dashed lines), the line-of-sight velocity dispersions $\sigma(x)$ (dotted lines) and the root-mean-square velocities $V_{\text{rms}}(x)$ (dashed-dotted lines) along the major axis.

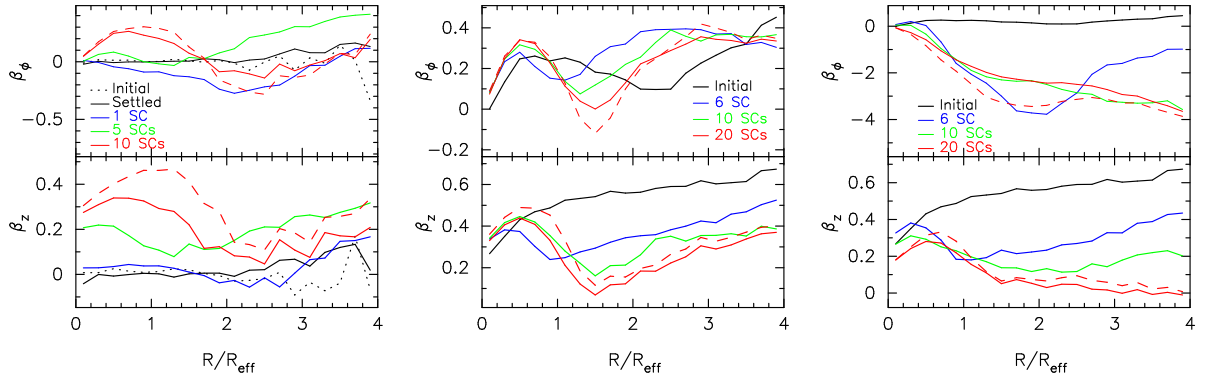


Figure 3.14: The anisotropies β_ϕ (top) and β_z (bottom) after different accretion events for runs A1 (left), A2 (middle) and A3 (right). For A1, I show the initial super star cluster by the black dotted line. For each simulation the red dashed lines show the luminosity weighted anisotropies of the final NC. The lack of net angular momentum in run A3 drives β_ϕ to negative values, even when luminosity-weighting, whereas in run A2 β_ϕ is positive.

3.3 Accretion onto bare NCDs

Here I consider the case of a bare NCD, without an initial NCS, accreting multiple young SCs. I mimic the dissipation formation of a NCD seed by introducing a stellar NCD at the centre of the bulge component. The initial NCD component has a mass of $1 \times 10^6 M_{\odot}$. I use model C4 to represent the infalling SCs, placing them at 63pc from the centre of the NC, since the NCD is barely affected by the SC until it is well within this radius. In run A2 all SCs are on prograde circular orbits, whereas in A3, half of the SCs have retrograde orbits. In total, the NCD accretes 20 SCs, corresponding to 4 times its own mass. All SCs orbit in the plane of the NCD without any vertical motions. Each accretion event requires 20 – 30 Myrs to complete. I allow each accretion to finish before introducing the next SC. In total, these simulations require 1.1 Gyrs. Table 3.2 gives further details of these simulations.

Both remnants have $R_{\text{eff}} \simeq 11.1$ pc and structural properties consistent with observed NCs as shown in Figure 3.5, which tracks the evolving NC. The surface density increases after each accretion event, evolving along the track of observed NCs. When I continue to grow the NC in A2 by accreting a further 30 SCs, the NC becomes denser than the infalling SCs and the surface density continues to increase and does not saturate. Figure 3.15 shows the surface density profiles seen edge-on. The top panels show mass-weighted maps of the surface density. In the middle row of Figure 3.15, I present luminosity-weighted surface density maps, which are more discy than the mass-weighted ones. In the bottom panel of Figure 3.15, I show the surface density profiles.

Like the merger remnants, the accretion remnants can be triaxial. The NC in run A2 is triaxial with a final $\varepsilon_{FO} \simeq 0.22$ and a $T \simeq 0.4$, whereas run A3 is rounder with $\varepsilon_{FO} \simeq 0.05$ and $T \simeq 0.1$. The final edge-on ellipticity at $3 R_{\text{eff}}$ is $\varepsilon_{EO} \simeq 0.60$ for run A2 and $\varepsilon_{EO} \simeq 0.56$ for run A3, and luminosity-weighted ellipticities $\varepsilon_{EO} \simeq 0.73$

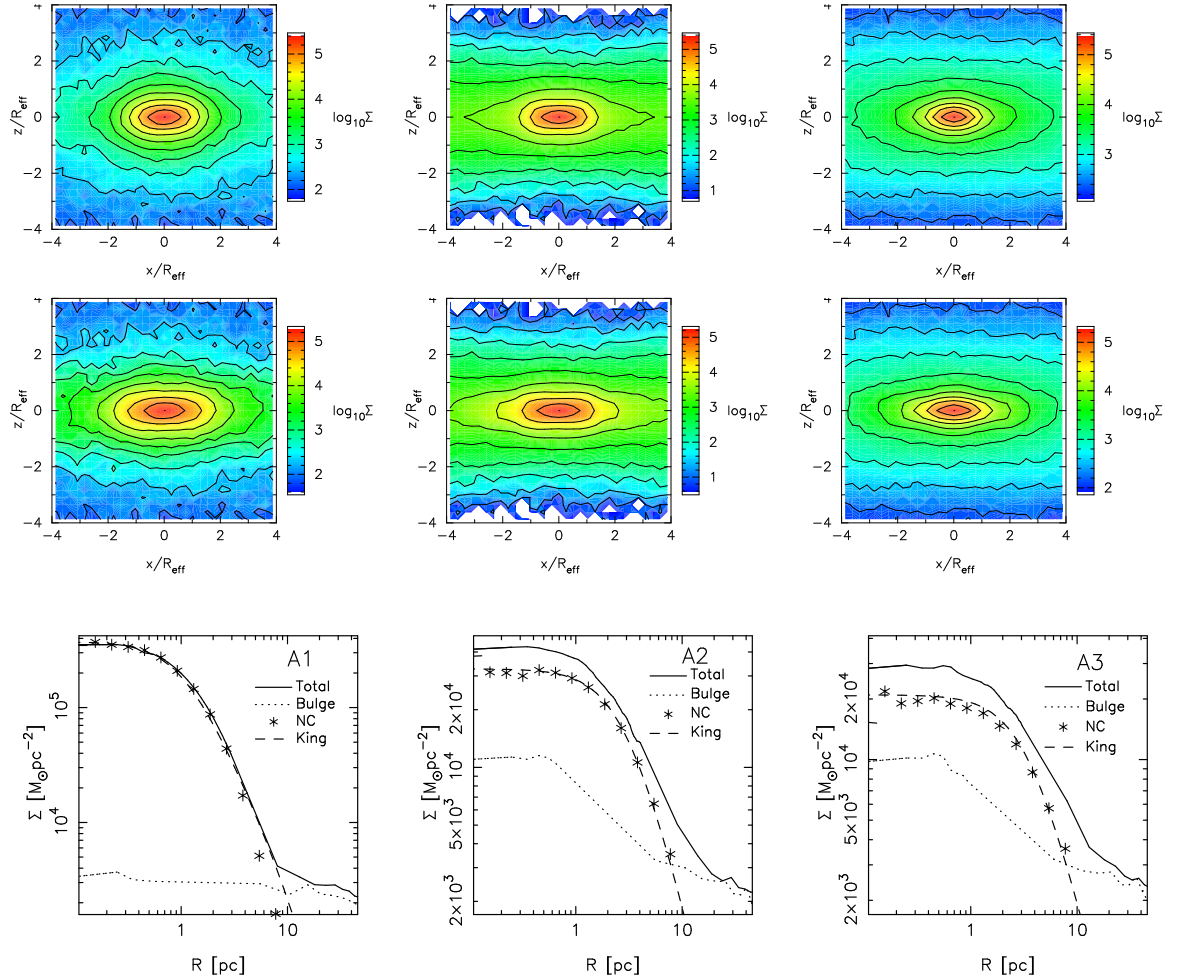


Figure 3.15: Projected surface density maps seen edge-on for simulations A1 (left), A2 (middle) and A3 (right). The top row shows mass-weighted maps and the middle row luminosity-weighted ones. In the bottom panel I show the face-on surface density profiles measured within circular annuli for the NC as stars and the corresponding King profile by a dashed line. The bulge is shown by the dotted line and the combined surface density by the solid line.

in A2 and $\varepsilon_{EO} \simeq 0.66$ in A3, which is in agreement with observed NCs. Accretion leads to the formation of NCs with discy isophotes at large radii as can be seen in Figure 3.10. As in NGC 4244, they show an increase in B_4 towards the centre and a decline further out.

The vertical density profile of the NC in run A2 at R_{eff} is shown in Figure 3.16. The NCD is vertically heated by the accretion of SCs. The last accreted SC is distributed in a thinner component than the initial NCD. I again fit the luminosity-weighted density map with an elliptical King and an exponential disc profile as in Seth et al. (2006). This gives a NCS with $R_{\text{eff}} \sim 9.8$ pc and a flattening of $q \sim 0.37$ and a NCD with $z_0 \sim 1.7$ pc and a scale-length $R_d \sim 3.3$ pc. The NCD accounts for 2% of the NC mass, which is ~ 3 times smaller than in NGC 4244. The scale-height and scale-length of the NCD in run A2 is about the same of that observed in NGC 4244. Thus, structurally, the NC is comparable to that in NGC 4244, provided that the accreted SC is young.

The initial NCD is strongly rotating. Accretion reduces the rotation of the remaining NC. Figure 3.17 shows the evolution of $(V/\sigma)_e$. The first accretion leads to a large decrease in $(V/\sigma)_e$. In run A2, the subsequent accretions induce smaller changes, quickly asymptoting to $(V/\sigma)_e \simeq 0.45$ ($\simeq 0.52$ luminosity-weighted). $(V/\sigma)_e$ increases with radius regardless of which weighting is used. Run A3 instead drops to $(V/\sigma)_e \simeq 0.10$ although a luminosity-weighting gives the appearance of more rotation, $(V/\sigma)_e \simeq 0.40$, comparable to that in run A2.

Figure 3.12 plots the first two moments of the line-of-sight kinematics. The remnant NC in A2 is significantly rotating while the remnant in A3 shows rotation only when luminosity-weighted. The V shown in Figure 3.13 peaks at larger radii compared to those in NGC 4244 and M33. Unlike in runs M1-M3 and A1, the NC remnant in run A2 and A3 have V_{rms} that increases with radius, like the NC of NGC 4244. However the V_{rms} profiles in Fig. 3.13 show that in run A2 V_{rms} increases

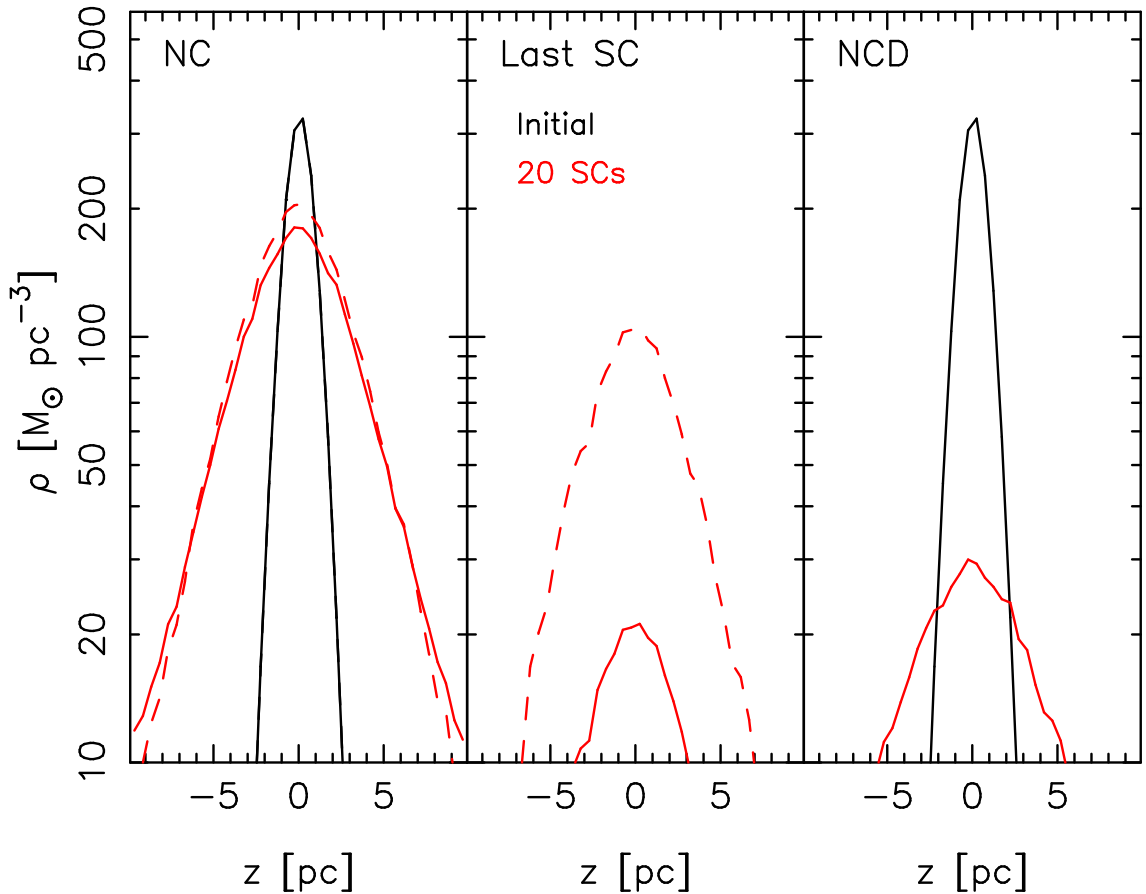


Figure 3.16: The vertical density profile of simulation A2 for the initial NCD (black) and after 20 accreted SCs (red). The solid lines show mass-weighted and the dashed lines luminosity-weighted profiles. I plot the density profile for the total NC, the last accreted SC and the particles of the initial NCD in the left, middle and right panel, respectively.

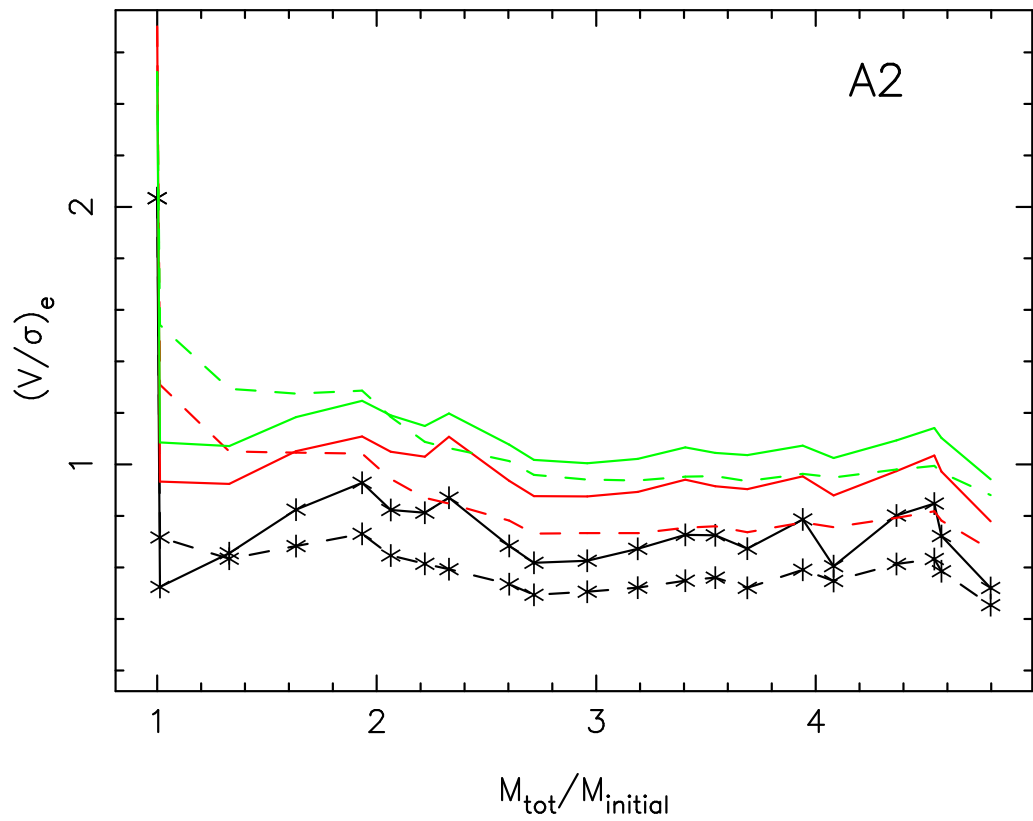


Figure 3.17: The evolution of $(V/\sigma)_e$ within R_{eff} (black lines), $3 R_{\text{eff}}$ (red lines) and $5 R_{\text{eff}}$ (green lines) in run A2. The dashed lines represent mass-weighted and the solid lines luminosity-weighted measurements adopting the M/L of the NCS and NCD in NGC 4244.

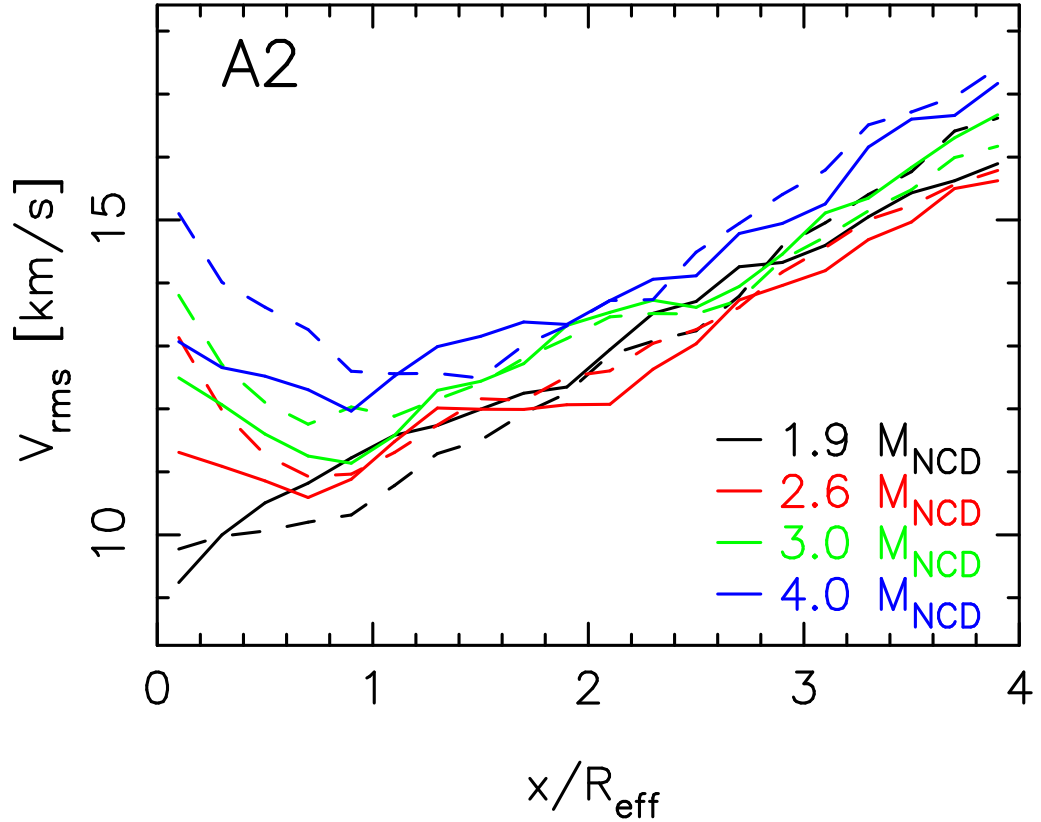


Figure 3.18: The V_{rms} profile after the NC has grown to 1.9 (black lines), 2.6 (red lines), 3.0 (green lines) and 4.0 times (blue lines) the initial NCD's mass. The solid lines show the $V_{\text{rms}}(x)$ of the NC seen side-on and the dashed lines seen end-on.

within R_{eff} . In Fig. 3.18 I show that V_{rms} develops a central peak within R_{eff} after the initial NCD has doubled its mass. Thus NGC 4244 cannot have accreted more than half of its mass as stars.

I adopted the M/L for my analysis which was found for the NCD and NCS in NGC 4244. This is so far the only NC, which has been observed in such great detail. The effect of different M/L on the kinematics is small, besides the amount of rotation as one can see in run A3. First I already use a very young population (≤ 100 Myrs) for the NCD component and secondly the V_{rms} profile and fields are dominated by the NCS containing the older population. Thus V_{rms} is a robust parameter for distinguishing between the proposed formation scenarios.

3.3.1 Vertical anisotropy

As usual for rapidly rotating discs, the initial NCD is radially biased, with β_z initially large, but this decreases with accretion, although it remains positive. Unlike with the kinematic measurements, no important differences in β_z and β_ϕ occur if I weight by luminosity, as shown in Figure 3.17. Regardless of whether mass or luminosity weighting is applied, β_z peaks within R_{eff} , and declines beyond.

The JAM model of the NC in NGC 4244 has a $\beta_z \simeq -0.2$. In Figure 3.19 I test the effect of inclination on β_z . For inclinations $> 75^\circ$ β_z continues to be negative at a 3σ level. I have previously shown in model M2 that accretion of SCs with vertical motions decreases β_z . In run A2, the accreted SCs are in the plane of the initial NCD. In further tests, I let the NC in A2 accrete the 20th SC on a polar orbit using SC models C3, C4 and C5 ($M = 2 \times 10^6 M_\odot$, 2×10^5 , 6×10^5). In Figure 3.20, I show the anisotropy β_ϕ and β_z of the remaining NC after these accretions. Modest accretion off the plane of the disc drives β_z to negative values, within R_{eff} . The accretion of SC C3 drives $\beta_z < 0$ within $4 R_{\text{eff}}$ and it also leads to $\beta_\phi < 0$ within R_{eff} . The accretion of SC C5 causes $\beta_z < 0$ within R_{eff} and $\beta_\phi < 0$ only within $< 0.5 R_{\text{eff}}$. Thus, the observed negative β_z requires that the NC accretes at least $\sim 10\%$ of its mass directly as stars.

3.4 JAM models of simulated NCs

To compare the rotation of real NCs and simulated ones in a fully consistent way, I applied the same JAM approach to measure the rotation of the simulated NCs. The MGE models were fitted to reconstructed images of all models listed in Table 3.2 at an edge-on orientation, for different viewing directions in the disc plane. For each projection, I fitted the anisotropy β_z and M/L of the simulated NCs, and I then measured the rotation parameter κ at the best-fitting $(\beta_z, M/L)$. The inferred

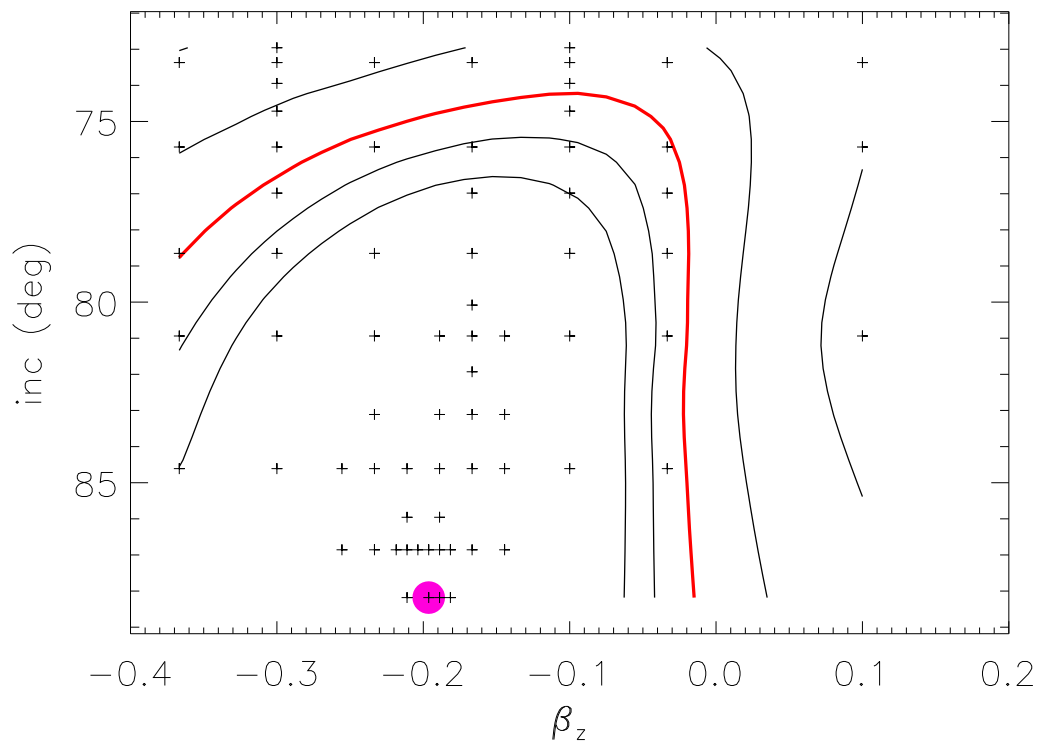


Figure 3.19: The anisotropy β_z for different inclinations. The purple filled circle shows the best fitting model for the NC in NGC 4244. The black solid lines shows the contours of the uncertainty levels. The red solid line is the uncertainty at 3σ .

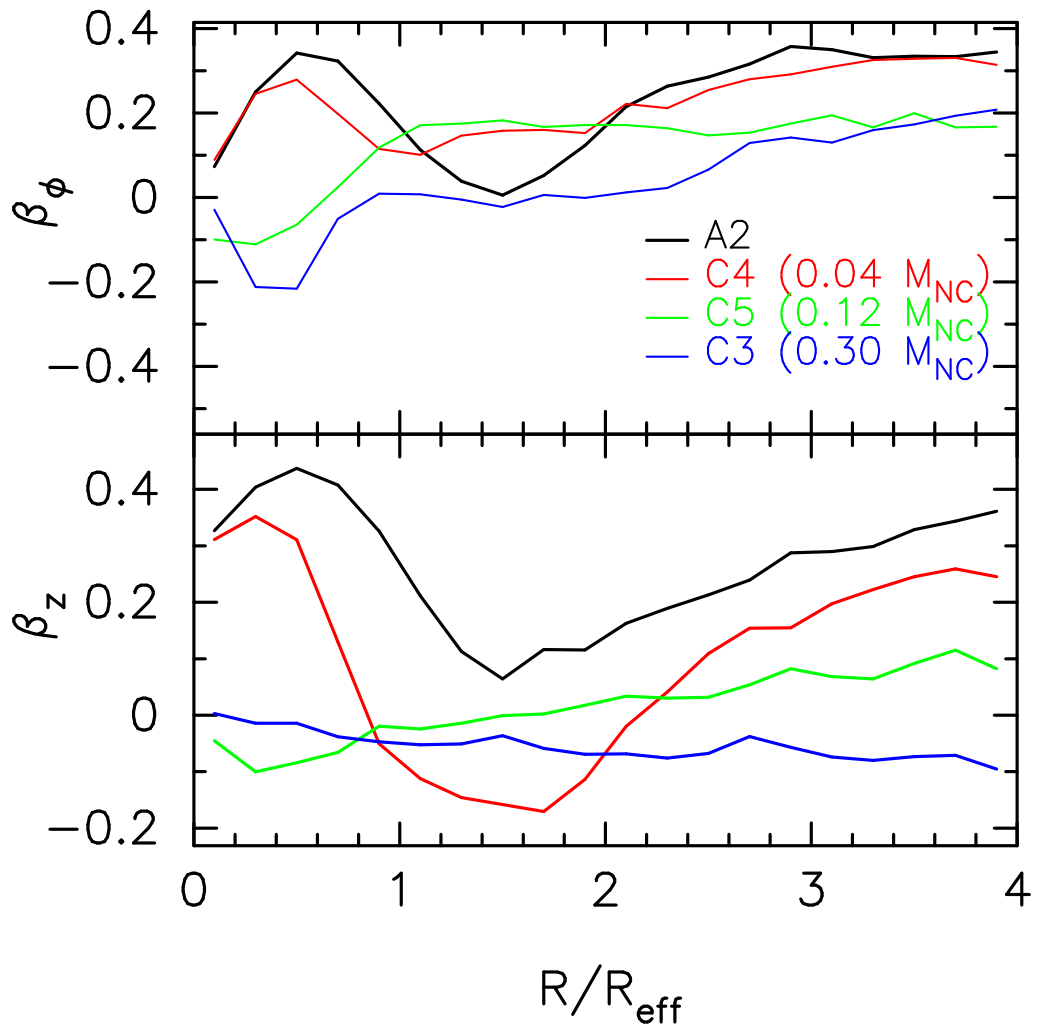


Figure 3.20: The anisotropies β_ϕ (top) and β_z (bottom) for A2 after the accretion of 20 SCs and for the three test runs if we replace the final accreted SC with the indicated SC on a polar orbit.

parameters are given in Table 3.3 and compared with the values measured from the particles. The comparison shows that the simple JAM models capture the global anisotropy of the simulated NCs of the merger simulations, and gives confidence in the values I extracted from the real data. In summary, for all simulations, as with the observations, I measure a degree of rotation $\kappa \approx 1$ within 5% for models M1 and M2, and within 10% for model M3. Given the complex accretion process of the NC, it is remarkable for the rotation to be so closely linked to the NC shape. This result is similar to what was found for real galaxies in Cappellari (2008) and suggests that a general process may be responsible for both observations. For the models of the merger simulations I recover a weak anisotropy, with models M1 and M3 anisotropic with $\beta_z \approx 0.25$ and $\beta_z \approx 0.17$, respectively, while model M2 is closer to fully isotropic with $\beta_z \approx 0.04$ within $3 R_{\text{eff}}$. Contrary to models M1-M3, the JAM models do not represent acceptable models for the accretion simulations A1-A3. In fact the kinematics predicted from the simulated photometry under the assumption of constant M/L and an oblate velocity ellipsoid, is qualitatively quite different from the simulated one. The main reason for this discrepancy is due to the strong variation in the M/L in the simulated NC, which is not included in the JAM models. Although it would be easy to construct JAM models using the gravitational potential directly measured from the simulations, this cannot be easily done from the observations. However, in all accretion simulations the global rotation can robustly be determined by JAM.

I perform an independent measure of the degree of rotation of the simulated NCs using Eqns. 2.3 and 2.4 to place simulations M1-M3 and A1-A3 on the $(V/\sigma, \varepsilon)$ diagram. While I used the line-of-sight velocities obtained from a fit of a Gauss-Hermite series to place the observed NCs in NGC 4244 and M33 on the $(V/\sigma, \varepsilon)$ diagram, for the simulations I use the mean line-of-sight velocities. For NCs M1-M3 the diagram provides results consistent with the JAM models, for both simulated

Table 3.3: Global cylindrical anisotropy and parameters from the JAM models for the simulations and observations. I also present the values measured directly from the simulations.

Run	JAM MGE			Simulation	
	β_z	κ	ε_{EO}	$\langle\beta_\phi\rangle$	$\langle\beta_z\rangle$
M1	0.25	0.94	0.55	0.15	0.38
M2	0.04	0.99	0.37	0.08	0.10
M3	0.17	0.90	0.56	0.17	0.26
A1	n.a.	n.a.	0.56	0.05	0.35
A2	n.a.	n.a.	0.73	0.10	0.31
A3	n.a.	n.a.	0.66	-1.92	0.20
NGC 4244	-0.2	1.06	0.43		
M33	0.0	0.84	0.28		

and observed NCs. In particular, both models M1 and M3 are in a location of the diagram which indicates significant anisotropy, while model M2 and the observed NCs of M33 and NGC 4244 are close to the isotropic line (with a typical uncertainty of ~ 0.1). The measured values are shown in Figure 3.21. To first order, the diagram shows that both the simulated clusters and the real ones are rapidly rotating. The simulated NCs in runs M1 and M3 are flatter than M2, but have a similar $(V/\sigma)_e$. The NCs in the accretion simulations A1-3 are more flat than the merger simulations, M1 and M3. They have comparable $(V/\sigma)_e$, although in A3 only the last accreted SC causes the rotation. All these results are consistent with the findings of the JAM models.

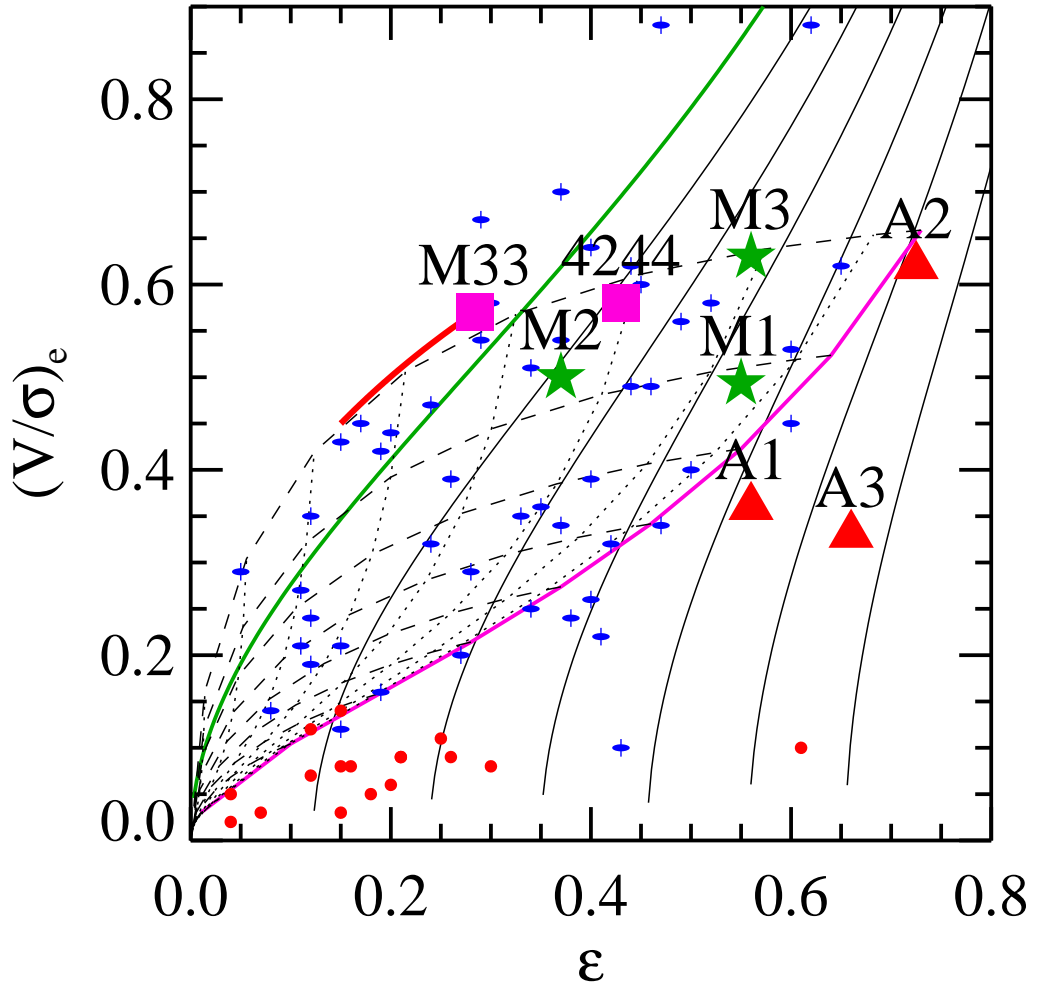


Figure 3.21: Real and simulated NCs on the $(V/\sigma, \varepsilon)$ diagram of Binney (2005). The thick green line indicates the location of edge-on isotropic models, while the other solid lines are anisotropic models with global anisotropy $\delta \equiv 1 - 2\sigma_z^2 / (\sigma_\phi^2 + \sigma_R^2)$, spaced at 0.1 intervals. The magenta line is the lower envelope for fast-rotating galaxies defined in Cappellari et al. (2007). The dashed lines indicate how the magenta line transforms at lower inclinations in 10° steps, indicated by the dotted lines. The green stars and red triangles indicate the location of the simulated NCs, while the magenta squares are the observed NCs. The observed location for M33 has been projected (red line) assuming an inclination of $i = 49^\circ$. For comparison I also plot the fast-rotator (blue dots) and slow-rotator (red circles) early-type galaxies from Cappellari et al. (2007). Both the simulated and real NCs are fast rotating and relatively close to the isotropic line.

3.5 Discussion

3.5.1 In situ formation versus accretion

I have examined, in detail, the formation of nuclear clusters (NCs) via the mergers of star clusters (SCs). This has been proposed as an important avenue for NC formation (Tremaine et al., 1975; Miocchi et al., 2006; Capuzzo-Dolcetta & Miocchi, 2008a; Agarwal & Milosavljević, 2011). The main support for this mechanism comes from the similarity of the scaling relations between SCs and NCs (Lotz et al., 2001; Walcher et al., 2005). In agreement with previous studies (Bekki et al., 2004; Capuzzo-Dolcetta & Miocchi, 2008a,b), I find that such scaling relations are preserved after mergers.

As with previous studies (Bekki et al., 2004), the merger of SCs was found to produce triaxial NCs, but I have shown that axisymmetry can result from the presence of intermediate mass black holes (IMBH) or sufficient vertical motions. In the only observed galaxy where the face-on shape can be determined, M33, I showed that the NC is most likely axisymmetric. When the simulated NCs are viewed edge-on, mergers produce boxy NCs, unless the merger of SCs occurs onto a pre-existing super star cluster or a pre-existing nuclear cluster disc at the centre. The flattening is in the range of observed NCs in edge-on galaxies (Seth et al., 2006).

My simulations indicate that a NC formed via merging of cored SCs leads to a cored NC (Dehnen, 2005). During the merger, the NC density and mass increases and the NC evolves along the track defined by the observed density-mass relation for NCs. The increase in density does not saturate. The accretion of SCs leads to growth in mass, size and mean density of the NC. As seen in Figure 3.5, observed NCs and Milky Way globular clusters (GCs) overlap in the range $10^2 < \Sigma_e < 10^5 \text{ M}_\odot \text{pc}^{-2}$. Some observed NCs are denser than the present-day Milky Way GC population. Studies of young massive SCs in interacting galaxies (Whitmore & Schweizer, 1995;

McCradly & Graham, 2007) show that they have similar masses ($10^5 - 10^6 M_\odot$) and similar sizes as the Milky Way GCs (Bastian et al., 2006, and references therein). Due to the smaller infall times of massive SCs (Milosavljević, 2004; Neumayer et al., 2011), the mergers of these massive SCs is more likely. Thus, if the main formation mechanism of NCs is the accretion of SCs, it would explain why NCs are denser than the present day GC population.

Observed NCs contain a thin, blue disc of young stars (< 100 Myrs). In NGC 4244, the mass of this disc is about 5% of the total NC mass - if this is typical for the lifetime of a galaxy, then over a Hubble time, dissipation and star formation is sufficient to build the NC (Seth et al., 2006). On the other, hand I have shown that even if the accreted SCs confer no net angular momentum to the NC, because the last accreted young SC dominates the luminosity, the apparent rotation can be quite large. I found that mergers can produce rapidly rotating NCs, having $(V/\sigma)_e$ values as large as those observed (Seth et al., 2008b). However, the second moment of the line-of-sight velocity distribution V_{rms} , is centrally peaked, unlike in the observations. It is only if I introduce a rapidly rotating ($(V/\sigma)_e \simeq 2.0$) nuclear disc at the centre of the initial system that the subsequent evolution produced by infalling SCs is able to qualitatively reproduce the observed V_{rms} field as well as the observed isophotal shape, degree of rotation and mass-density relation, provided no more than half of the NC's mass is accreted. Thus a pure merger origin of NCs can be excluded.

Our JAM model of the NC in NGC 4244 has a negative $\beta_z = -0.2$. Because Cappellari (2008) found that a decrease in inclination leads to an increase in β_z , I tested the effect of inclination on β_z for the JAM model of NGC 4244. For inclinations $> 75^\circ$, I found β_z continues to be negative at a 3σ level. Thus the $\beta_z < 0$ in NGC 4244 cannot be a projection effect and must be intrinsic. However, a NC disc formed out of gas cooling would have $\beta_z > 0$. For example, the JAM model of the NC in NGC 404 has $\beta_z \sim 0.5$ (Seth et al., 2010). In this case the observed burst of

star formation ~ 1 Gyr ago could easily have fed its NC and given rise to its positive β_z . By scattering box orbits, central black holes can lower β_z (e.g. Merritt & Quinlan, 1998). Seth et al. (2008a) find indirect evidence of supermassive black holes (SMBHs) with masses ranging from 10 – 100% in $\sim 10\%$ of NCs. In NGC 4244, the radius of influence for the largest possible intermediate mass black hole is < 1 pc, while the NC has $R_{\text{eff}} = 5$ pc. Therefore, the presence of a intermediate mass black holes in the centre of NGC 4244 cannot explain its $\beta_z < 0$. The only way I were able to produce $\beta_z < 0$ was through the accretion of SCs on highly inclined orbits. Thus, at least $\sim 10\%$ of the mass of the NC of NGC 4244 needs to be accreted as SCs in order to obtain $\beta_z < 0$, which constitutes a lower limit on the amount of mass accreted in the form of star clusters.

3.5.2 Nuclear Cluster Formation in Dwarf Elliptical Galaxies

Our simulations can also make testable predictions relating to the formation of nuclei in dE galaxies. Lotz et al. (2001) suggested that NCs in dE galaxies could have formed by the merger of GCs. They found a depletion of the most massive GCs relative to the less massive ones, in the inner region of galaxies. They interpreted this as being due to shorter dynamical friction infall timescales for massive GCs than for the lower mass ones. In the ACS Virgo Cluster Survey, Côté et al. (2006) found that, on average, NCs in dE galaxies are 3.5 mag brighter than the mean GC. So if NCs form via the mergers of GCs, on average about 25 GCs need to merge. Similar to what I found for NCs in late-type spiral galaxies (Figure 3.5), Côté et al. (2006, see their Figure 18) found that the NCs are denser than the mean density of the GC population in dE galaxies. They also found that the fraction of red GCs and the $(g - z)'_{AB}$ colour of NCs increases with host galaxy luminosity (Peng et al., 2006; Côté et al., 2006). Using Monte Carlo simulations, and assuming that these NCs

formed via mergers, Côté et al. (2006) found that the resulting scaling relation of the NC's colours is less steep than those observed. From spectroscopic data Paudel et al. (2010) found that the metallicity of NCs, in a sample of dE galaxies, correlates with the luminosity of the host galaxy. They also found that the median difference in age between the NC and the galactic main body is about ~ 3.5 Gyrs and that the difference is more prominent in dEs with discy isophotal shapes. This implies that the formation of NCs in dEs might be enhanced by the accretion of gas. In contrast, Paudel et al. (2010) found fairly old and metal-poor NCs in very faint dEs, resembling the properties of the GC population. This suggests that NCs in faint dEs might have formed by different processes than the NCs in brighter dEs.

In summary, both the accretion of gas with in situ star formation and the merger of GCs could be at work to form NCs in dE galaxies. If NCs in dEs form via the merger of GCs, our simulations indicate that they will have boxy shapes, have centrally peaked V_{rms} and be radially biased. On the other hand, if the main formation mechanism is dissipation, NCs will have discy isophotes and no centrally peaked V_{rms} . At present, no available observational data exists which is able to test these predictions.

3.5.3 The $M_{\text{CMO}}-\sigma_e$ relation

The star formation histories in NCs of late-type spiral galaxies are extended, with the youngest population of stars less than 100 Myrs old (Walcher et al., 2006; Rossa et al., 2006; Seth et al., 2010). NCs appear to be offset from the $M_{\bullet} - \sigma_e$ relation of SMBHs (Ferrarese et al., 2006; Wehner & Harris, 2006). NCs have the same slope, but, for a given velocity dispersion σ_e , are 10 times more massive than SMBHs. McLaughlin et al. (2006) found that this offset can be explained by feedback from stars and supernovae. Our simulations indicate that at least 10% of the mass of NCs needs to be accreted by SCs and that at least 50% of its mass needs to be

accreted as gas. Therefore, a fraction of the star formation could occur outside the NC. However, the accreted SCs have to be young and have to have formed within the central region. SCs with masses in a range of $10^5 - 10^6 M_{\odot}$ have to be formed within $60 - 200$ pc, otherwise their infall times are longer than 100 Myrs. Even if the NC has accreted half of its mass in young SCs, stellar feedback occurs within the central region of the galaxy and therefore remains a plausible explanation for the $M_{\text{NC}} - \sigma_e$.

3.6 Summary

In this chapter I have shown a broad analysis of the role of the merger and accretion of SCs in the formation of NCs. The mergers of SCs produce NCs with density and sizes consistent with observations, evolving along the track of observed NCs. Remnant NCs can be axisymmetric. Multiple accretions of young SCs onto a pre-existing nuclear cluster spheroid can also produce discy isophotal shapes. Mergers can lead to rapidly rotating NCs, as observed. They have $\beta_z \lesssim 0.4$, where initial vertical motions induce the smallest values of β_z . However, these NCs have centrally peaked V_{rms} unlike observed NCs in late-type discs.

I have mimicked the accretion of gas and formation of a NCD as observed in the NC of NGC 4244, by introducing a rotating NCD which subsequent accretion of SCs. The accretion of young SCs onto this bare NCD produces NCs with densities, sizes and ellipticities comparable to those observed. They show discy isophotes and have rotations comparable to those in the NCs of NGC 4244 and M33. V_{rms} is dominated by dispersion if the accreted mass is greater than the initial mass of the NCD. The formation of the NC in NGC 4244 therefore requires at least 50% of the mass to be accreted as gas to match the observations.

On the other hand, the observed negative β_z in the NC of NGC 4244 requires at least $\sim 10\%$ of its total mass to have been accreted from SCs. This is the first time

that I have found evidence for the direct accretion of stars onto NCs. In the case of NGC 4244 the NC seems to constrain a hybrid scenario for its formation.

I caution that even if the accreted SCs do not impart any net angular momentum, the last accreted SC can dominate the apparent rotation when luminosity-weighting and could be similar to the $(V/\sigma)_e$ and V_{rms} fields of observed NCs.

These results show that the simulations are now ahead of the observations with predictions of detailed observables that can be used to constrain the formation scenarios better. Integral-field observations of the kinematics of more NC are essential for further progress.

Chapter 4

Consequences of bar formation on the $M_{\bullet} - \sigma_e$ relation

4.1 Numerical methods

I use the set of 25 Milky Way spiral galaxy simulations presented in Widrow et al. (2008). Therefore, I only describe briefly the setup of the simulations and refer the reader to Widrow et al. (2008) for a more detailed description.

4.1.1 Galaxy models

The galaxy models consist of a disc, bulge and dark matter halo. The distribution function is of the form:

$$f(\mathcal{E}, L_z, E_z) = f_d(\mathcal{E}, L_z, E_z) + f_b(\mathcal{E}) + f_h(\mathcal{E}) , \quad (4.1)$$

where $\mathcal{E} \equiv -E$ is the relative energy, L_z is the angular momentum about the symmetry axis and E_z is the vertical energy of stars in the disc (Kuijken & Merrifield, 1995; Widrow & Dubinski, 2005). The distribution functions for the halo and the

bulge are found via an inverse Abel transformation (Binney & Tremaine, 2008)

$$f_{b,h}(\mathcal{E}) = \frac{1}{\sqrt{8\pi^2}} \int_0^{\mathcal{E}} \frac{d^2 \tilde{\rho}_{b,h}}{d\Psi_{\text{tot}}^2} \frac{d\Psi_{\text{tot}}}{\sqrt{\mathcal{E} - \Psi_{\text{tot}}}}, \quad (4.2)$$

where the relative potential $\Psi_{\text{tot}} \equiv -\Phi_{\text{tot}}$ and $\tilde{\rho}_{b,h}$ are the chosen density profiles for the bulge and halo, respectively. The distribution function for a Sérsic profile was found by using the method described by Ciotti (1991). The distribution function for the halo with a Navarro-Frenk-White profile was found by Zhao (1997); Widrow (2000); Lokas & Mamon (2001). The relative potentials Ψ for the bulge and halo are determined from the densities profiles $\tilde{\rho}_{b,h}$ by satisfying Poisson's equation:

$$\nabla^2 \Psi = -4\pi \tilde{\rho}_{b,h}(R, z, \psi) \quad (4.3)$$

The individual distribution functions $f_{b,h}(\mathcal{E})$ derived by Eqn. 4.2 are symmetric and they have isotropic velocities. For the composite distribution functions, one replaces the Ψ , obtained from $\tilde{\rho}_{b,h}$, with the total gravitational potential including an external potential $\Psi_{\text{tot}} = \Psi_h + \Psi_b + \Psi_d$, where Ψ_h , Ψ_b and Ψ_d are the relative potentials for the halo, bulge and disc. The latter is obtained by using the monopole term of a spherical harmonics expansion.

The density profile for the bulge is represented by

$$\tilde{\rho}_b(R) = \rho_b \left(\frac{R}{R_e} \right)^{-p} e^{-b(R/R_e)^{1/n}}, \quad (4.4)$$

which yields, in projection, the Sérsic law with $p = 1 - 0.6097/n + 0.05563/n^2$ (Prugniel & Simien, 1997; Terzić & Graham, 2005), where n is the Sérsic index, ρ_b the mean density within R_{eff} and R is the projected radius. The constant b is adjusted such that the half mass radius, R_{eff} , contains half of the total projected mass of the bulge. In my models, I use

$$\sigma_b \equiv (4\pi n b^{n(p-2)} \Gamma(n(2-p)) R_e^2 \rho_b)^{1/2} \quad (4.5)$$

with the gamma function $\Gamma(n(2-p))$, rather than ρ_b to parametrize the overall

density scale of the bulge models. For the halo, the density profile is

$$\tilde{\rho}_{\text{halo}} = \frac{2^{2-\gamma}\sigma_h^2}{4\pi a_h^2} \frac{1}{(r/a_h)^\gamma (1+r/a_h)^{3-\gamma}} C(r; r_h, \delta r_h) , \quad (4.6)$$

where C is a truncation function that decreases smoothly from unity to zero at $r = r_h$ within a radial range δr_h , a_h is the scale radius, γ is the central cusp strength and σ_h the velocity scale. I use the function $C(r; r_h, \delta r_h) = \frac{1}{2}\text{erfc}((r - r_h)/\sqrt{2}\delta r_h)$, where $\text{erfc}(x)$ is the complementary error function. For the disc, I adopt an exponential profile

$$\rho_d(R, z) = \frac{M_d}{2\pi R_d^2} e^{-R/R_d} \text{sech}^2 z/z_d , \quad (4.7)$$

where R_d is the scale-length, z_d the scale-height and M_d the total mass of the disc. The disc is truncated at radius R_t . I choose a distribution function where the radial dispersion profile is approximately exponential $\sigma_R^2(R) = \sigma_{R0}^2 \exp(-R/R_\sigma)$, with $R_\sigma = R_d$.

4.1.2 Model parameters

The 25 simulations are set up from a probability distribution for Galactic parameters, such as the Sérsic index of the bulge, the disc scale-length and the disc, bulge and halo masses. Therefore all models initially match the properties of the Milky Way. Details are listed in Table 4.1, but for completeness see also Widrow et al. (2008, Sec. 5-6).

The stability of a stellar disc and the resistance against disc instabilities can be measured by two parameters: Toomre's stability parameter (Toomre, 1964)

$$Q = \frac{\sigma_R \kappa}{3.36 G \Sigma} , \quad (4.8)$$

where σ_R is the radial velocity dispersion in cylindrical coordinates, κ the epicyclic radial frequency, G the gravitational constant and Σ the surface density. Another

parameter to determine the disc's stability is the disc's susceptibility to global instabilities (Goldreich & Tremaine, 1978, 1979)

$$X = \frac{\kappa^2 R}{2\pi G \Sigma m}, \quad (4.9)$$

where R is the radius and m the azimuthal mode number of perturbations. Here, I take $m = 2$ since I am interested in bars. In general, discs with $Q < 2$ and $X < 3$ are unstable to bar formation. The set of initial conditions in this Chapter all have similar observational parameters, but they have very different stability properties with $1.0 \lesssim Q \lesssim 2.0$ and $2.5 \lesssim X \lesssim 4.0$ (see Section 7 in Widrow et al., 2008).

All simulations do not contain a SMBH. An initial SMBH satisfying the $M_\bullet - \sigma_e$ relation (Gültekin et al., 2009b) would have a mass $10^7 M_\odot$. The influence radius of this SMBH would be $R_{infl} = GM_\bullet/\sigma^2 \approx 10$ pc. Thus R_{infl} is smaller than the softening length and therefore the presence of SMBH is negligible. For the analysis I assume that the SMBH has been evolved at the initial time and satisfy the $M_\bullet - \sigma_e$ relation (Gültekin et al., 2009b).

4.1.3 Numerical parameters

The 25 simulations were evolved over 5 Gyrs using a parallel N -body tree code (Dubinski, 1996). The bulge, disc and halo consist of 2×10^5 , 6×10^5 and 1×10^6 particles respectively. The particle softening $\epsilon = 25$ pc for all particles and the simulations were evolved for 10^4 equal time steps of length $\Delta t = 0.5$ Myr. This timestep is sufficient to resolve the structural and kinematical evolution of these galaxies, because it is 1/100 times the crossing time of stars at a radius of 1 kpc with a circular velocity of $v_c = 150 \text{ km s}^{-1}$.

Table 4.1: The sample of disc galaxy simulations used in this study. In the first part I show the run number and the symbol used for this particular simulation throughout the paper. In the second part of the table I present the initial parameters of the simulations, which are the minimum of the Toomre Q and the minimum of the swing amplification parameter X , the disc-to-bulge ratio, D/B , and the halo-to-bulge ratio, H/B , within R_{eff} , the Sérsic index n of the bulge and R_{eff} obtained by calculating the projected radius containing half the mass of the bulge. In the third part I show the parameters of the evolved system: the bar amplitude A_{Bar} at t_1 and t_2 , the aperture velocity dispersion σ_e at $t_0 = 0$, t_1 and t_2 and the scatter $\Delta\sigma_e$ at t_2 .

Number	Symbol	Q	X	D/B	H/B	n	R_{eff} [pc]	A_{Bar} (t_1)	A_{Bar} (t_2)	$\sigma_e(t_0)$ [km s $^{-1}$]	$\sigma_e(t_1)$ [km s $^{-1}$]	$\sigma_e(t_2)$ [km s $^{-1}$]	$\Delta\sigma_e(t_2)$ [km s $^{-1}$]
1	+	1.0	2.5	5.8	0.02	1.0	593	0.140	0.134	102.0	142.0	144.4	7.1
2	*	1.0	3.0	4.8	0.05	1.3	659	0.176	0.180	102.5	137.4	142.0	9.4
3	o	1.0	3.5	4.5	0.04	1.7	649	0.117	0.167	108.9	136.7	144.8	9.6
4	x	1.0	4.0	3.8	0.06	1.5	751	0.177	0.247	103.7	129.6	140.8	10.9
5	□	1.0	4.5	3.6	0.11	1.7	780	0.116	0.219	105.9	120.1	133.0	9.5
6	△	1.25	2.5	5.9	0.02	1.2	649	0.222	0.270	103.7	135.8	145.3	12.5
7	⊕	1.25	3.0	5.0	0.03	1.6	610	0.138	0.212	105.3	133.5	140.9	9.6
8	⊙	1.25	3.5	4.8	0.15	1.3	569	0.149	0.220	107.4	129.8	140.9	10.3

Continued on the next page

Table 4.1 – continued from the previous page

Number	Symbol	Q	X	D/B	H/B	n	R_{eff} [pc]	A_{Bar} (t_1)	A_{Bar} (t_2)	$\sigma_e(t_0)$ [km s ⁻¹]	$\sigma_e(t_1)$ [km s ⁻¹]	$\sigma_e(t_2)$ [km s ⁻¹]	$\Delta\sigma_e(t_2)$ [km s ⁻¹]
9	☐	1.25	4.0	3.6	0.08	1.7	738	0.111	0.178	107.2	116.2	131.1	7.8
10	◇	1.25	4.5	3.7	0.18	1.8	752	0.006	0.139	108.9	108.0	120.9	7.1
11	☆	1.50	2.5	6.3	0.02	1.4	456	0.121	0.137	115.2	132.8	142.7	6.9
12	▲	1.50	3.0	4.8	0.03	1.3	531	0.164	0.134	109.4	128.2	131.9	6.2
13	⊕	1.50	3.5	6.4	0.20	1.0	727	0.260	0.265	94.6	117.4	126.4	11.0
14	☆	1.50	4.0	5.5	0.26	1.0	841	0.176	0.267	95.9	120.4	129.0	11.4
15	■	1.50	4.5	5.4	0.33	1.1	841	0.246	0.308	97.6	115.7	130.2	12.6
16	○	1.75	2.5	5.6	0.02	1.4	600	0.138	0.137	106.3	124.6	128.9	7.5
17	★	1.75	3.0	5.0	0.03	1.3	646	0.175	0.213	104.4	122.3	129.4	9.4
18	□	1.75	3.5	5.3	0.13	1.2	744	0.233	0.303	100.2	119.1	131.5	12.1
19	◦	1.75	4.0	3.6	0.09	1.6	700	0.060	0.165	109.0	111.4	125.1	7.7
20	◆	1.75	4.5	4.2	0.14	1.2	690	0.109	0.290	104.9	111.0	129.9	13.2
21	◆	2.00	2.5	5.6	0.02	1.4	600	0.138	0.137	106.3	124.6	128.9	7.5
22	●	2.00	3.0	5.1	0.05	1.4	686	0.184	0.274	103.9	123.1	133.2	11.3

Continued on the next page

Table 4.1 – continued from the previous page

Number	Symbol	Q	X	D/B	H/B	n	R_{eff} [pc]	A_{Bar} (t_1)	A_{Bar} (t_2)	$\sigma_e(t_0)$ [km s ⁻¹]	$\sigma_e(t_1)$ [km s ⁻¹]	$\sigma_e(t_2)$ [km s ⁻¹]	$\Delta\sigma_e(t_2)$ [km s ⁻¹]
23	○	2.00	3.5	4.6	0.06	1.5	644	0.138	0.239	105.3	116.2	128.9	10.4
24	●	2.00	4.0	3.6	0.07	1.5	645	0.135	0.224	108.2	117.4	129.2	9.5
25	●	2.00	4.5	3.8	0.15	1.4	589	0.006	0.051	111.2	110.8	112.5	3.0

4.2 Evolution of structural properties

All of the simulations form bars within 5 Gyrs. I measure the bar amplitude A_{Bar} as the normalised amplitude of the $m = 2$ Fourier density moment

$$A_{\text{Bar}} = N^{-1} \left| \sum_{j \in \text{disc}} e^{2i\phi_j} \right|, \quad (4.10)$$

where ϕ_j is the two-dimensional cylindrical polar angle in the equatorial plane of the disc of particle j . I consider three different times in the simulations $t_0 = 0$, $t_1 = 2.5$ and $t_2 = 5$ Gyrs, and refer to these times throughout the Chapter. In most simulations, the bar forms by 1 Gyr and continues to grow until t_2 (see Figure 17 in Widrow et al., 2008), while in simulations 1 and 12 the bar amplitude peaks before t_2 at 0.5 and 2 Gyrs, respectively. Measurements of A_{Bar} are presented in Table 4.1.

Bar formation leads to an increase in mass in the centre (Hohl, 1971). In Figure 4.1 I plot A_{Bar} versus the fractional change in mass

$$\Delta M/M_{\text{init}} = (M_{\text{final}} - M_{\text{init}})/M_{\text{init}}, \quad (4.11)$$

where M_{final} is the mass at t_1 or t_2 within R_{eff} and M_{init} the mass at t_0 within R_{eff} . The central mass increases both when I look at the disc particles alone and when both disc and bulge particles are considered. In Figure 4.1 I see that $\Delta M(B + D)/M(B + D)_{\text{init}}$ increases with increasing A_{Bar} . The initial ratio between the mass of the bulge and the disc within R_{eff} is in the range of $2.8 \lesssim B/D(R < R_{\text{eff}}) \lesssim 12.0$ and by t_2 it changes to $1.2 \lesssim B/D(R < R_{\text{eff}}) \lesssim 7.7$. The contribution of the halo mass within R_{eff} is less than 15% of the total mass and I therefore neglect the dark matter halo particles in our analysis.

This increase in disc mass alters the structural properties of the bulge. I obtain the bulge R_{eff} by calculating the projected circular aperture containing half of its mass. I find R_{eff} in the range of $456 < R_{\text{eff}} < 841$ pc at t_0 , decreasing to $439 < R_{\text{eff}} < 747$ pc at t_2 , except in simulation 25, where R_{eff} increases slightly. Throughout the

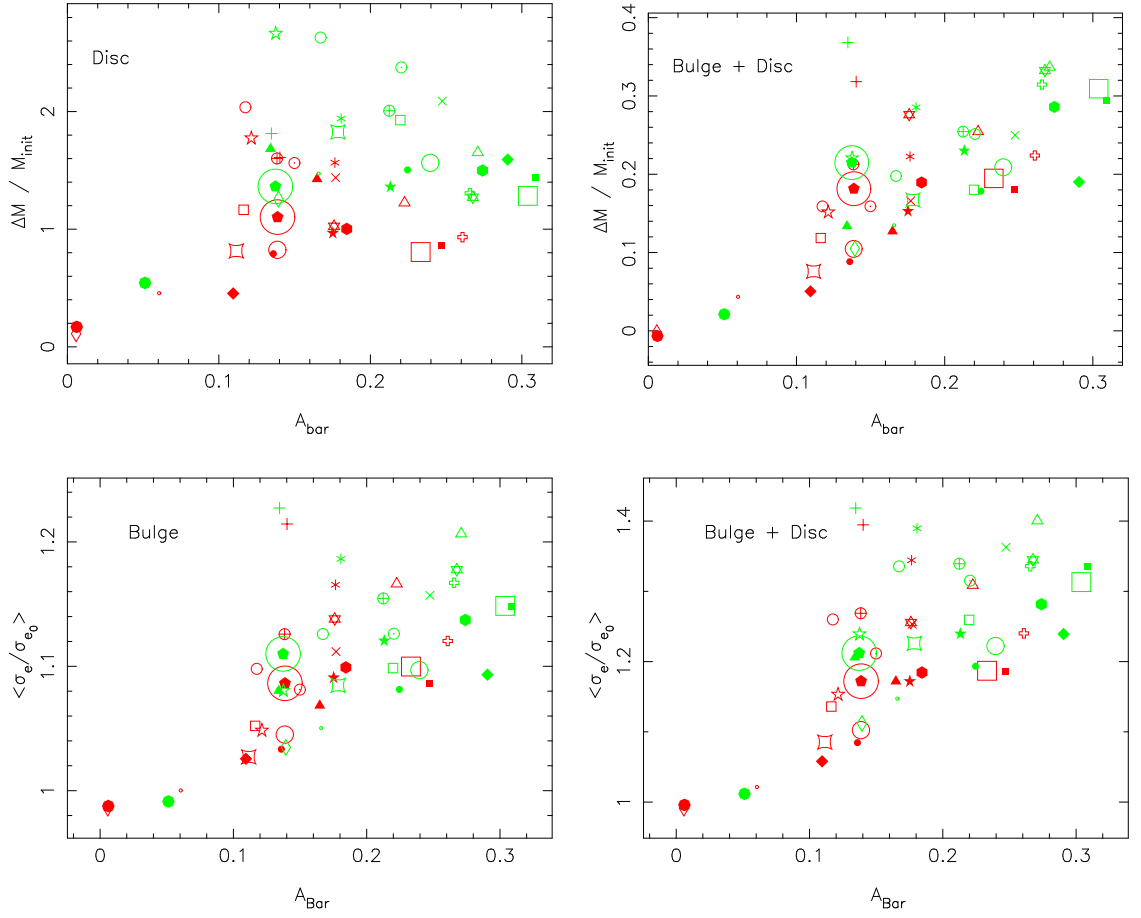


Figure 4.1: Top row: The fractional changes in mass of the disc (left panel) and bulge + disc (right panel) within R_{eff} of the bulge at t_1 (red) and t_2 (green) plotted versus the bar amplitude A_{Bar} . Bottom row: The average change $\langle \sigma_e / \sigma_{e0} \rangle$ at t_1 and at t_2 for the bulge stars and for the bulge + disc stars versus A_{Bar} .

paper all measurements, including those for the disc (D) and bulge + disc (B+D), are computed within R_{eff} of the bulge (B) at that particular time, unless otherwise indicated. I measure the Sérsic index n of the bulge by fitting a Sérsic profile (Sersic, 1968). Initially n has values in the range $1.0 < n < 1.8$, decreasing slightly to $1.0 < n < 1.6$ by t_2 . The growth of the disc compresses the bulge and thus, n decreases (Andredakis, 1998). The initial values of R_{eff} and n are listed in Table 4.1.

4.3 Evolution of Dispersion

The increase in mass in the disc's central region deepens the potential and raises the aperture velocity dispersion σ_e . I measure σ_e within R_{eff} of the bulge as

$$\sigma_e^2 = \frac{\sum_{r_i \leq R_e} m_i v_i^2}{\sum_{r_i \leq R_e} m_i} = \frac{\int_0^{R_e} I(R) (\sigma_{\text{los}}(R)^2 + \bar{v}_{\text{los}}(R)^2) dR}{\int_0^{R_e} I(R) dR} \quad (4.12)$$

where σ_{los} is the root-mean-square of the line-of-sight velocities and \bar{v}_{los} the mean line-of-sight velocity of all particles within R_{eff} . I repeat these measurements of σ_e for four different position angles PA= 0° (bar seen side-on), 30° , 60° and 90° (bar seen end-on) at four inclinations $i = 0^\circ$ (face-on), 30° , 60° , 90° (edge-on). I use the average for σ_e and the root-mean-square of σ_e as its scatter $\Delta\sigma_e$. In Figure 4.1 I plot the average ratio of initial to final σ_e , $\langle\sigma_e/\sigma_{e0}\rangle$ versus A_{Bar} , where σ_{e0} is σ_e at t_0 . On average strong bars lead to large changes in σ_e . The increase in σ_e (B + D) is as large as $\sim 40\%$.

As shown by Debattista et al. (*in prep.*) the ratio σ_e/σ_{e0} depends on

$$\Delta M(\text{B} + \text{D})/M(\text{B} + \text{D})_{\text{init}} . \quad (4.13)$$

In Figure 4.2 I show this correlation. For the correlation in the bulge + disc I find a positive Spearman's rank coefficient $r_s = 0.91$ which is statistically significant corresponding to $> 6\sigma$, and a Kendall rank coefficient $\tau = 0.76$ corresponding to $> 8\sigma$, while in the bulge I find a stronger correlation with $r_s = 0.95$ corresponding to $> 7\sigma$ and $\tau = 0.83$ corresponding to $> 9\sigma$.

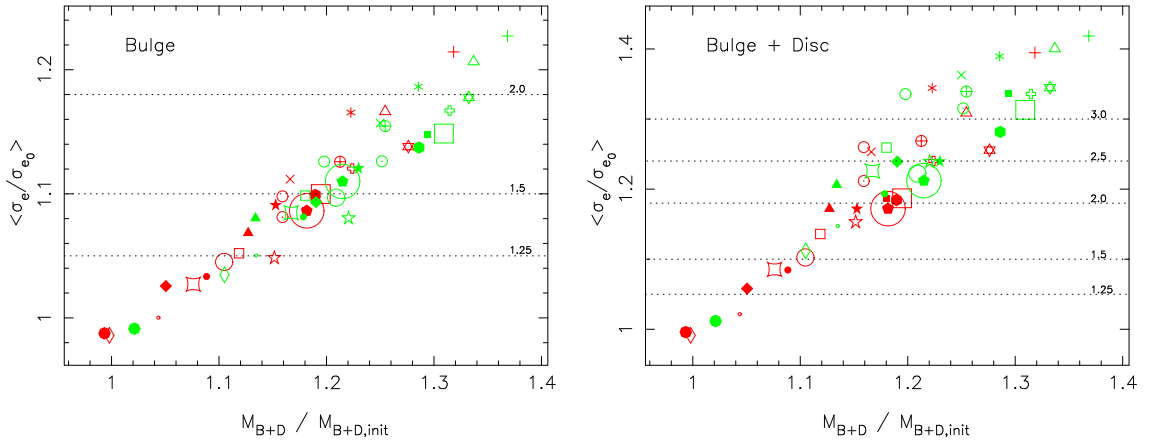


Figure 4.2: Average changes in σ_e at t_1 (red) and t_2 (green) for the bulge stars (left) and for the bulge + disc stars (right) versus the change in mass of the bulge + disc stars within R_{eff} . The change in σ_e correlates with the change in mass within R_{eff} . In both panels the dotted lines indicate contours of constant $(\sigma_e/\sigma_{e0})^\beta$ with $\beta = 4.24$, with the values given above each line.

Bar formation also changes the anisotropy of the disc and of the bulge. I measured the velocity dispersions as the root-mean-square of the velocities in cylindrical coordinates σ_u , σ_v , σ_w , where the coordinates in velocity space u , v and w corresponds to the cylindrical coordinates R , ϕ and z . I obtained the anisotropies

$$\beta_\phi = 1 - \sigma_v^2/\sigma_u^2 \quad \text{and} \quad \beta_z = 1 - \sigma_w^2/\sigma_u^2. \quad (4.14)$$

In Figure 4.3 I show that the initial bulge in all simulations is isotropic by construction. Classical bulges are well described by flattened isotropic rotators (Kormendy & Illingworth, 1982; Davies & Illingworth, 1983). In all runs the bulge becomes mildly tangentially anisotropic by the end of the simulation. The anisotropy in the bulge + disc increases to $\beta_\phi(\text{B} + \text{D}) \sim 0.1$ and $\beta_z(\text{B} + \text{D}) \sim 0.3$. $\beta_\phi(\text{B} + \text{D})$ remains uncorrelated with A_{Bar} , while $\beta_z(\text{B} + \text{D})$ shows a weak correlation with A_{Bar} . Both β_ϕ and β_z seem to saturate, which is most likely due to buckling of the bar limiting how large β_z can get (Araki, 1987; Merritt & Sellwood, 1994). Buckling is caused by the anisotropy (Raha et al., 1991; Merritt & Sellwood, 1994). While bar formation

increases the anisotropy, buckling decreases it to more stable levels.

Bar buckling itself increases the mass in the central reegion (Debattista et al., 2006a; Sellwood & Debattista, 2009) and therefore $\langle\sigma_e/\sigma_{e0}\rangle$ continues to rise. In Figure 4.4 I plot $\langle\sigma_e/\sigma_{e0}\rangle$ versus β_ϕ and β_z . I also calculated the anisotropy in spherical coordinates

$$\beta_t = 1 - (\sigma_\theta^2 + \sigma_\phi^2) / 2\sigma_r^2. \quad (4.15)$$

No correlation is present for bulge particles and disc particles separately, however a very strong correlation is present for bulge + disc stars and is stronger with $\beta_\phi(\text{B} + \text{D})$ than with $\beta_z(\text{B} + \text{D})$ or with $\beta_t(\text{B} + \text{D})$. This surprising correlation also suggests a correlation between $\beta_\phi(\text{B} + \text{D})$ and the fractional change in mass which I show in Figure ???. For this correlation in the bulge + disc I find $r_s = 0.67$ and $\tau = 0.52$ which is statistically significant corresponding to $> 5\sigma$, while in the disc I find anticorrelation with $r_s = -0.15$ and $\tau = -0.12$ which is significant corresponding to $< 2\sigma$. While $\beta_\phi(\text{D})$ and $\Delta\text{M}(\text{B} + \text{D})/\text{M}(\text{B} + \text{D})_{\text{init}}$ anticorrelate, $\beta_\phi(\text{B} + \text{D})$ and $\Delta\text{M}(\text{B} + \text{D})/\text{M}(\text{B} + \text{D})_{\text{init}}$ correlate, but saturates at $\beta_\phi(\text{B} + \text{D}) \sim 0.1$. Thus, this correlation is less strong than the correlation between $\langle\sigma_e/\sigma_{e0}\rangle$ and $\Delta\text{M}(\text{B} + \text{D})/\text{M}(\text{B} + \text{D})_{\text{init}}$.

4.3.1 Contamination from the disc

Depending on the bulge-to-disc ratio, B/D , the contamination by the disc on the measured bulge velocities dispersion may be less important in smaller apertures than in larger apertures. In Figure 4.5, I plot contours of the mass ratio of the bulge-to-disc within R_{eff} and within $R_{\text{eff}}/8$ in the plane of total B/D versus R_{eff}/R_d , where R_d is the scale-length of the disc. For example, in an exponential disc with a bulge having $n = 1.5$, $R_{\text{eff}}/R_d = 0.3$ and $B/D \sim 0.9$, the ratio of bulge to disc mass ~ 50 within $R_{\text{eff}}/8$ and ~ 10 within R_{eff} . In the simulations the ratio of bulge to disc mass varies between 3 and 48 within $R_{\text{eff}}/8$ and between 3 and 12 within R_{eff} . In

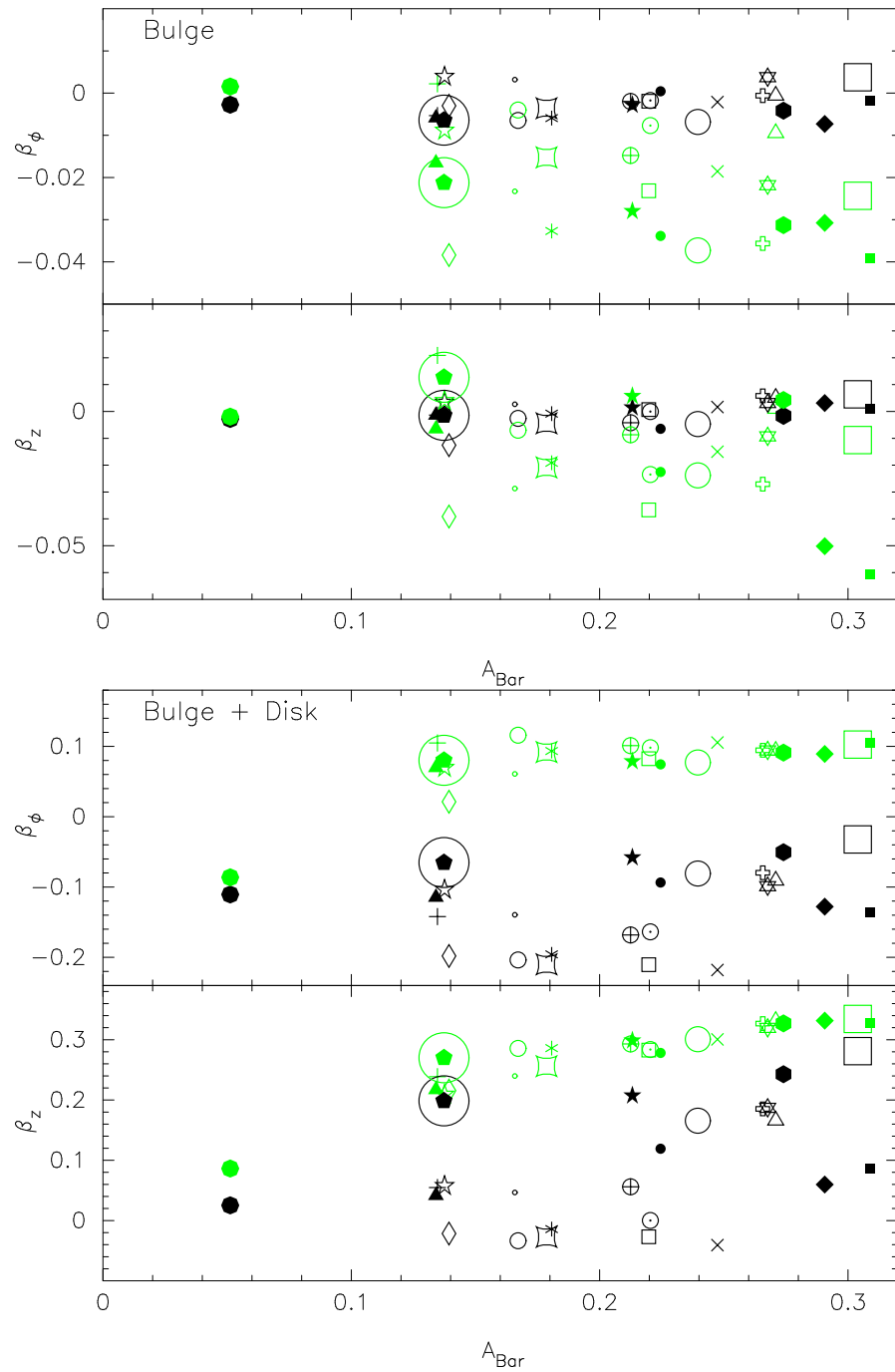


Figure 4.3: The anisotropies β_ϕ (top panel) and β_z (bottom panel) at t_0 (black) and t_2 (green) versus A_{Bar} by t_2 only for bulge stars (top) and for the bulge + disc (bottom). Note that the initial disc has no bar, so A_{Bar} is zero. To see the evolution of the anisotropy, I plot A_{Bar} by t_2 for the anisotropies at t_0 and t_2 .

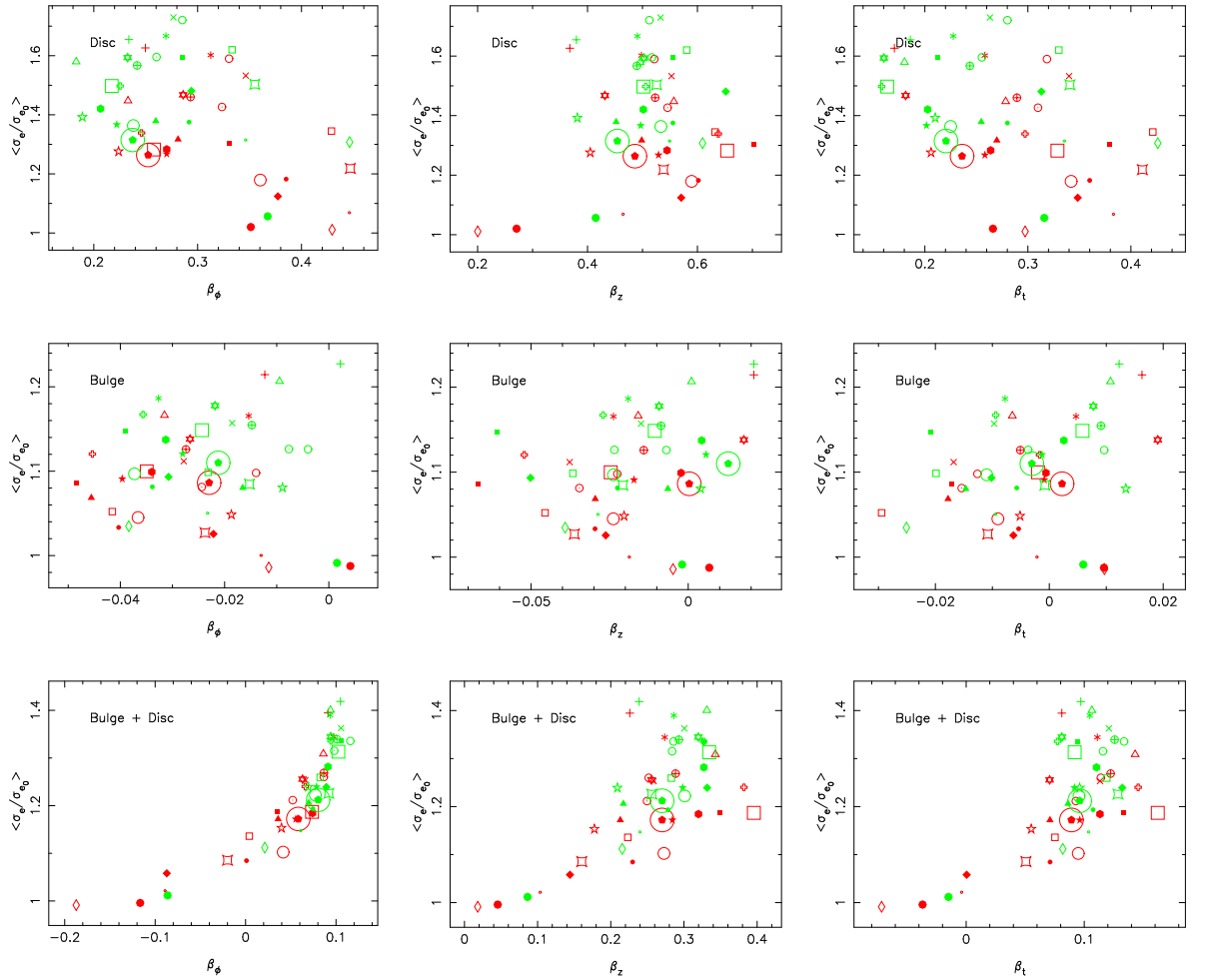


Figure 4.4: The changes $\langle \sigma_e / \sigma_{e0} \rangle$ at t_1 (red) and at t_2 (green) versus anisotropy β_ϕ (left panels), β_z (middle panel), β_t in spherical coordinates (right panels) for the disc (top), for the bulge (middle) and for the bulge + disc (bottom). The bulge + disc system shows a stronger correlation to β_ϕ , β_z and β_t than do the components separately.

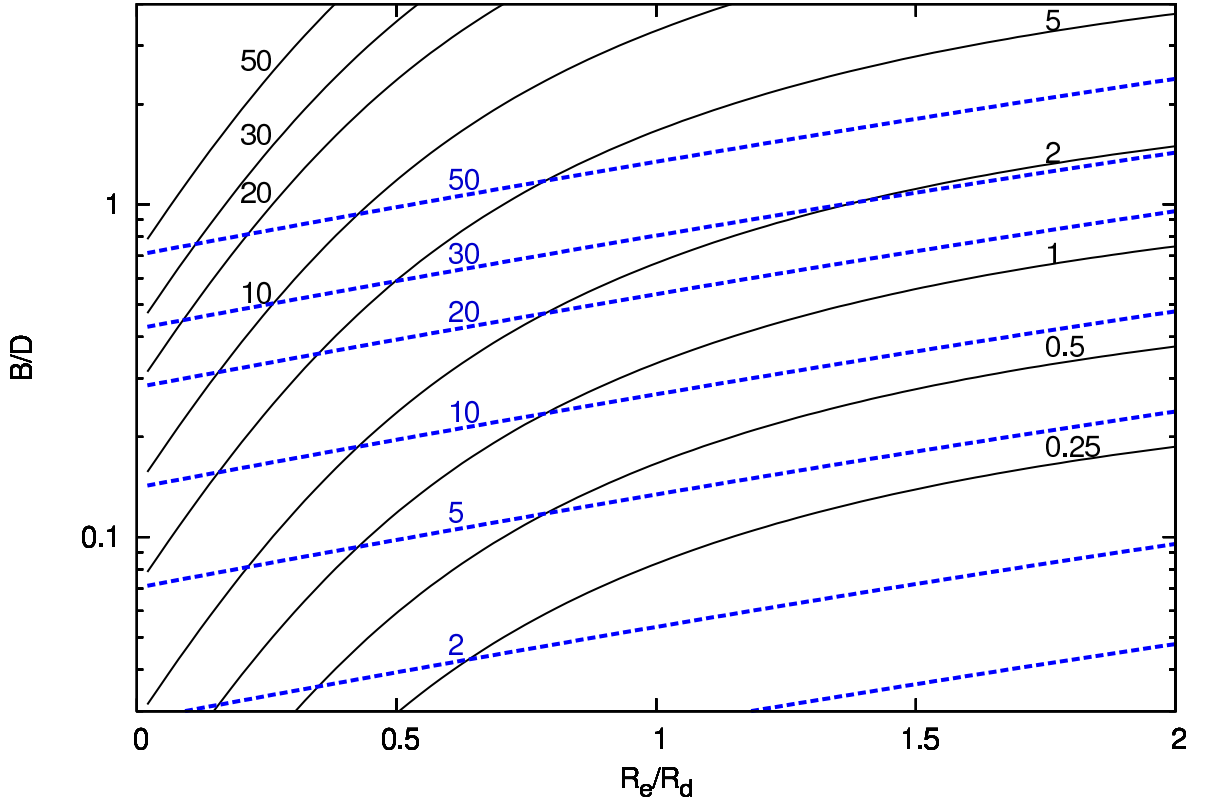


Figure 4.5: The bulge-to-disc mass ratio within R_{eff} (black solid lines) and $R_{\text{eff}}/8$ (blue dashed lines) for an exponential disc and a bulge with a Sérsic profile with $n=1.5$. The mass ratio is given by the values at each line.

order to test whether the disc contamination to the measured $\sigma(B)$ can be reduced through the use of smaller apertures, I compare $\sigma(B+D)$ and $\sigma(B)$ within R_{eff} and $R_{\text{eff}}/8$.

Surprisingly, I find a similar degree of disc contamination for $\sigma_{e/8}$ as for σ_e . In Figure 4.6 I compare $\sigma_e(B)$ with $\sigma_e(B+D)$; while $\sigma_e(B+D)$ correlates with $\sigma_e(B)$ for both R_{eff} and $R_{\text{eff}}/8$. $\sigma_e(B+D)$ is $\sim 1.25\times$ larger than $\sigma_e(B)$, when measured edge-on.

In Figure 4.7 I plot the cumulative distribution of $\sigma_{e/8}(B+D)/\sigma_{e/8}(B)$ and of $\sigma_e(B+D)/\sigma_e(B)$. The two distributions are very similar and the mean of both

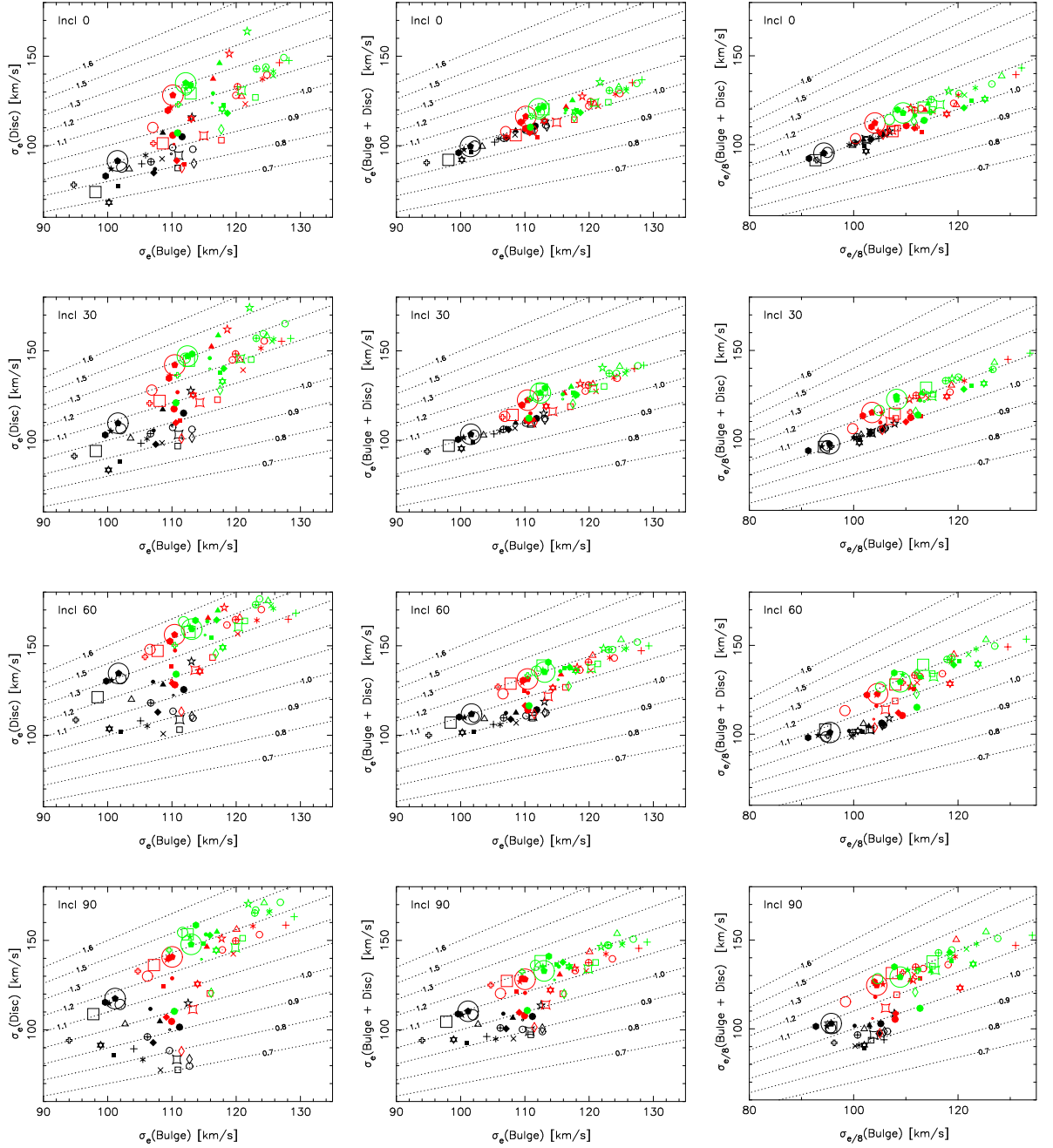


Figure 4.6: σ_e of the disc (left) and bulge + disc (middle) versus σ_e of the bulge. The right column plots $\sigma_{e/8}$ of the bulge + disc versus that of the bulge. Black, red and green represent the models at t_0 , t_1 and t_2 , respectively. I average over $\text{PA} = 0^\circ, 30^\circ, 60^\circ$ and 90° and plot σ 's for inclinations $i = 0^\circ, 30^\circ, 60^\circ$ and 90° from top to bottom. σ_e of the bulge + disc shows a stronger correlation with σ_e in the bulge than σ_e of the disc. For the bulge + disc σ_e and $\sigma_{e/8}$ behave quite similarly.

distributions is ~ 1.13 . I use a Kolmogorov-Smirnov (K-S) test to compare the two distributions. The K-S test shows that the probability that the two distributions are identical is 0.88. I also show the distribution for $\Delta\sigma_{e/8}(B+D)/\sigma_{e/8}(B)$ and $\Delta\sigma_e(B+D)/\sigma_e(B)$, which shows that the scatter in $\sigma_{e/8}(B+D)$ is slightly larger than in $\sigma_e(B+D)$. The K-S test now finds that the probability that both distributions are identical is only 0.41. Contamination from the disc increases $\Delta\sigma_{e/8}$ and $\Delta\sigma_e$ by factor of ~ 0.08 and ~ 0.075 , respectively. I therefore can conclude that σ_e measured within R_{eff} is a slightly better measure of the bulge velocity dispersion.

4.3.2 The Effect of Orientation

Bar formation increases the anisotropy of the bulge and of the bulge + disc, increasing $\Delta\sigma_e$. I plot $\Delta\sigma_e$ versus β_ϕ , β_z and β_t in Figure 4.8. The initial bulge + disc system has $-0.12 < \beta_t(B+D) < 0.05$, which increases by t_1 and continues to rise in most runs. In general $\Delta\sigma_e(B+D)$ correlates with anisotropy, with the correlation stronger with $\beta_z(B+D)$ and $\beta_t(B+D)$ than with $\beta_\phi(B+D)$.

Graham et al. (2011) argued that the orbital structure of the bar increases σ_e by as much as 10 – 40%, depending on the bar’s strength and orientation. In Figure 4.9 and 4.10 I show $\Delta\sigma_e$ averaged over PAs $\langle\sigma_e\rangle_{PA}$ and over inclinations $\langle\sigma_e\rangle_{inc}$, respectively. $\Delta\sigma_e$ is $\sim 13\%$ for bulge + disk and $\sim 6\%$ for the bulge. There is a clear decline in $\Delta\sigma_e$ from t_1 to t_2 , except in simulation 25, where the bar is still very weak at t_1 and becomes stronger at t_2 . The decline of $\Delta\sigma_e$ in the other simulations is due to the bar buckling between t_1 and t_2 , which decreases the anisotropy. $\Delta\sigma_e$ is greater for higher inclination. There is also a clear correlation between $\Delta\sigma_e$ and bar strength. This trend is different when I vary the PAs at fixed inclination. At PA = 0° (bar seen side-on) the scatter declines with increasing A_{Bar} , whereas at a PA $> 30^\circ$ the scatter increases with increasing A_{Bar} .

The scatter, $\Delta\sigma_e$, arising from different orientations is low compared to the

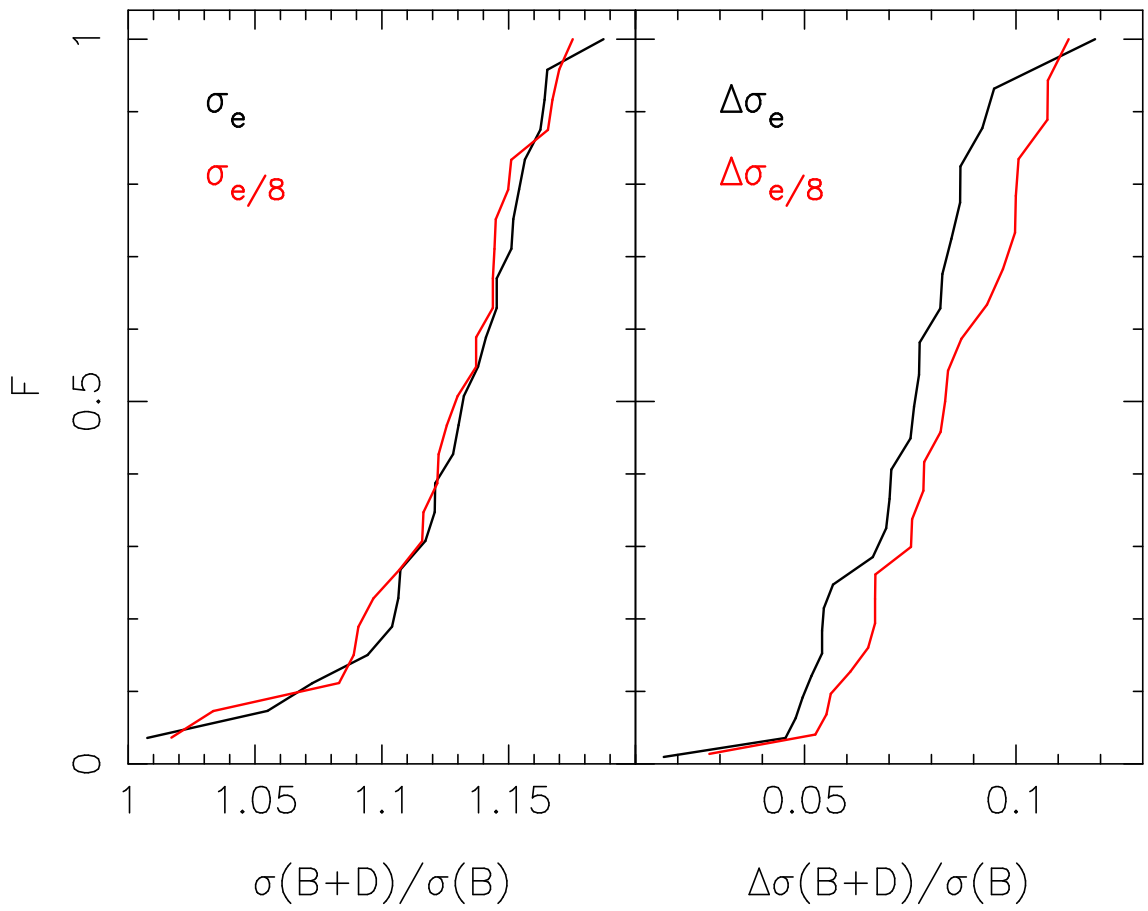


Figure 4.7: Left panel - The cumulative distribution of $\sigma_{e/8}(B + D)$ (red solid line) and $\sigma_e(B + D)$ (black solid line). Right panel - The cumulative distribution of $\Delta\sigma_{e/8}(B + D)$ and $\Delta\sigma_e(B + D)$.

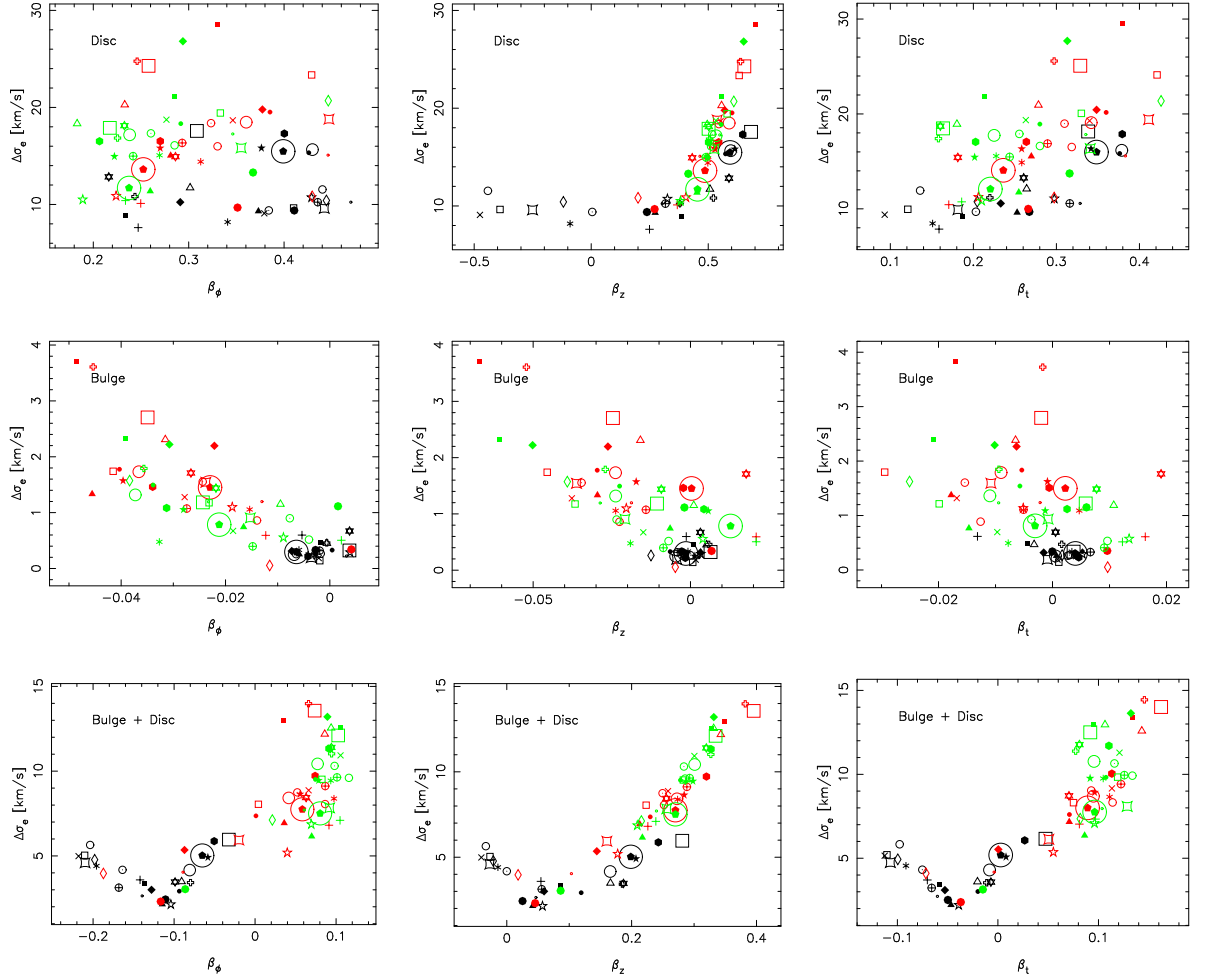


Figure 4.8: The scatter $\Delta\sigma_e$ at t_0 (black), t_1 (red) and at t_2 (green) versus anisotropy β_ϕ (left panels), β_z (middle panel) β_t in spherical coordinates for the disc (top), for the bulge (middle) and for the bulge + disc (bottom). The bulge + disc system shows a stronger correlation to β_ϕ , β_z and β_t than do the components separately.

changes in σ_e induced by the increase of mass during bar formation. Any offsets therefore cannot be explained by the orbit families of the bar, as proposed by Graham et al. (2011). Moreover, at best, orientation increases the scatter in σ_e but does not systematically increase it.

4.4 Evolution of the M_\bullet - σ_e relation

The changes in σ_e associated with bar formation would have consequences for the SMBH. If it is to remain on the $M_\bullet - \sigma_e$ relation, M_\bullet has to grow by a factor of

$$\Gamma_\bullet \equiv M_{\bullet,final}/M_{\bullet,init} = (\sigma_e/\sigma_{e0})^\beta . \quad (4.16)$$

In the simulations σ_e increases by a factor of ~ 1.4 . This implies that M_\bullet has to grow by a factor of ~ 4.2 , if the slope $\beta = 4.24$ (Gültekin et al., 2009b).

4.4.1 Zero-Point

If M_\bullet does not grow during bar formation, the increase of σ_e moves the SMBH in the $M_\bullet - \sigma_e$ plane. Following the procedure presented in Debattista et al. (*in prep.*), where they define the change in σ_e as $\bar{f} \equiv \langle \sigma_e/\sigma_{e0} \rangle$, I can write the $M_\bullet - \sigma_e$ relation assuming no M_\bullet growth after bar formation as

$$\log M_\bullet = \alpha + \beta \log \sigma_e - \beta \log \bar{f} . \quad (4.17)$$

The slope of the $M_\bullet - \sigma_e$ relation remains β , but the zero-point changes by

$$\Delta\alpha = -\beta \log \bar{f} . \quad (4.18)$$

Bar growth increases σ_e thus $\bar{f} > 1$ and the difference of the zero-point $\Delta\alpha < 0$. Therefore, the $M_\bullet - \sigma_e$ relation for barred galaxies is parallel to the $M_\bullet - \sigma_e$ relation of unbarred galaxies with an offset due to the smaller zero point. Here I assume that \bar{f} is uncorrelated with σ_e .

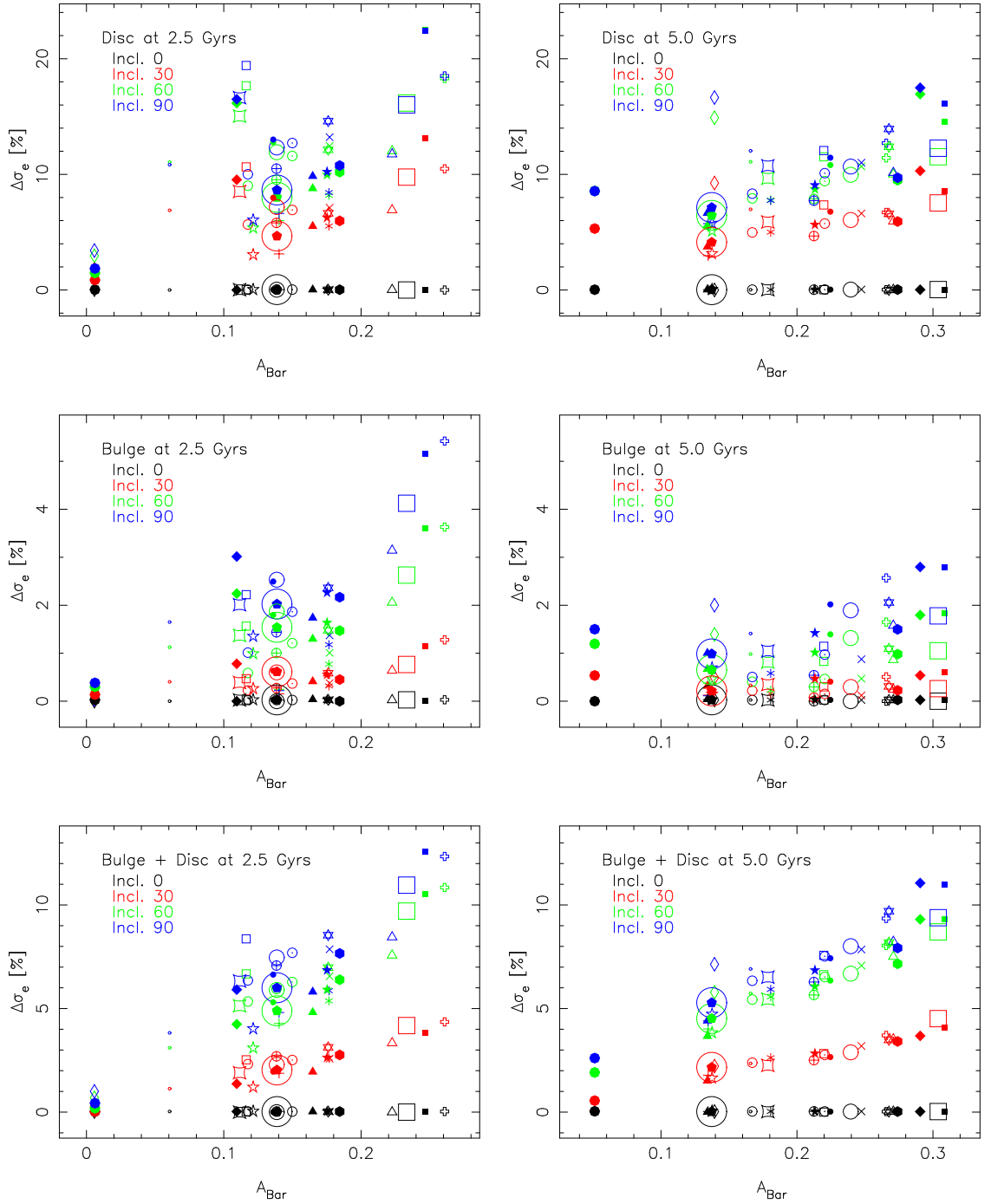


Figure 4.9: The scatter, $\Delta\sigma_e$, averaged over four different PAs at a fixed inclination versus bar amplitude. On the left I show $\Delta\sigma_e$ at t_1 and on the right at t_2 . From the top to the bottom, I show: $\Delta\sigma_e$ measured within R_{eff} of the disc, bulge and bulge + disc system, respectively.

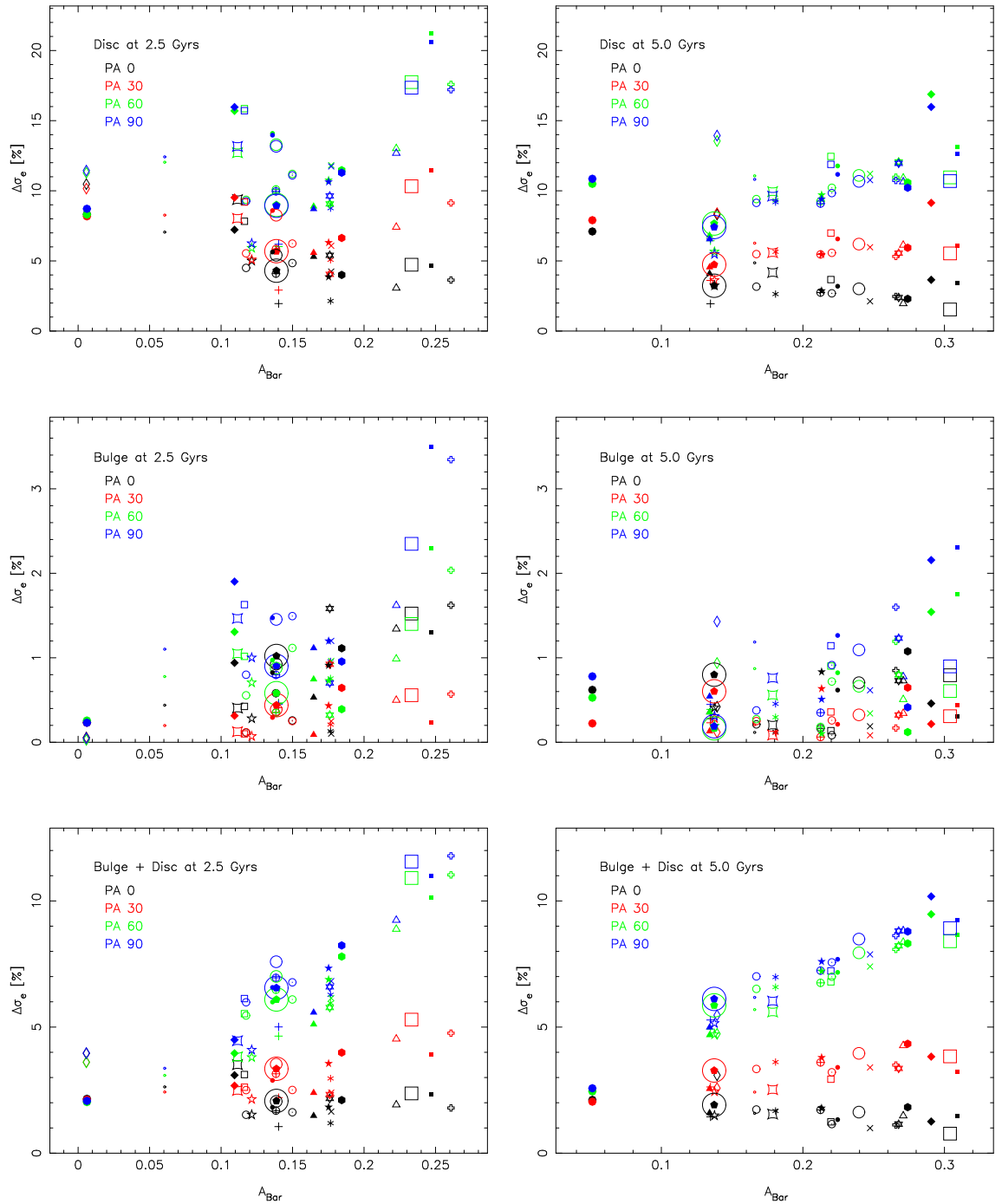


Figure 4.10: The scatter, $\Delta\sigma_e$, averaged over four different inclinations at a fixed PA versus bar amplitude. On the left I show $\Delta\sigma_e$ at t_1 and on the right at t_2 . From the top to the bottom, I show: $\Delta\sigma_e$ measured within R_{eff} of the disc, bulge and bulge + disc system, respectively.

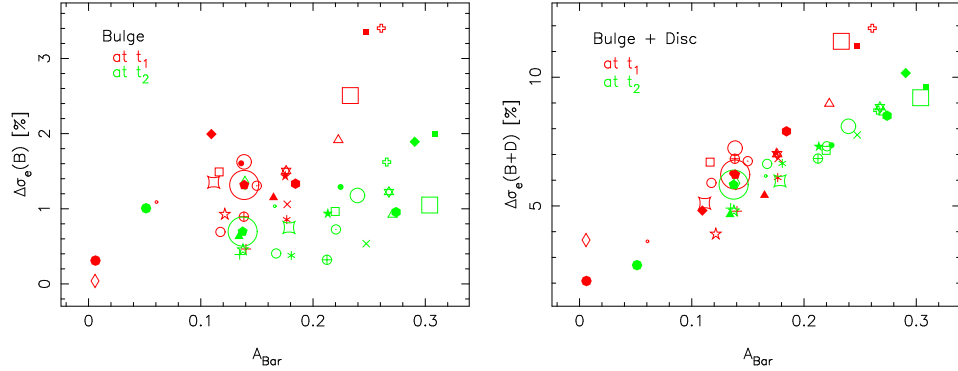


Figure 4.11: The scatter $\Delta\sigma_e$ averaged over all orientations versus bar amplitude. In the left column I show $\Delta\sigma_e(B)$ and in the right column $\Delta\sigma_e(B + D)$ at t_1 (green) and at t_2 (red). at t_2 .

I use the fitting method MPFITEXY¹, which uses the algorithm MPFIT (Markwardt, 2009) to obtain a linear regression by minimising

$$\chi^2 = \sum_{i=1}^N \frac{(y_i - \alpha - \beta x_i)^2}{\epsilon_{x_i}^2 + (\epsilon_{y_i}^2 + \epsilon_0^2)} \quad (4.19)$$

where ϵ_0 is the intrinsic scatter, which is determined such that the reduced $\tilde{\chi}^2 \lesssim 1$. The χ^2 estimator treats the M_\bullet and the σ_e values symmetrically. This guarantees that neither M_\bullet nor σ_e is the dependent variable in the relation (Tremaine et al., 2002). In Figure 4.12, I show the $M_\bullet - \sigma_e$ relation for my simulations by calculating M_\bullet via the $M_\bullet - \sigma_e$ relation for galaxies (Gültekin et al., 2009b), using σ_e at t_0 . I then fit the $M_\bullet - \sigma_e$ relation with σ_e at t_2 assuming that M_\bullet remains unchanged. I find a significant offset, with the largest offset being in the disc component and the smallest offset in the bulge. The results of the fits are presented in Table 4.2.

¹<http://purl.org/mike/mpfitexy>

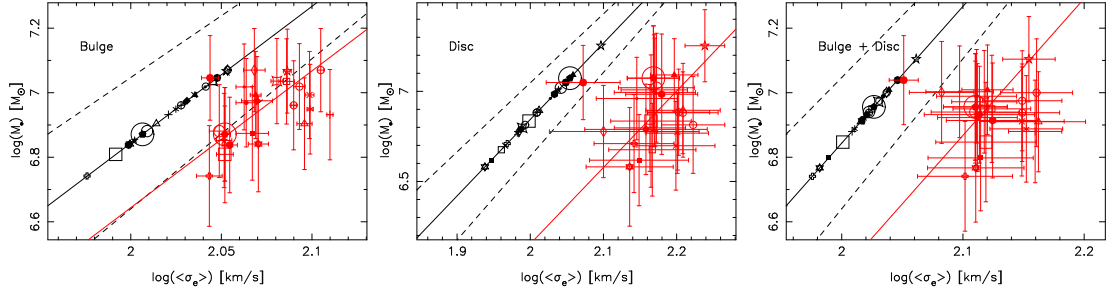


Figure 4.12: Using the known $M_{\bullet} - \sigma_e$ relation (solid black line) from Gültekin et al. (2009b), I show the initial σ_e and calculated M_{\bullet} (black symbols). The dashed lines show the 1σ uncertainty of the $M_{\bullet} - \sigma_e$ relation. Assuming that M_{\bullet} does not change, I plot σ_e at t_2 (red symbols). The red solid line shows a χ^2 fit to the values at t_2 assuming the same slope $\beta = 4.24$ as found by Gültekin et al. (2009b). I find, in all cases, a substantial offset from the $M_{\bullet} - \sigma_e$ relation. Note the different scales of the abscissa and ordinate.

Table 4.2: Fit results - using a χ^2 fit with a fixed slope $\beta = 4.24$ from Gültekin et al. (2009b) for classical bulges of unbarred disc galaxies. I calculate the offset via the difference between the zero-point of unbarred disc galaxies and the zero-point from the fit to the simulations.

Component	$\alpha \pm \Delta\alpha$	Offset [dex]
Bulge	7.92 ± 0.03	-0.20
Disc	7.43 ± 0.07	-0.69
Bulge + Disc	7.71 ± 0.04	-0.41

4.5 Comparison with observations

Evidence for an offset for barred galaxies has been given by Hu (2008); Graham (2008b); Gadotti & Kauffmann (2009) and Graham et al. (2011). I use the published data of 49 SMBH direct mass measurements to obtain the $M_{\bullet} - \sigma_e$ for classical bulges in unbarred galaxies and barred galaxies. In the sample of Gültekin et al. (2009b), I find 12 bulges in unbarred galaxies and 10 bulges in barred galaxies. I define bulges having a Sérsic index $n < 2$ as a pseudo bulge. Thus in the sample of bulges in unbarred galaxies, I have one pseudo bulge and 11 classical bulges (M31, M81, NGC 3115, NGC 3245, NGC 3585, NGC 3998, NGC 4026, NGC 4342, NGC 4564, NGC 4594, NGC 7457), while in the sample of bulges in barred galaxies, I find four pseudo bulges (NGC 1300, NGC 3384, NGC 7582, Circinus) and six classical bulges (NGC 1023, NGC 2787, NGC 3227, NGC 4258, NGC 4596, Milky Way). Using the same method as described in Section 4.4, I fit the $M_{\bullet} - \sigma_e$ relation for the classical bulges in unbarred galaxies. I obtain $(\alpha, \beta, \epsilon) = (8.38 \pm 0.07, 3.72 \pm 0.41, 0.11)$. I then fixed the slope to measure offsets and refit the $M_{\bullet} - \sigma_e$ relation for the classical bulges and for pseudo bulges in barred galaxies. I find, for the classical bulges, $(\alpha, \epsilon) = (7.98 \pm 0.18, 0.39)$ and for the pseudo bulges, $(\alpha, \epsilon) = (7.56 \pm 0.33, 0.58)$. Thus both types of bulges have an offset from the $M_{\bullet} - \sigma_e$ relation of unbarred galaxies, while the offset for pseudo bulges with $\Delta\alpha = -0.82$ dex are greater than for classical bulges with $\Delta\alpha = -0.4$ dex in barred galaxies. A similar offset of $\Delta\alpha = -0.5$ dex has been found by Graham et al. (2011) using a set of 64 M_{\bullet} in galaxies from which 20 bulges are in barred galaxies. Using Eqn. 4.18, this implies that SMBH in barred galaxies have $\Gamma_{\bullet} \sim 6.6$ in pseudo bulges and $\Gamma_{\bullet} \sim 2.5$ in classical bulges.

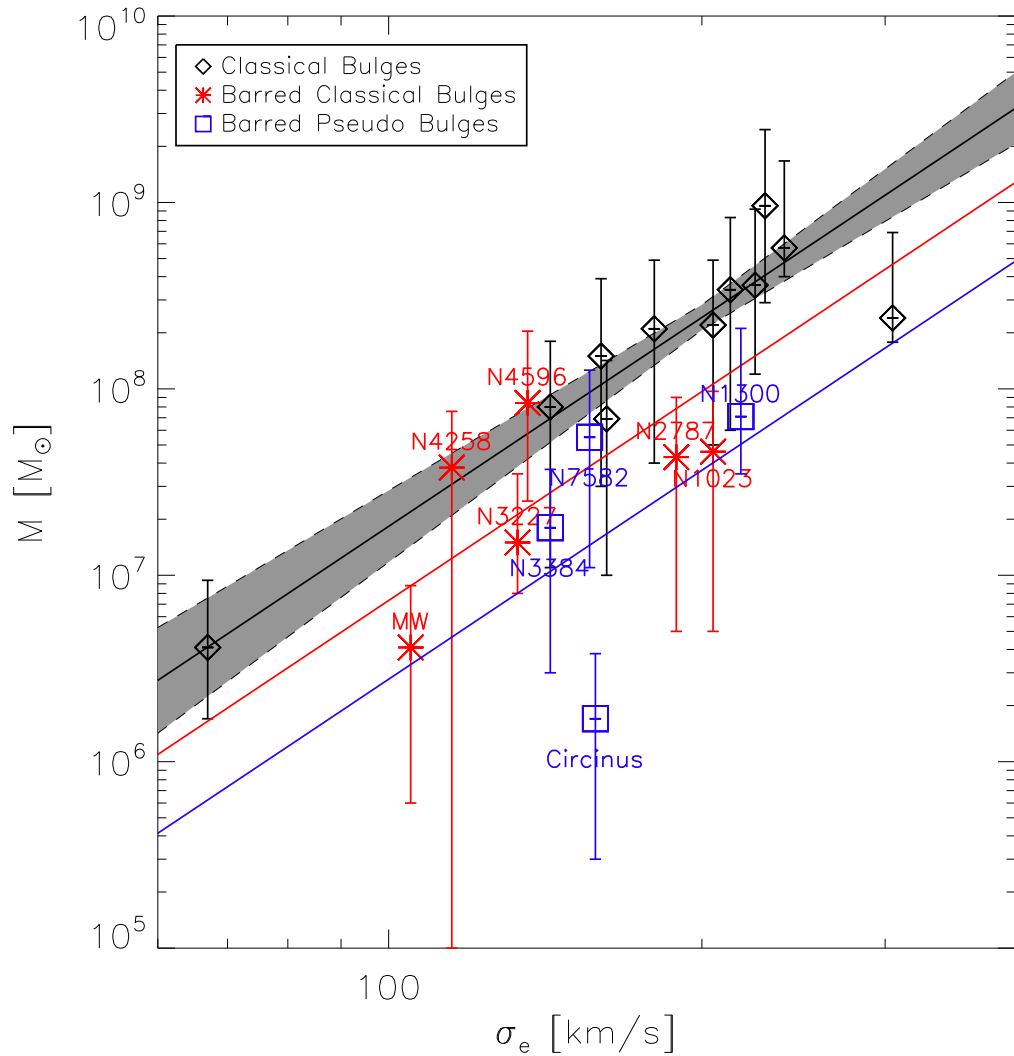


Figure 4.13: The $M_{\bullet} - \sigma_e$ relation for classical bulges in disc galaxies, classical and pseudo bulges in barred spiral galaxies from Gültekin et al. (2009b). The solid black line shows the linear regression of the classical bulges, while the dashed black lines show the 1σ uncertainty. The solid red and blue lines show a fit of the $M_{\bullet} - \sigma_e$ relation to the classical and pseudo bulges in barred galaxies with slope fixed to that for classical bulges in unbarred disc galaxies.

4.6 Discussion

4.6.1 Offset in the $M_{\bullet} - \sigma_e$ relation

I have analysed in detail the consequences of bar formation on the evolution of the aperture velocity dispersion σ_e of the bulge and bulge + disc system. Assuming that the initial supermassive black hole (SMBH) satisfies the $M_{\bullet} - \sigma_e$ relation, I have shown that if M_{\bullet} does not grow after bar formation, the increase in σ_e results in an offset from the $M_{\bullet} - \sigma_e$ relation. Graham (2008b) found that the scatter in the $M_{\bullet} - \sigma_e$ relation is reduced when bulges of barred galaxies are excluded and defined a $M_{\bullet} - \sigma_e$ relation of unbarred galaxies. Graham et al. (2011) found in a sample of 64 galaxies that the offset for bulges in barred galaxies is about -0.5 dex compared with the unbarred $M_{\bullet} - \sigma_e$ relation. He argued that this offset could be the result of different orientations of the bar, possibly enhancing σ_e of the bulge by 10 – 40% depending on the strength and orientation of the bar. I find that the scatter of σ_e in the bulge + disc caused by different orientations is $< 15\%$, but that the increase in σ_e caused by the increase in mass due to bar formation is able to explain the observed offset.

These results suggest that bars are not efficient at feeding the growth of SMBHs. However using *Hubble Space Telescope* STIS spectra to measure the upper limits of 105 SMBH masses, M_{\bullet} , in low-luminosity AGNs, Beifiori et al. (2009) did not find any offset of barred galaxies from the $M_{\bullet} - \sigma_e$ relation of unbarred galaxies. Likewise in a study of 76 active galaxies Xiao et al. (2011) also found that there is no discrepancy between barred and unbarred galaxies. While the latter sample has no information about the morphological type of the galaxies, the sample of Beifiori et al. (2009) contains 19 barred galaxies from which 6 galaxies are early-type galaxies. The sample of Graham et al. (2011) contains 20 barred galaxies of which 8 are early-type galaxies, but they do not distinguish between classical and

pseudo bulges. In the sample of Gültekin et al. (2009a) which I used in this paper, I have 6 classical barred galaxies from which 4 are early-type galaxies. The fact that samples which contain a significant fraction of early-type galaxies shows an offset of barred galaxies in the $M_{\bullet} - \sigma_e$ relation, while samples which consist mostly of late-type galaxies do not show this offset, suggests that bars are efficient at feeding SMBHs, but in the absence of gas in the host galaxy, the SMBH is unable to grow back on to the $M_{\bullet} - \sigma_e$ relation. Therefore, if the bar forms in an early-type galaxy, M_{\bullet} will have an offset from the $M_{\bullet} - \sigma_e$ relation of unbarred galaxies.

4.7 Summary

I have studied the consequences of bar formation on the $M_{\bullet} - \sigma_e$ relation of SMBHs in the classical bulges of spiral galaxies. I have used a set of 25 disc galaxy simulations, which consist of, by construction, classical bulges.

The formation of a bar increases the mass density within the central region, alters the kinematics of the disc and bulge and varies the structural properties of the bulge. Both the half mass radius of the bulge and the Sérsic index decrease in most simulations. While anisotropy increases, the aperture velocity dispersion, σ_e , rises everywhere. The mean change in $\langle \sigma_e / \sigma_{e0} \rangle$ shows a strong correlation with the change in the mass ratio of the bulge + disc $M_{B+D} / M_{B+D,init}$. The increase of $\langle \sigma_e / \sigma_{e0} \rangle$ is about a factor of 1.4.

The scatter, $\Delta\sigma_e$, is measured as the root-mean-square of σ_e by averaging over four different position angle (PA) at four inclinations. I find that $\Delta\sigma_e$ correlates with the bar amplitude, A_{Bar} but there is an even stronger correlation with anisotropy, β_{ϕ} , β_z and β_t . $\Delta\sigma_e$ is largest in the disc and smallest in the bulge. In the bulge + disc $\Delta\sigma_e$ is $\sim 15\%$, when the bar is seen edge-on and end-on. Thus, $\Delta\sigma_e$ is smaller than the mean change in σ_e caused by the increase in mass due to bar growth.

While σ_e in the disc does not correlate with the σ_e of the bulge, σ_e of the bulge

+ disc does correlate. If I measure $\sigma_{e/8}$, which is the velocity dispersion measured within the aperture of $R_{\text{eff}}/8$, I find a similar correlation. In the edge-on view, σ_e and $\sigma_{e/8}$ are about a factor of ~ 1.3 larger in the bulge + disc than in the bulge.

The influence of the disc within R_{eff} and $R_{\text{eff}}/8$ is still significant and I find, for both, a similar offset with a factor of ~ 1.13 from their distributions compared to σ_e and $\sigma_{e/8}$ of the bulge. Both σ_e and $\sigma_{e/8}$ follow very similar distributions with a probability of 0.88 in a Kolmogorov-Smirnov test.

The increase of σ_e by a factor of ~ 1.4 implies that the mass of the SMBH, M_\bullet , needs to grow by a factor of ~ 4.2 , if it would remain on the $M_\bullet - \sigma_e$ relation. However, if the M_\bullet does not grow, the SMBH has an offset from the usual $M_\bullet - \sigma_e$ relation. I use the $M_\bullet - \sigma_e$ relation with the most recent values (Gültekin et al., 2009b) to calculate M_\bullet from σ_e at t_0 . Fitting the $M_\bullet - \sigma_e$ relation with the same M_\bullet but σ_e at t_2 with the same slope. I find a significant offset in the simulations from the $M_\bullet - \sigma_e$ relation. In comparison to the simulations, I use the sample of 49 galaxies (Gültekin et al., 2009b) and fit the $M_\bullet - \sigma_e$ relation only for classical bulges in unbarred galaxies. I find a $M_\bullet - \sigma_e$ relation for these galaxies with zero-point, slope and intrinsic scatter of $(\alpha, \beta, \epsilon) = (8.38 \pm 0.07, 3.72 \pm 0.41, 0.11)$, respectively. I then refit the $M_\bullet - \sigma_e$ relation using the same slope to measure the offset of classical bulges and pseudo bulges in barred galaxies. The offset from the $M_\bullet - \sigma_e$ relation is smaller for the classical bulges than for the pseudo bulges, but the offset is significant and larger than 1σ level of uncertainty. Therefore, the offset of bulges in barred galaxies from the $M_\bullet - \sigma_e$ relation of unbarred galaxies could be the result of the increase of mass due to bar formation in the disc of the galaxies.

Chapter 5

Summary of Conclusions and Future Prospects

In my thesis I have studied the evolution and formation of nuclei in galaxies from two different aspects. I have shown that nuclear clusters (NCs), as the visible proxies of supermassive black holes (SMBHs), offer remarkable insights into the formation history of the central regions of galaxies. I achieved full usage of the two-dimensional data of the NCs in NGC 4244 and M33 by modelling the observations with the solutions of the Jeans equations with an oblate velocity ellipsoid (JAM software described in Cappellari, 2008). While M33 is inclined by 49° (Corbelli & Schneider, 1997), and, therefore, it is not possible to determine its anisotropy, I find that the NC in edge-on galaxy NGC 4244 is nearly isotropic with $\beta_z = -0.2 \pm 0.1$. Both NCs are rapidly rotating. The merger of star clusters (SCs) produce a variety of observed properties including densities, structural scaling relations and even rapid rotation. The shape and the presence of young nuclear cluster disks (NCD) can also be achieved by the multiple accretion of *young star clusters* onto a NC. Nonetheless, difficulties remain such as that the line-of-sight velocity profile, $V(x)$, is more slowly rising and that the second order kinematic moment, $V_{\text{rms}}(x) = \sqrt{V(x)^2 + \sigma(x)^2}$, are too centrally peaked to match observations. The latter can be remedied by the

accretion of SCs onto a pre-existing NCD. I imitate the formation of a NCD out of the accretion of gas by introducing a pre-existing NCD of stars. These results suggest that the formation of NCs in late-type spiral galaxies cannot be purely stellar dynamical mergers and that gas dissipation is required. In comparison with the NC in NGC 4244, gas dissipation is needed for at least 50% of its total mass. However, the negative anisotropy found in NGC 4244 requires the direct accretion of stars with at least 10% of its total mass, since gas dissipation and in-situ star formation leads to positive anisotropy. These results show that these detailed observables can be used to constrain the formation scenario of NCs. More high resolved integral field data of the kinematics of NCs are essential for further progress. Further constraints on NC formation could also be achieved by studying the central environment in galaxies. Agarwal & Milosavljević (2011) have shown that not only the merger of an empirical SC population lead to consistent NC masses, but also that as result of the merger of SCs, the remnant NC is surrounded by an extended excess over the underlying galaxy profile. They suggested that this excess could be related to the pseudo bulge phenomenon in disc galaxies. In my simulations, the best fitting NCs from the accretion of SCs onto a pre-existing NCD consist of 95% of the total mass of accreted SCs. In these simulations, the mass of the extended excess is only a small fraction, but it is distributed in an extended disc-like structure. In the spiral galaxy NGC 4698, and the low luminosity elliptical galaxies NGC 4458 and NGC 4478, nuclear stellar discs have been found (Bertola et al., 1999; Morelli et al., 2004). These nuclear stellar discs, which are more extended than young NCDs in NCs, could be related by NC formation. However, only in NGC 4458 a NC has been found (Ferrarese et al., 2006). Thus, more detailed observations to study the stellar populations of nuclear stellar discs and integral field data to study the kinematics could bring further insights, if these nuclear stellar discs are related with NC formation or central massive objects in general. The simulations can provide

further structural and kinematical constraints.

In elliptical galaxies, fine structures such as shells and ripples have been found in the outer parts, and these structures are believed to be formed by tidal interactions due to galaxy mergers (Sikkema et al., 2007; Canalizo et al., 2007). These structures can, in general, be detected even a few Gyrs after the last major merger event (Schweizer & Seitzer, 1992). When NCs in dwarf elliptical galaxies form mainly through the merger of SCs (Lotz et al., 2001, 2004), besides a boxy isophotal shape, centrally peaked V_{rms} fields, and radially biased anisotropy, these kinds of shell structures might be observable. One simulation, of eight massive SCs within the central region of a bulge, shows that shell structures survive over 100 Myrs and maybe even longer. Thus, even in late-type spiral galaxies, if the anisotropy is observed to be negative, these shells could be observable. When the simulations predict that these nuclear shells are dense enough to be observable, that could be another constraint of stellar mergers in NCs.

The Milky Way galaxy is one of the galaxies containing both a SMBH (Gillessen et al., 2009) and a ~ 10 times more massive NC (Schödel et al., 2009). However, the nature of the interplay between SMBHs and NCs and their relation is unknown. Based on the scaling relations of CMOs (Ferrarese et al., 2006; Wehner & Harris, 2006; Rossa et al., 2006; Graham et al., 2011) and the coexistence of NCs and SMBHs in galaxies (Seth et al., 2008a; Graham & Spitler, 2009), there exist two possibilities of their relation: Either the formation of SMBHs could be directly linked to the formation of NCs, or NCs and SMBHs could be formed by processes that scale similarly with galaxy mass, but are otherwise unrelated. There is no clear evidence between central star formation and AGN activity, but the accretion of SCs could enhance the growth of the SMBH by accreting intermediate mass black holes (Noyola et al., 2008, 2010; van der Marel & Anderson, 2010). Furthermore, the accretion of SCs could enhance the refilling of the orbits of stars in the loss-cone (Merritt &

Wang, 2005), which could increase the rate of merging of intermediate mass black holes. However the agglomeration of an intermediate mass black holes could also lead to a recoil of a SMBH after their merger. This would have a strong effect on the surrounding NC. If the SMBH is massive enough, it could lead to the disruption of the NC, due to the drastic changes in the gravitational potential. This is a possible explanation for the finding of the ACS Virgo Cluster Survey, that about 66 to 88% of low and intermediate luminosity early-type galaxies harbour a NC (Côté et al., 2006). The simulations presented in this thesis might be able to give further insights into this aspects.

In my thesis, I have shown that to match the observed kinematic properties of the NC in NGC 4244 gas dissipation is needed for at least 50% of its total mass. One proposed mechanisms for driving gas towards the galactic centres is the action of instabilities such as nuclear spirals or nested bars (Shlosman & Begelman, 1989; Schinnerer et al., 2003; Maciejewski et al., 2002; Schinnerer et al., 2008). Erwin & Sparke (2002) carefully compiled statistics for early-type optically barred galaxies from images by both the *WIYN telescope* and the *Hubble Space Telescope* and concluded that at least one-quarter of them are double-barred. Debattista & Shen (2007) have shown that the formation of a long-lived secondary bar can evolve spontaneously in stellar systems through rotating pseudo bulges. Using similar high resolved initial conditions as described in this thesis, smoothed particle hydrodynamics simulations could provide new insight into the formation of NCs. They will allow to study the fuelling rate into the central region of the galaxy as well as to study the kinematics of the formed systems.

On the other hand, I have studied the kinematical changes in bar forming galaxies using a set of 25 spiral galaxy simulations. In these simulations I have investigated the evolution of the $M_{\bullet} - \sigma_e$ relation (Gebhardt et al., 2000a; Ferrarese & Merritt, 2000; Tremaine et al., 2002; Ferrarese & Ford, 2005) between the SMBH mass, M_{\bullet} ,

and the aperture velocity dispersion of stars, σ_e , in the galaxy. Observations have indicated that $M_\bullet - \sigma_e$ relation of bulges in barred galaxies seemed to be different of the $M_\bullet - \sigma_e$ relation of unbarred galaxies (Hu, 2008; Gadotti & Kauffmann, 2009). Graham et al. (2011) find an offset of 0.5 dex of barred galaxies from the $M_\bullet - \sigma_e$ relation of unbarred galaxies. While Graham et al. (2011) argued that the increase in σ_e , which causes the offset of SMBHs in barred galaxies, could be explained by the projection of the orbital structure of stars in the bar, I find that the scatter, $\Delta\sigma_e$ is less than 15% due to different orientations. Instead, the increase in σ_e strongly correlates with the relative changes in mass in the galaxy and with the anisotropy of the galaxy. The alteration of σ_e in the bulge is about a factor of $\sim 40\%$, which implies that M_\bullet needs to grow by a factor of 4.2, so that it would remain on the $M_\bullet - \sigma_e$ relation. If the opposite is the case, and the M_\bullet does not grow, the SMBH moves away from the $M_\bullet - \sigma_e$ relation of unbarred galaxies. I find a significant offset from the $M_\bullet - \sigma_e$ relation in the simulations. In a sample of classical bulges and pseudo bulges in observed barred and unbarred galaxies (Gültekin et al., 2009b), I also find a significant offset of barred galaxies. The offset from the $M_\bullet - \sigma_e$ relation is smaller for the classical bulges than for the pseudo bulges, but the offset is larger than the 1σ level of uncertainty. While these simulations are collisionless N -body simulations, the formerly described smoothed particle hydrodynamical simulations of double barred galaxies would also shed light on the feeding processes of SMBHs in galaxies. Fuelling processes in spiral galaxies become more important at lower redshifts, because in the hierarchical picture of galaxy formation the merger rate of galaxies decreases significantly at lower redshifts. Thus, secular processes in disc galaxies become more important and are the drivers to fuel AGN and star formation in the central region of galaxies in the local universe (Schawinski et al., 2011). Bar formation in the stellar disc leads to the redistribution of angular momentum and not only to an increase in stellar mass in the central region, but also an increase

in gaseous mass (Sakamoto et al., 1999; Jogee et al., 2005). While both processes influence the kinematics of the bulge, which cause an offset of SMBHs in the $M_{\bullet} - \sigma_e$ relation of unbarred galaxies, the accretion of gas could feed the SMBH. Therefore, the accretion of gas in the central region can increase M_{\bullet} and if sufficient, the SMBH can be brought back onto the $M_{\bullet} - \sigma_e$ relation. The formerly described smoothed particle hydrodynamics simulations of nested bars could also provide new insights into these processes and how different the timescales of these processes are.

In conclusion the fuelling processes of SMBHs and NCs in spiral galaxies will also shed light on the evolution of SMBH seeds, because SMBHs and NCs in bulges of dwarf galaxies are on the lower mass end of central massive objects. Thus, these processes might provide deeper insights in the evolution of SMBH seeds formed in the early times of the Universe.

Bibliography

Abadi, M. G., Navarro, J. F., Steinmetz, M., & Eke, V. R. 2003, *ApJ*, 597, 21

Abel, T., Bryan, G. L., & Norman, M. L. 2000, *ApJ*, 540, 39

Adams, F. C., Graff, D. S., Mbonye, M., & Richstone, D. O. 2003, *ApJ*, 591, 125

Adams, F. C., Graff, D. S., & Richstone, D. O. 2001, *ApJ*, 551, L31

Agarwal, M., & Milosavljević, M. 2011, *ApJ*, 729, 35

Andersen, D. R., Walcher, C. J., Böker, T., Ho, L. C., van der Marel, R. P., Rix, H.-W., & Shields, J. C. 2008, *ApJ*, 688, 990

Andredakis, Y. C. 1998, *MNRAS*, 295, 725

Araki, S. 1987, *AJ*, 94, 99

Athanassoula, E. 1992, *MNRAS*, 259, 328

Athanassoula, E. 2005, *MNRAS*, 358, 1477

Avila-Reese, V., Carrillo, A., Valenzuela, O., & Klypin, A. 2005, *MNRAS*, 361, 997

Baes, M., Buyle, P., Hau, G. K. T., & Dejonghe, H. 2003, *MNRAS*, 341, L44

Bastian, N., Saglia, R. P., Goudfrooij, P., Kissler-Patig, M., Maraston, C., Schweizer, F., & Zoccali, M. 2006, *A&A*, 448, 881

-
- Baugh, C. M., Cole, S., & Frenk, C. S. 1996, MNRAS, 283, 1361
- Begelman, M. C. 2010, MNRAS, 402, 673
- Begelman, M. C., & Rees, M. J. 1978, MNRAS, 185, 847
- Begelman, M. C., Rossi, E. M., & Armitage, P. J. 2008, MNRAS, 387, 1649
- Begelman, M. C., Volonteri, M., & Rees, M. J. 2006, MNRAS, 370, 289
- Beifiori, A., Sarzi, M., Corsini, E. M., Dalla Bontà, E., Pizzella, A., Coccato, L., & Bertola, F. 2009, ApJ, 692, 856
- Bekki, K. 2007, Publications of the Astronomical Society of Australia, 24, 77
- Bekki, K., Couch, W. J., Drinkwater, M. J., & Shioya, Y. 2004, ApJ, 610, L13
- Bekki, K., Couch, W. J., & Shioya, Y. 2006, ApJ, 642, L133
- Bender, R. 1988, A&A, 193, L7
- Bender, R., Burstein, D., & Faber, S. M. 1992, ApJ, 399, 462
- Bertola, F., Corsini, E. M., Vega Beltrán, J. C., Pizzella, A., Sarzi, M., Cappellari, M., & Funes, J. G. 1999, ApJ, 519, L127
- Binney, J. 1978, MNRAS, 183, 501
- Binney, J. 2005, MNRAS, 363, 937
- Binney, J., & Mamon, G. A. 1982, MNRAS, 200, 361
- Binney, J., & Tremaine, S. 2008, Galactic Dynamics: Second Edition (Galactic Dynamics: Second Edition, by James Binney and Scott Tremaine. ISBN 978-0-691-13026-2 (HB). Published by Princeton University Press, Princeton, NJ USA, 2008.)

- Binney, J. J., Davies, R. L., & Illingworth, G. D. 1990, *ApJ*, 361, 78
- Blandford, R. D., & McKee, C. F. 1982, *ApJ*, 255, 419
- Blumenthal, G. R., Faber, S. M., Primack, J. R., & Rees, M. J. 1984, *Nature*, 311, 517
- Böker, T., Laine, S., van der Marel, R. P., Sarzi, M., Rix, H.-W., Ho, L. C., & Shields, J. C. 2002, *AJ*, 123, 1389
- Böker, T., et al. 2004, in *Astronomical Society of the Pacific Conference Series*, Vol. 322, *The Formation and Evolution of Massive Young Star Clusters*, ed. H. J. G. L. M. Lamers, L. J. Smith, & A. Nota, 39
- Bond, J. R., Arnett, W. D., & Carr, B. J. 1984, *ApJ*, 280, 825
- Bournaud, F., Jog, C. J., & Combes, F. 2007, *A&A*, 476, 1179
- Bromm, V., Coppi, P. S., & Larson, R. B. 2002, *ApJ*, 564, 23
- Bromm, V., & Loeb, A. 2003, *ApJ*, 596, 34
- Brook, C. B., et al. 2010, *ArXiv e-prints*
- Brooks, A. M., et al. 2011, *ApJ*, 728, 51
- Bureau, M., & Athanassoula, E. 1999, *ApJ*, 522, 686
- Burkert, A., & Naab, T. 2005, *MNRAS*, 363, 597
- Burkert, A., & Silk, J. 2001, *ApJ*, 554, L151
- Canalizo, G., Bennert, N., Jungwiert, B., Stockton, A., Schweizer, F., Lacy, M., & Peng, C. 2007, *ApJ*, 669, 801
- Cappellari, M. 2002, *MNRAS*, 333, 400

- Cappellari, M. 2008, MNRAS, 390, 71
- Cappellari, M., & Emsellem, E. 2004, PASP, 116, 138
- Cappellari, M., et al. 2007, MNRAS, 379, 418
- Cappellari, M., et al. 2011, MNRAS, 269
- Capuzzo-Dolcetta, R., & Miocchi, P. 2008a, ApJ, 681, 1136
- Capuzzo-Dolcetta, R., & Miocchi, P. 2008b, MNRAS, 388, L69
- Carollo, C. M., Stiavelli, M., de Zeeuw, P. T., & Mack, J. 1997, AJ, 114, 2366
- Carollo, C. M., Stiavelli, M., & Mack, J. 1998, AJ, 116, 68
- Carollo, C. M., Stiavelli, M., Seigar, M., de Zeeuw, P. T., & Dejonghe, H. 2002, AJ, 123, 159
- Chandrasekhar, S. 1943, ApJ, 97, 255
- Chokshi, A., & Turner, E. L. 1992, MNRAS, 259, 421
- Ciotti, L. 1991, A&A, 249, 99
- Clark, P. C., Glover, S. C. O., & Klessen, R. S. 2008, ApJ, 672, 757
- Combes, F. 2003, in *Astronomical Society of the Pacific Conference Series*, Vol. 290, *Active Galactic Nuclei: From Central Engine to Host Galaxy*, ed. S. Collin, F. Combes, & I. Shlosman, 411
- Combes, F. 2005, ArXiv Astrophysics e-prints
- Combes, F., Debbasch, F., Friedli, D., & Pfenniger, D. 1990, A&A, 233, 82
- Combes, F., & Sanders, R. H. 1981, A&A, 96, 164
- Contopoulos, G., & Papayannopoulos, T. 1980, A&A, 92, 33

- Corbelli, E., & Schneider, S. E. 1997, *ApJ*, 479, 244
- Côté, P., et al. 2006, *ApJS*, 165, 57
- Courteau, S., de Jong, R. S., & Broeils, A. H. 1996, *ApJ*, 457, L73
- Cox, T. J., Dutta, S. N., Di Matteo, T., Hernquist, L., Hopkins, P. F., Robertson, B., & Springel, V. 2006, *ApJ*, 650, 791
- Davies, R. L., & Illingworth, G. 1983, *ApJ*, 266, 516
- Debattista, V. P., Carollo, C. M., Mayer, L., & Moore, B. 2004, *ApJ*, 604, L93
- Debattista, V. P., Mayer, L., Carollo, C. M., Moore, B., Wadsley, J., & Quinn, T. 2006a, *ApJ*, 645, 209
- Debattista, V. P., Mayer, L., Carollo, C. M., Moore, B., Wadsley, J., & Quinn, T. 2006b, *ApJ*, 645, 209
- Debattista, V. P., Moore, B., Quinn, T., Kazantzidis, S., Maas, R., Mayer, L., Read, J., & Stadel, J. 2008, *ApJ*, 681, 1076
- Debattista, V. P., & Sellwood, J. A. 2000, *ApJ*, 543, 704
- Debattista, V. P., & Shen, J. 2007, *ApJ*, 654, L127
- Dehnen, W. 2005, *MNRAS*, 360, 892
- Devecchi, B., & Volonteri, M. 2009, *ApJ*, 694, 302
- Di Matteo, T., Springel, V., & Hernquist, L. 2005, *Nature*, 433, 604
- Drory, N., & Fisher, D. B. 2007, *ApJ*, 664, 640
- Dubinski, J. 1996, *New Astronomy*, 1, 133
- Ebisuzaki, T., et al. 2001, *ApJ*, 562, L19

-
- Efstathiou, G., Frenk, C. S., White, S. D. M., & Davis, M. 1988, *MNRAS*, 235, 715
- Eggen, O. J., & Sandage, A. R. 1962, *ApJ*, 136, 735
- Eisenstein, D. J., & Loeb, A. 1995, *ApJ*, 443, 11
- Eliche-Moral, M. C., Balcells, M., Aguerri, J. A. L., & González-García, A. C. 2006, *A&A*, 457, 91
- Elmegreen, B. G., Elmegreen, D. M., & Hirst, A. C. 2004, *ApJ*, 612, 191
- Emsellem, E., et al. 2011, ArXiv e-prints
- Emsellem, E., Monnet, G., & Bacon, R. 1994, *A&A*, 285, 723
- Emsellem, E., & van de Ven, G. 2008, *ApJ*, 674, 653
- Erwin, P., & Sparke, L. S. 2002, *AJ*, 124, 65
- F. Palla, H. Zinnecker, A. Maeder, & G. Meynet, ed. 2002, *Physics of star formation in galaxies*
- Fall, S. M., & Efstathiou, G. 1980, *MNRAS*, 193, 189
- Ferrarese, L. 2002, *ApJ*, 578, 90
- Ferrarese, L., et al. 2006, *ApJ*, 644, L21
- Ferrarese, L., & Ford, H. 2005, *Space Sci. Rev.*, 116, 523
- Ferrarese, L., & Merritt, D. 2000, *ApJ*, 539, L9
- Figer, D. F., McLean, I. S., & Morris, M. 1999, *ApJ*, 514, 202
- Figer, D. F., et al. 2002, *ApJ*, 581, 258
- 1992, *Accretion power in astrophysics.*, ed. Frank, J., King, A., & Raine, D.

- Franx, M., Illingworth, G., & de Zeeuw, T. 1991, *ApJ*, 383, 112
- Freitag, M., Rasio, F. A., & Baumgardt, H. 2006, *MNRAS*, 368, 121
- Frenk, C. S., White, S. D. M., Davis, M., & Efstathiou, G. 1988, *ApJ*, 327, 507
- Frenk, C. S., White, S. D. M., Efstathiou, G., & Davis, M. 1985, *Nature*, 317, 595
- Friedli, D., & Benz, W. 1995, *A&A*, 301, 649
- Fryer, C. L., Woosley, S. E., & Heger, A. 2001, *ApJ*, 550, 372
- Gadotti, D. A., & Kauffmann, G. 2009, *MNRAS*, 399, 621
- Gao, L., Yoshida, N., Abel, T., Frenk, C. S., Jenkins, A., & Springel, V. 2007, *MNRAS*, 378, 449
- Gebhardt, K. 1994, Ph.D. thesis, Rutgers - The State Univ.
- Gebhardt, K., et al. 2000a, *ApJ*, 539, L13
- Gebhardt, K., Pryor, C., O'Connell, R. D., Williams, T. B., & Hesser, J. E. 2000b, *AJ*, 119, 1268
- Gebhardt, K., Pryor, C., Williams, T. B., & Hesser, J. E. 1995, *AJ*, 110, 1699
- Gebhardt, K., Rich, R. M., & Ho, L. C. 2005, *ApJ*, 634, 1093
- Gebhardt, K., et al. 2003, *ApJ*, 583, 92
- Geha, M., Guhathakurta, P., & van der Marel, R. P. 2002, *AJ*, 124, 3073
- Gerssen, J., van der Marel, R. P., Gebhardt, K., Guhathakurta, P., Peterson, R. C., & Pryor, C. 2002, *AJ*, 124, 3270
- Gerssen, J., van der Marel, R. P., Gebhardt, K., Guhathakurta, P., Peterson, R. C., & Pryor, C. 2003, *AJ*, 125, 376

-
- Ghez, A. M., Salim, S., Hornstein, S. D., Tanner, A., Lu, J. R., Morris, M., Becklin, E. E., & Duchêne, G. 2005, *ApJ*, 620, 744
- Gillessen, S., Eisenhauer, F., Fritz, T. K., Bartko, H., Dodds-Eden, K., Pfuhl, O., Ott, T., & Genzel, R. 2009, *ApJ*, 707, L114
- Goerdt, T., Moore, B., Kazantzidis, S., Kaufmann, T., Macciò, A. V., & Stadel, J. 2008, *MNRAS*, 385, 2136
- Goerdt, T., Moore, B., Read, J. I., & Stadel, J. 2010, *ApJ*, 725, 1707
- Goldreich, P., & Tremaine, S. 1978, *ApJ*, 222, 850
- Goldreich, P., & Tremaine, S. 1979, *ApJ*, 233, 857
- Governato, F., et al. 2009, ArXiv e-prints
- Governato, F., et al. 2004, *ApJ*, 607, 688
- Graham, A. W. 2008a, *ApJ*, 680, 143
- Graham, A. W. 2008b, *PASA*, 25, 167
- Graham, A. W., & Driver, S. P. 2007, *MNRAS*, 380, L15
- Graham, A. W., & Li, I. 2009, *ApJ*, 698, 812
- Graham, A. W., Onken, C. A., Athanassoula, E., & Combes, F. 2011, *MNRAS*, 48
- Graham, A. W., & Spitler, L. R. 2009, *MNRAS*, 397, 2148
- Greene, J. E., et al. 2010, ArXiv e-prints
- Greif, T. H., Johnson, J. L., Klessen, R. S., & Bromm, V. 2008, *MNRAS*, 387, 1021
- Gültekin, K., et al. 2009a, *ApJ*, 695, 1577
- Gültekin, K., et al. 2009b, *ApJ*, 698, 198

Gürkan, M. A., Fregeau, J. M., & Rasio, F. A. 2006, *ApJ*, 640, L39

Gürkan, M. A., Freitag, M., & Rasio, F. A. 2004, *ApJ*, 604, 632

Haehnelt, M. G., & Rees, M. J. 1993, *MNRAS*, 263, 168

Haiman, Z. 2004, *ApJ*, 613, 36

Häring, N., & Rix, H. 2004, *ApJ*, 604, L89

Harris, W. E. 1996, *AJ*, 112, 1487

Hernquist, L. 1990, *ApJ*, 356, 359

Hinshaw, G., et al. 2009, *ApJS*, 180, 225

Hohl, F. 1971, *ApJ*, 168, 343

Hu, J. 2008, *MNRAS*, 386, 2242

Hubble, E. P. 1926, *ApJ*, 64, 321

1936, *Realm of the Nebulae*, ed. Hubble, E. P.

Illingworth, G. 1977, *ApJ*, 218, L43

Jahnke, K., & Maccio, A. 2010, *ArXiv e-prints*

Jedrzejewski, R. I. 1987, *MNRAS*, 226, 747

Jogee, S., et al. 2004, *ApJ*, 615, L105

Jogee, S., Scoville, N., & Kenney, J. D. P. 2005, *ApJ*, 630, 837

Johansson, P. H., Naab, T., & Burkert, A. 2009, *ApJ*, 690, 802

Johnson, J. L., & Bromm, V. 2007, *MNRAS*, 374, 1557

- Jones, T. A., Swinbank, A. M., Ellis, R. S., Richard, J., & Stark, D. P. 2010, MNRAS, 404, 1247
- Kalnajs, A. J. 1973, ApJ, 180, 1023
- Katz, N. 1991, ApJ, 368, 325
- Katz, N., Hernquist, L., & Weinberg, D. H. 1992, ApJ, 399, L109
- Kauffmann, G., White, S. D. M., & Guiderdoni, B. 1993, MNRAS, 264, 201
- Kazantzidis, S., et al. 2005, ApJ, 623, L67
- Khochfar, S., & Burkert, A. 2005, MNRAS, 359, 1379
- King, A. 2003, ApJ, 596, L27
- King, I. 1962, AJ, 67, 471
- Kormendy, J., & Bender, R. 1996, ApJ, 464, L119
- Kormendy, J., & Djorgovski, S. 1989, ARA&A, 27, 235
- Kormendy, J., & Illingworth, G. 1982, ApJ, 256, 460
- Kormendy, J., & Kennicutt, R. C., Jr. 2004, ARA&A, 42, 603
- Kormendy, J., & Richstone, D. 1995, ARA&A, 33, 581
- Kornei, K. A., & McCrady, N. 2009, ApJ, 697, 1180
- Kotulla, R., Fritze, U., Weilbacher, P., & Anders, P. 2009, MNRAS, 396, 462
- Koushiappas, S. M., Bullock, J. S., & Dekel, A. 2004, MNRAS, 354, 292
- Krajnović, D., Cappellari, M., de Zeeuw, P. T., & Copin, Y. 2006, MNRAS, 366, 787

-
- Kuijken, K., & Merrifield, M. R. 1995, *ApJ*, 443, L13
- Larsen, S. S., Brodie, J. P., & Hunter, D. A. 2004, *AJ*, 128, 2295
- Lauer, T. R., Faber, S. M., Ajhar, E. A., Grillmair, C. J., & Scowen, P. A. 1998, *AJ*, 116, 2263
- Lauer, T. R., Tremaine, S., Richstone, D., & Faber, S. M. 2007, *ApJ*, 670, 249
- Lindblad, B. 1925, *ApJ*, 62, 191
- Lodato, G., & Natarajan, P. 2006, *MNRAS*, 371, 1813
- Loeb, A., & Rasio, F. A. 1994, *ApJ*, 432, 52
- Lokas, E. L., & Mamon, G. A. 2001, *MNRAS*, 321, 155
- Lotz, J. M., Miller, B. W., & Ferguson, H. C. 2004, *ApJ*, 613, 262
- Lotz, J. M., Telford, R., Ferguson, H. C., Miller, B. W., Stiavelli, M., & Mack, J. 2001, *ApJ*, 552, 572
- Loveday, J., Peterson, B. A., Efstathiou, G., & Maddox, S. J. 1992, *ApJ*, 390, 338
- Lynden-Bell, D. 1978, *Phys. Scr*, 17, 185
- MacArthur, L. A., Courteau, S., & Holtzman, J. A. 2003, *ApJ*, 582, 689
- Maciejewski, W. 2004a, *MNRAS*, 354, 883
- Maciejewski, W. 2004b, *MNRAS*, 354, 892
- Maciejewski, W., Teuben, P. J., Sparke, L. S., & Stone, J. M. 2002, *MNRAS*, 329, 502
- Mackey, A. D., & Gilmore, G. F. 2003, *MNRAS*, 340, 175
- Madau, P., & Rees, M. J. 2001, *ApJ*, 551, L27

-
- Magorrian, J., et al. 1998, *AJ*, 115, 2285
- Maoz, E. 1998, *ApJ*, 494, L181
- Maraston, C. 1998, *MNRAS*, 300, 872
- Maraston, C. 2005, *MNRAS*, 362, 799
- Marconi, A., & Hunt, L. K. 2003, *ApJ*, 589, L21
- Markwardt, C. B. 2009, in *Astronomical Society of the Pacific Conference Series*, Vol. 411, *Astronomical Data Analysis Software and Systems XVIII*, ed. D. A. Bohlander, D. Durand, & P. Dowler, 251
- Mayer, L., Kazantzidis, S., Escala, A., & Callegari, S. 2010, *Nature*, 466, 1082
- McCraday, N., & Graham, J. R. 2007, *ApJ*, 663, 844
- McLaughlin, D. E., & Fall, S. M. 2008, *ApJ*, 679, 1272
- McLaughlin, D. E., King, A. R., & Nayakshin, S. 2006, *ApJ*, 650, L37
- McLaughlin, D. E., & van der Marel, R. P. 2005, *ApJS*, 161, 304
- McLeod, K. K., & Rieke, G. H. 1995, *ApJ*, 441, 96
- Merrifield, M. R., & Kuijken, K. 1999, *A&A*, 345, L47
- Merritt, D. 2009, *ApJ*, 694, 959
- Merritt, D., Ferrarese, L., & Joseph, C. L. 2001, *Science*, 293, 1116
- Merritt, D., & Hernquist, L. 1991, *ApJ*, 376, 439
- Merritt, D., & Quinlan, G. D. 1998, *ApJ*, 498, 625
- Merritt, D., & Sellwood, J. A. 1994, *ApJ*, 425, 551

-
- Merritt, D., & Wang, J. 2005, *ApJ*, 621, L101
- Miller, M. C., & Hamilton, D. P. 2002, *MNRAS*, 330, 232
- Milosavljević, M. 2004, *ApJ*, 605, L13
- Miocchi, P., Capuzzo Dolcetta, R., Di Matteo, P., & Vicari, A. 2006, *ApJ*, 644, 940
- Miralda-Escudé, J., & Kollmeier, J. A. 2005, *ApJ*, 619, 30
- Morelli, L., et al. 2004, *MNRAS*, 354, 753
- Mulchaey, J. S., & Regan, M. W. 1997, *ApJ*, 482, L135
- Murray, N., Quataert, E., & Thompson, T. A. 2005, *ApJ*, 618, 569
- Naab, T., & Burkert, A. 2003, *ApJ*, 597, 893
- Naab, T., Burkert, A., & Hernquist, L. 1999, *ApJ*, 523, L133
- Naab, T., Khochfar, S., & Burkert, A. 2006, *ApJ*, 636, L81
- Naab, T., & Ostriker, J. P. 2009, *ApJ*, 690, 1452
- Navarro, J. F., & Benz, W. 1991, *ApJ*, 380, 320
- Navarro, J. F., Frenk, C. S., & White, S. D. M. 1996, *ApJ*, 462, 563
- Navarro, J. F., & Steinmetz, M. 2000, *ApJ*, 538, 477
- Navarro, J. F., & White, S. D. M. 1994, *MNRAS*, 267, 401
- Neumayer, N., Walcher, C. J., Andersen, D., Sanchez, S. F., Boeker, T., & Rix, H.
2011, ArXiv e-prints
- Norman, C. A., Sellwood, J. A., & Hasan, H. 1996, *ApJ*, 462, 114
- Noyola, E., Gebhardt, K., & Bergmann, M. 2008, *ApJ*, 676, 1008

- Noyola, E., Gebhardt, K., Kissler-Patig, M., Lützgendorf, N., Jalali, B., de Zeeuw, P. T., & Baumgardt, H. 2010, *ApJ*, 719, L60
- Omukai, K., Schneider, R., & Haiman, Z. 2008, *ApJ*, 686, 801
- Paudel, S., Lisker, T., & Kuntschner, H. 2010, *ArXiv e-prints*
- Pelupessy, F. I., Di Matteo, T., & Ciardi, B. 2007, *ApJ*, 665, 107
- Peng, E. W., et al. 2006, *ApJ*, 639, 95
- Perlmutter, S., et al. 1999, *ApJ*, 517, 565
- Peterson, B. M., et al. 2004, *ApJ*, 613, 682
- Portegies Zwart, S. F., Baumgardt, H., Hut, P., Makino, J., & McMillan, S. L. W. 2004, *Nature*, 428, 724
- Portegies Zwart, S. F., & McMillan, S. L. W. 2002, *ApJ*, 576, 899
- Prugniel, P., & Simien, F. 1997, *A&A*, 321, 111
- Raha, N., Sellwood, J. A., James, R. A., & Kahn, F. D. 1991, *Nature*, 352, 411
- Read, J. I., Goerdt, T., Moore, B., Pontzen, A. P., Stadel, J., & Lake, G. 2006, *MNRAS*, 373, 1451
- Read, J. I., Lake, G., Agertz, O., & Debattista, V. P. 2008, *MNRAS*, 389, 1041
- Regan, J. A., & Haehnelt, M. G. 2009, *MNRAS*, 396, 343
- Richstone, D., et al. 1998, *Nature*, 395, A14
- Richstone, D. O., & Tremaine, S. 1985, *ApJ*, 296, 370
- Riess, A. G., et al. 1998, *AJ*, 116, 1009

- Robertson, B., Hernquist, L., Cox, T. J., Di Matteo, T., Hopkins, P. F., Martini, P., & Springel, V. 2006, *ApJ*, 641, 90
- Rossa, J., van der Marel, R. P., Böker, T., Gerssen, J., Ho, L. C., Rix, H.-W., Shields, J. C., & Walcher, C.-J. 2006, *AJ*, 132, 1074
- Roškar, R., Debattista, V. P., Quinn, T. R., Stinson, G. S., & Wadsley, J. 2008, *ApJ*, 684, L79
- Rubin, V. C., & Ford, W. K., Jr. 1970, *ApJ*, 159, 379
- Saha, K., Tseng, Y., & Taam, R. E. 2010, *ApJ*, 721, 1878
- Sakamoto, K., Okumura, S. K., Ishizuki, S., & Scoville, N. Z. 1999, *ApJ*, 525, 691
- Santoro, F., & Shull, J. M. 2006, *ApJ*, 643, 26
- Satoh, C. 1980, *PASJ*, 32, 41
- Sazonov, S. Y., Ostriker, J. P., Ciotti, L., & Sunyaev, R. A. 2005, *MNRAS*, 358, 168
- Schawinski, K., Treister, E., Urry, C. M., Cardamone, C. N., Simmons, B., & Yi, S. K. 2011, *ApJ*, 727, L31
- Schinnerer, E., Böker, T., & Meier, D. S. 2003, *ApJ*, 591, L115
- Schinnerer, E., Böker, T., Meier, D. S., & Calzetti, D. 2008, *ApJ*, 684, L21
- Schneider, R., Omukai, K., Inoue, A. K., & Ferrara, A. 2006, *MNRAS*, 369, 1437
- Schödel, R., Merritt, D., & Eckart, A. 2009, *A&A*, 502, 91
- Schweizer, F., & Seitzer, P. 1992, *AJ*, 104, 1039
- Scott, N., et al. 2009, *MNRAS*, 398, 1835
- Scoville, N., et al. 2007, *ApJS*, 172, 150

- Searle, L., & Zinn, R. 1978, *ApJ*, 225, 357
- Sellwood, J. A. 2003, *ApJ*, 587, 638
- Sellwood, J. A. 2008, *ApJ*, 679, 379
- Sellwood, J. A., & Binney, J. J. 2002, *MNRAS*, 336, 785
- Sellwood, J. A., & Debattista, V. P. 2009, *MNRAS*, 398, 1279
- 1968, *Atlas de galaxias australes*, ed. Sersic, J. L.
- Seth, A., Agüeros, M., Lee, D., & Basu-Zych, A. 2008a, *ApJ*, 678, 116
- Seth, A. C., Blum, R. D., Bastian, N., Caldwell, N., & Debattista, V. P. 2008b, *ApJ*, 687, 997
- Seth, A. C., et al. 2010, *ApJ*, 714, 713
- Seth, A. C., Dalcanton, J. J., & de Jong, R. S. 2005, *AJ*, 129, 1331
- Seth, A. C., Dalcanton, J. J., Hodge, P. W., & Debattista, V. P. 2006, *AJ*, 132, 2539
- Shapiro, S. L. 2005, *ApJ*, 620, 59
- Shen, J., Vanden Berk, D. E., Schneider, D. P., & Hall, P. B. 2008, *AJ*, 135, 928
- Shlosman, I., & Begelman, M. C. 1989, *ApJ*, 341, 685
- Shlosman, I., Frank, J., & Begelman, M. C. 1989, *Nature*, 338, 45
- Sikkema, G., Carter, D., Peletier, R. F., Balcells, M., Del Burgo, C., & Valentijn, E. A. 2007, *A&A*, 467, 1011
- Silk, J., & Rees, M. J. 1998, *A&A*, 331, L1
- 1987, *Dynamical evolution of globular clusters*, ed. Spitzer, L.

-
- Stadel, J. G. 2001, Ph.D. thesis, AA(UNIVERSITY OF WASHINGTON)
- Steinmetz, M., & Navarro, J. F. 1999, *ApJ*, 513, 555
- Steinmetz, M., & Navarro, J. F. 2002, *New Astronomy*, 7, 155
- Tanaka, T., & Haiman, Z. 2009, *ApJ*, 696, 1798
- Tegmark, M., Silk, J., Rees, M. J., Blanchard, A., Abel, T., & Palla, F. 1997, *ApJ*, 474, 1
- Terzić, B., & Graham, A. W. 2005, *MNRAS*, 362, 197
- Thomas, J., et al. 2009, *MNRAS*, 393, 641
- Toomre, A. 1964, *ApJ*, 139, 1217
- Tremaine, S., et al. 2002, *ApJ*, 574, 740
- Tremaine, S. D., Ostriker, J. P., & Spitzer, L., Jr. 1975, *ApJ*, 196, 407
- van den Bosch, F. C. 1998, *ApJ*, 507, 601
- van der Marel, R. P. 1991, *MNRAS*, 253, 710
- van der Marel, R. P., & Anderson, J. 2010, *ApJ*, 710, 1063
- van der Marel, R. P., Cretton, N., de Zeeuw, P. T., & Rix, H.-W. 1998, *ApJ*, 493, 613
- van der Marel, R. P., & Franx, M. 1993, *ApJ*, 407, 525
- van der Marel, R. P., Rossa, J., Walcher, C. J., Boeker, T., Ho, L. C., Rix, H.-W., & Shields, J. C. 2007, in *IAU Symposium*, Vol. 241, *IAU Symposium*, ed. A. Vazdekis & R. F. Peletier, 475
- van der Marel, R. P., & van Dokkum, P. G. 2007, *ApJ*, 668, 738

- van der Wel, A., & van der Marel, R. P. 2008, *ApJ*, 684, 260
- Volonteri, M., & Natarajan, P. 2009, *MNRAS*, 400, 1911
- Volonteri, M., & Rees, M. J. 2006, *ApJ*, 650, 669
- Wagner, S. J., Bender, R., & Moellenhoff, C. 1988, *A&A*, 195, L5
- Walcher, C. J., Böker, T., Charlot, S., Ho, L. C., Rix, H.-W., Rossa, J., Shields, J. C., & van der Marel, R. P. 2006, *ApJ*, 649, 692
- Walcher, C. J., et al. 2005, *ApJ*, 618, 237
- Wehner, E. H., & Harris, W. E. 2006, *ApJ*, 644, L17
- White, S. D. M., & Rees, M. J. 1978, *MNRAS*, 183, 341
- Whitmore, B. C., & Schweizer, F. 1995, *AJ*, 109, 960
- Widrow, L. M. 2000, *ApJS*, 131, 39
- Widrow, L. M., & Dubinski, J. 2005, *ApJ*, 631, 838
- Widrow, L. M., Pym, B., & Dubinski, J. 2008, *ApJ*, 679, 1239
- Wilczynski, E. J. 1896, *ApJ*, 4, 97
- Willott, C. J., et al. 2007, *AJ*, 134, 2435
- Wise, J. H., Turk, M. J., & Abel, T. 2008, *ApJ*, 682, 745
- Wosley, S. E., & Weaver, T. A. 1986, *ARA&A*, 24, 205
- Wyithe, J. S. B., & Loeb, A. 2003, *ApJ*, 595, 614
- Wyse, R. F. G., Gilmore, G., & Franx, M. 1997, *ARA&A*, 35, 637

Xiao, T., Barth, A. J., Greene, J. E., Ho, L. C., Bentz, M. C., Ludwig, R. R., & Jiang, Y. 2011, ArXiv e-prints

Yoshida, N., Omukai, K., Hernquist, L., & Abel, T. 2006, ApJ, 652, 6

Younger, J. D., Hopkins, P. F., Cox, T. J., & Hernquist, L. 2008, ApJ, 686, 815

Zaritsky, D., Elston, R., & Hill, J. M. 1989, AJ, 97, 97

Zhao, H. 1997, MNRAS, 287, 525

Zheng, X. Z., et al. 2009, ApJ, 707, 1566